ABSTRACT

Unimolecular Decomposition Kinetics at Resolved Internal Energies

Adam Mansell, Ph.D.

Mentor: Darrin J. Bellert, Ph.D.

The kinetic behavior of microcanonical unimolecular decomposition reactions involving clusters formed by the electrostatic interaction between transition metal cations and simple organic molecules has been measured at multiple internal energies. The presence of the metal lowers the energy necessary for the reactions to take place. Thus, these reactions serve as a useful model for catalysis.

These measurements were made in a custom built molecular beam apparatus, in which the experimental environment is free of the many complicating effects which are inherent to condensed phase measurements. The reacting clusters are formed in a supersonic expansion and bound by the charge-dipole interaction between the organic and the transition metal cation. Rearrangement reactions are initiated by absorption of a visible photon from a dye laser.

The most widely used formalism for unimolecular kinetic calculations is Rice-Ramsperger-Kassel-Marcus (RRKM) theory, which states that the rate constant for a unimolecular reaction is dependent on the way in which the internal energy is distributed to the various modes of motion of the molecule. The rate constant is then proportional to

the ratio of the sum of states of the transition state to the density of states of the reactant. This theory is utilized by our group to determine the reaction activation energies.

This dissertation will focus on the unimolecular decomposition of Ni^+propanal and Ni^+acetic acid. The two reactions involve competition between C-C bond activation and either C-H or C-O bond activation.

Unimolecular Decomposition Kinetics at Resolved Internal Energies

by

Adam Mansell, B.A.

A Dissertation

Approved by the Department of Chemistry and Biochemistry

_____

Patrick J. Farmer, Ph.D., Chairperson

Submitted to the Graduate Faculty of
Baylor University in Partial Fulfillment of the
Requirements for the Degree
of

Doctor of Philosophy

Approved by the Dissertation Committee

_____

Darrin J. Bellert, Ph.D., Chairperson

_____

Carlos E. Manzanares, Ph.D.

_____

Kevin L. Shuford, Ph.D.

_____

Kevin K. Klausmeyer, Ph.D.

_____

Zhenrong Zhang, Ph.D.

Accepted by the Graduate School

December 2016

_____

J. Larry Lyon, Ph.D., Dean

Page bearing signatures is kept on file in the Graduate School.

TABLE OF CONTENTS

LIST OF FIGURES

LIST OF TABLES

ACKNOWLEDGMENTS

Above all others, I must first thank God who has provided me with the resources to accomplish this task, and surrounded me with the people and support that made the journey not just possible, but enjoyable.

Next, I want to express my sincere appreciation and admiration for Dr. Darrin J. Bellert. Dr. Bellert has been the epitome of an excellent advisor throughout my time at Baylor. Always patient with me and willing to guide me on my journey, Dr. Bellert deftly and gracefully walks the fine line between friendly and professional; family man and professor; friend and boss. Unwavering in his convictions and confident in his strengths while humbly acknowledging his shortcomings, Dr. Bellert is the kind of professor I hope to be someday.

I would also like to thank Dr. John W. Kenney III. Dr. Kenney mentored me as an undergraduate, and helped me begin my journey in chemical research. Dr. Kenney showed me that high level research can be done even when under equipped or underfunded, as long as the researchers are patient, determined and resourceful.

I would also like to thank my committee members, Dr. Kevin Shuford, Dr. Carlos Manzanares, Dr. Kevin Klausmeyer, and Dr. Zhenrong Zhang, for their incredible patience with me throughout this process, their willingness to read the many versions of this document, and their many helpful insights.

Further, I would like to thank those individuals who have passed through this group before me, paving the way and making my success possible. Specifically, I would

like to thank Dr. Vanessa Castleberry, Dr. Otsmar Villarroel and Dr. Ivanna Laboren who all provided assistance whenever I asked for it, and were invaluable resources in learning how to use the instrument which they helped build. Similarly, I would like to thank Zachry Theis and Michael Gutierrez for working with me on the studies presented in this document.

The Baylor faculty and staff have been incredibly supportive throughout my time here, and through all my interactions with individuals associated with the University, I have felt that they were genuinely hoping for my success. Of particular note, I would like to thank Nancy Kallus, Virginia Hynek, Barbara Rauls and Adonna Cook who all patiently helped me with the ins and outs of being a student and helped keep our lab, and the building, running smoothly. Also, I would like to thank Dr. Patrick Farmer who showed a genuine interest in my development as a scientist, investing time and resources in me, even when I wasn't his student, and Dr. Charles Garner whose door was always open. Dr. Garner was my first impression of Baylor and it was his passion for research that initially led to me choosing Baylor for my graduate studies.

Penultimately, I would like to thank my friends and family who have helped and encouraged me throughout my life, providing emotional, spiritual and physical support whenever I needed it.

Finally, I would like to thank my wife, Karin Mansell. Karin, there is not enough room here to adequately discuss just how grateful I am or the many reasons why. Just know that were it not for you, I would have burned out long ago.

SDG

CHAPTER ONE

Introduction

It would be difficult to overstate the importance of transition metal catalysts to modern society. Indeed, it was the discovery that an iron compound could catalyze a reaction between N_2 and H_2 to form ammonia that prevented a catastrophic collapse into a Malthusian trap at the beginning of the twentieth century.[1] As of 2012, approximately 90% of all chemical processes involve transition metals as a catalyst in at least one of their steps.[2] Transition metal catalysts promise to be the solution to a number of problems facing modern society (energy capture and storage; CO_2 sequestration; water splitting/ sanitation; drug discovery, synthesis and delivery etc.). Given their importance and potential, it is not surprising that a great deal of research has been focused on, and importance placed on the elucidation of how they work and discovery of new catalysts. Indeed, approximately 1/5 of all Nobel laureates in chemistry were awarded the prize because of work on catalysis.[3] However, there does not yet exist a means by which the optimal combination of metals and metal oxides to catalyze a given reaction can be predicted with certainty. Advances in computational chemistry methods over the past few decades have made it possible to calculate the potential energy surface (PES) and structural information for relatively simple reactions, providing insights to the process but the computationally demanding nature of transition metal chemistry means the calculations must be chosen carefully; a decision which must be guided by experimental results. In addition, the newness of the territory and the unknown ramifications of the

approximations used means the results of the computation must be checked against the results of carefully carried out experiments.

Molecular ion beam techniques provide a unique arena in which to study fundamental aspects of reactions involving transition metal ions, as they are free from many of the complicating factors inherent to the condensed phase which make it difficult to decipher the exact features of a reaction center or reaction intermediate. For example, Brauman and Blair were able to show that the order of acidity of simple alcohols in the gas phase is the opposite of that in aqueous solution.[4] However, while there are situations where direct comparisons can be made between experiment and 'real world' scenarios (atmospheric chemistry and interstellar chemistry), the same factors which make molecular ion beam experiments ideal for studying the fundamental aspects of reactions also make it difficult to predict exactly how the quantities measured will manifest in the condensed phase reaction. The gap is being bridged by experiments that determine the solvation spheres of ions by various solvent molecules[5] and the binding nature of ligands to a fully coordinated center.[6]

Metal mediated transfer reactions are some of the most widely studied groups of reactions by ion beam techniques.[5-13] There are thermodynamic limits to which metals can practically act as catalysts in atomic and functional group transfer reactions, which these techniques are uniquely qualified to determine. Specifically, the binding affinity of the metal to the moiety being transferred must be greater than that between the donor and the moiety being transferred, but less than that between the acceptor and the moiety. This creates a "thermodynamic window of opportunity" which dictates which ions will function as catalysts. There are a number of mass spec techniques capable of measuring

atomic binding affinity (some of which will be discussed briefly in the following paragraphs), which operate by detection of dissociation fragmentation as a function of energy. The form of this initiation energy is the key differentiating characteristic between techniques. Photo induced dissociation experiments use photons to initiate the dissociation, which has the advantage of providing a well-defined amount of energy to the system, but suffers from the requirement that the ion must have a high Frank-Condon overlap near the dissociation threshold (a requirement that favors large molecules) and the dissociation must occur quickly (a requirement that favors small molecules).[7] Threshold Collision Induced Dissociation (TCID)[8] provides the necessary energy through collisions with an inert gas, usually xenon because of its large mass and polarizability, which encourages efficient energy transfer. By taking the thermal distribution of the precursor and the energy distribution of the collisions into account, extrapolation can be made to determine the 0 K bond dissociation energy.[8] Kinetic Energy Release Distribution (KERD)[9] experiments measure how the energy is partitioned to the various fragments after dissociation occurs, providing insight into the way the energy is partitioned during the reaction.[9] Knowledge of threshold energies allows for the determination of how well a calculated Potential Energy Surface (PES) reflects reality. Calculated PES's can be used to predict kinetics which can be measured or extrapolated with various techniques (Flowing Afterglow, Selected-Ion Flow-Tube, Inductively-Coupled Plasma/Selected Ion Flow Tube, Kinetic Energy Release Distribution, Collision Induced Dissociation, Ion Cyclotron Resonance, Fourier Transform Ion Cyclotron Resonance and Single Photon Induced Dissociation Rearrangement Reactions)[10]. For most of these techniques there is a thermal distribution of the precursor, and in

experiments where the activation energy is provided through collisions, there is also an energy distribution associated with the collision probability which must be accounted for.

The metal cation mediated oxygen transfer from nitrogen oxides to various compounds is one of the most thoroughly studied group of reactions studied by gas phase ion techniques and among some of the most important reactions due to the detrimental environmental effects of N_2O, NO and NO_2.[11] These reactions are often very exothermic, but do not proceed at room temperature due to a large activation barrier. It has been shown that metal cations can provide alternate pathways with lower activation barriers, allowing for the reduction of nitrogen oxides at easily accessible temperatures. Out of 59 atomic cations, 26 have been found to have oxygen affinities inside the thermodynamic 'window of opportunity' for the transfer of atomic oxygen from N_2O to CO.[11] Using an Inductively-Coupled Plasma/ Selected-Ion Flow Tube (ICP/ SIFT) tandem mass spectrometer, Blagojevic and coworkers[11] were able to show that 10 of these demonstrated catalytic activity (Ca^+, Fe^+, Ge^+, Sr^+, Ba^+, Os^+, Ir^+, Pt^+, Eu^+ and Yb^+). The 16 that did not (Cr^+, Mn^+, Co^+, Ni^+, Cu^+, Se^+, Mo^+, Ru^+, Rh^+, Sn^+, Te^+, Re^+, Pb^+, Bi^+, Tm^+ and Lu^+) reacted too slowly with either N_2O or CO.[11] The same research group has also explored the catalytic activity of metal cations in the reduction of NO and NO_2, and demonstrated that Fe^+, Os^+ and Ir^+ are able to catalyze the entire cycle.

The metal cation catalyzed oxidation of H_2 by N_2O has also been explored, especially with Fe^+ as the catalyst.[12] This system has a number of remarkable features, the most interesting of which is that the cross-section (which is intimately related to the rate constant) decreases with increasing energy at energies just above threshold.[13] This has been attributed to spin surface crossing (SSC), a phenomenon in which the sextet surface

begins lower in energy than the quartet surface, but is relatively higher for the insertion intermediate (H-FeO^+-H) and the transition states to either side. This situation leads to a decrease in the overall production rate of water from the $FeO^+ + H_2$ collision, due to increasing probability of the reaction proceeding along the higher energy surface. These $FeO^+ + H_2$ studies have shown the importance of being able to provide experimental benchmarks for computational studies. Our research group adds to this body of knowledge by monitoring the microcanonical ensemble dissociation of metal cation containing complexes as a function of time, and observing the change in dissociation characteristics as a function of energy. Specifically, this dissertation focuses on the nickel cation mediated decomposition of propionaldehyde and acetic acid. In the decomposition of Ni^+Propionaldehyde, the kinetic data was gathered primarily by myself, Zachry Theis and Michael Gutierrez; the interpretation of the results and the modeling of the reaction mechanism was done by myself and Dr. Darrin Bellert; and the PES and vibrational frequency calculations were conducted by Dr. O. Nieto Faza and Dr. Carlos Silva Lopez.

CHAPTER TWO

Experimental Apparatus and Technique

Introduction

Kinetic measurements on the decomposition of small clusters are made using a custom built instrument (Figure 2.1), described in this chapter. In general, the reactant clusters are generated in a large 120 L vacuum ($2x10^{-7}$ Torr) chamber via collisions within a supersonic expansion, which lowers the internal energy of the cluster significantly. The ions absorb a photon which provides the energy necessary to overcome any reaction barriers along the reaction pathway. The molecular beam passes through two skimmers before entering a Wiley Mclaren[14] type orthogonal accelerator which sends the cations into a ~two meter field free time-of-flight (TOF), where the ions are separated by mass. At the detection end of the TOF, the ions pass through a kinetic energy filter (sector) which can be set to transmit ions with a specific kinetic energy. If the sector is set to transmit cations with the same kinetic energy imparted by the orthogonal accelerator, then a mass spectrum of the ions formed in the source is generated. If any of these 'parent' ions decay inside the time of flight, the mass of the cation will change, while the velocity of the daughter fragments remain constant, and the sector can be tuned to selectively transmit daughters of specific mass.

The energy needed to form decomposition products is provided by a photon from a tunable dye laser. By systematically changing the timing of the laser pulse relative to the orthogonal accelerator, we are able to change the amount of time the complex has to

decay prior to entering the time of flight, which determines the intensity of the detected daughter fragment. By plotting fragment intensity as a function of laser timing relative to orthogonal accelerator timing, we can monitor the dependence of the decomposition process. As we change the wavelength of the photon, we can determine the decomposition behavior as a function of cluster internal energy.

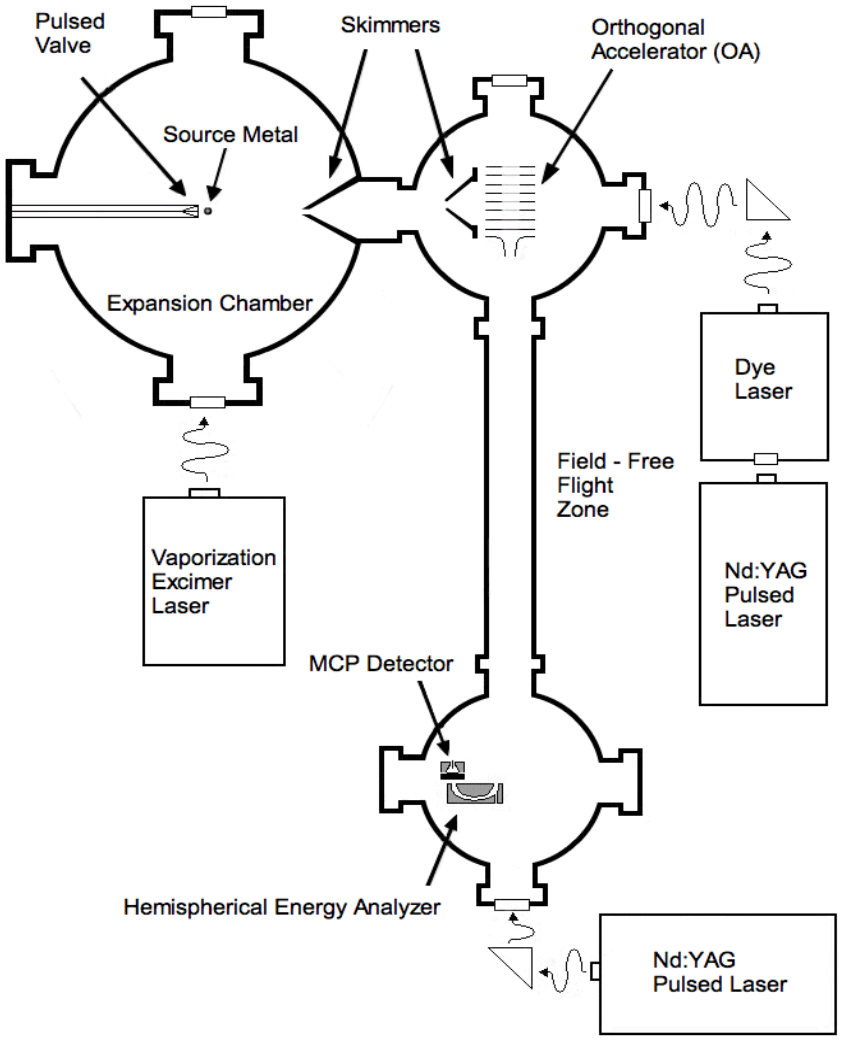

Figure 2.1 Diagram of the custom apparatus described in this chapter

Complex Formation and Detection

A line pressurized to 100 p.s.i. with helium and slightly doped with the organic of interest is coupled into a 120L vacuum chamber (base pressure ~$2x10^{-7}$Torr). Briefly opening a Parker series 9 pulsed valve allows the gas mixture to escape into the vacuum chamber. As the gas expands over a rotating metal rod, the rod is ablated with focused 248nm light from an excimer laser. The ablated metal atoms are entrained in the expanding gas where collisions form complexes which are cooled by further collisions with the carrier gas in the adiabatic expansion. The expanding gas is skimmed twice, allowing only the center of the molecular beam to reach the time of flight (TOF) portion of the instrument. When the densest portion of the cluster packet is between the parallel capacitor plates, the orthogonal accelerator (OA) is pulsed from ground potential to 1.75 kV, sending cations into the field free TOF with a common kinetic energy, where they are separated by mass.

Internal Energy Minimization

Energy resolution is a hallmark of this experiment, and in order to extract anything meaningful about the internal energy after photon absorption, the internal energy prior to photon absorption must be well defined. This is accomplished by lowering the internal energy of the complex prior to initiating the reaction to such an extent that the photon energy is essentially the energy of the complex. This is done through adiabatic expansion, which has been the standard for creating cold ion complexes in molecular beams for decades,[2] and as such, a number of tools have been developed which allow us to ensure that the energy in each mode of motion has been sufficiently reduced.

In our apparatus, in order to determine the translational energy distribution of the species of interest, we systematically change the time at which the beam is created relative to when the orthogonal accelerator pulses on, and monitor how the intensity changes (Figure 2.1). The probability, P, of a particle having a given translational energy, v, is given by

$$P(v) = Nv^3 e^{-\frac{m(v-\bar{u})^2}{2kT}} \qquad \text{Equation 2.1}$$

Where N is a normalization factor, m is the weighted mass of the doped helium gas, T is the local temperature and ū is the average velocity in the beam. By changing the timing values of the ablation laser relative to the opening of the pulsed valve, we can optimize the beam profile to minimize the translational distribution of the ions. The average temperature calculated from the data in Figure 2.1 is approximately one kelvin. This value is typical of the type of beam routinely generated for our experiments.

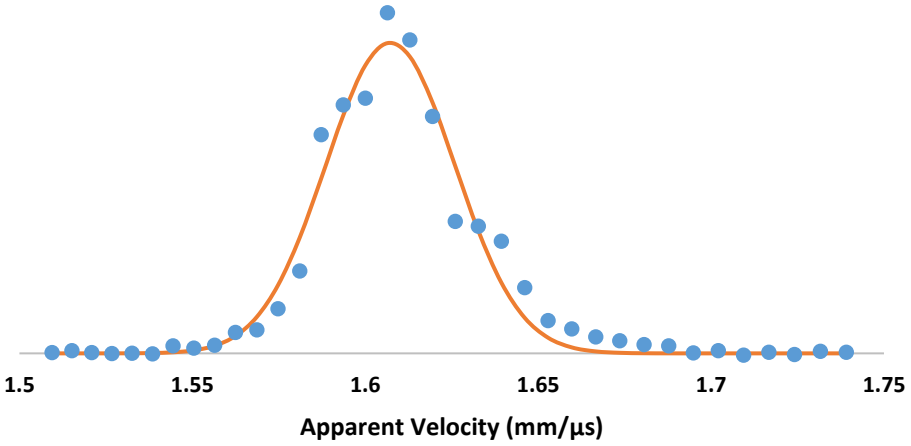

Figure 2.2 The velocity distribution of the precursor clusters for the Ni^+Propionaldehyde complex

In order to provide further evidence of the effectiveness of our cooling method, we have conducted experiments using a mixture of helium and hydrogen as the carrier gas, as opposed to neat helium. The mixture is more effective at cooling because of the vibrational mode in the diatomic molecule. Because the measured rate constants are the same within error, we conclude that it is appropriate to assume that the energy of the activated complex is the same as the energy of the incident photon.

The final validation that the internal energy of the constituents of the molecular beam has been sufficiently cooled, comes from mass spectra, which show that the source is able to generate large clusters with small binding energies. Figure 2.2 is a mass spectrum of the ion complexes generated with Ni^+ and propionaldehyde, showing peaks for Ni^+, Ni^+CO, $Ni^+propionaldehyde_n$ where n is 1-5, at mass 58, 86, 116, 174, 232, 290 and 348 amu respectively. Table 2.1 shows bond energies for Ni^+ bound to various ligands. As the number of ligands increases, the bond energy for each successive ligand drops significantly. Therefore, we conclude that the internal energy of the constituents of the beam which contains these large clusters can be reasonably approximated as the energy of the photon which activates the reaction.

Initiating the Reaction

The energy for the reaction is provided by a photon from a Nd:YAG (Spectra Physics, Quanta Ray) pumped dye laser (Sirah). The Nd:YAG generates approximately 1000 mJ/pulse of 1064 nm light, which is either frequency doubled (532 nm) or tripled (355 nm) depending on the absorption characteristics of the dye being used. The molecular beam intersects the visible photon before the orthogonal accelerator is pulsed on. The photon promotes a low lying forbidden transition in the metal cation which is

made slightly more allowed by the electrostatic interactions with the organic. The energy is then distributed through intersystem crossing to the various modes of motion of the complex on the ground state potential energy surface. If the internal energy of the system is sufficient to overcome all energy barriers along the reaction coordinate, then the reaction will proceed to products.

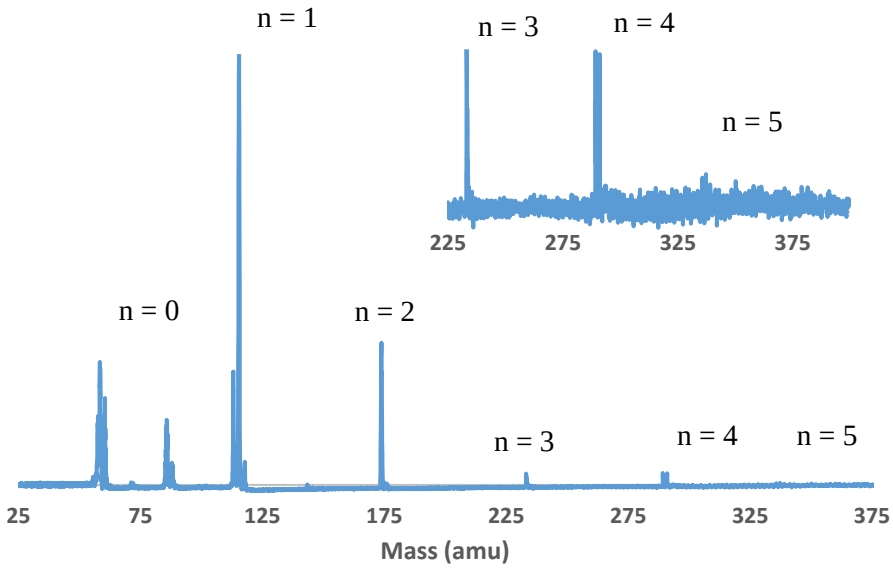

Figure 2.3 Mass spectrum showing Ni^+, Ni^+CO and $Ni^+(propionaldehyde)_n$ where n is 0-5

Product Formation and Detection

The ions pass through a hemispherical sector (Figure 2.4) which separates ions by kinetic energy prior to reaching the detector. The sector is made from two polished stainless steel blocks. Both blocks are electrically isolated. The inner block is negatively charged while the outer block is positively charged. Ions with the appropriate kinetic energy follow a stable trajectory through the sector while ions with different kinetic energies collide with the walls of the sector. The ions which pass through the sector strike a chevron dual microchannel plate detector (Burle Industries).

Table 2.1 Bond dissociation energies between Ni^+ and various ligands[6]

System	BDE (cm^{-1})	±
Ni^+-H_2	6020	100
Ni^+H_2-H_2	6300	10
$Ni^+(H_2)_2$-H_2	3900	10
$Ni^+(H_2)_3$-H_2	2500	10
$Ni^+(H_2)_4$-H_2	1500	67
$Ni^+(H_2)_5$-H_2	300	70
Ni^+-CH_4	8710	
Ni^+CH_4-CH_4	9270	
$Ni^+(CH_4)_2$-CH_4	2400	
$Ni^+(CH_4)_3$-CH_4	1900	
$Ni^+(CH_4)_4$-CH_4	700	
Ni^+-CO	14600	920
Ni^+CO-CO	14000	920
$Ni^+(CO)_2$-CO	7900	500
$Ni^+(CO)_3$-CO	6000	300

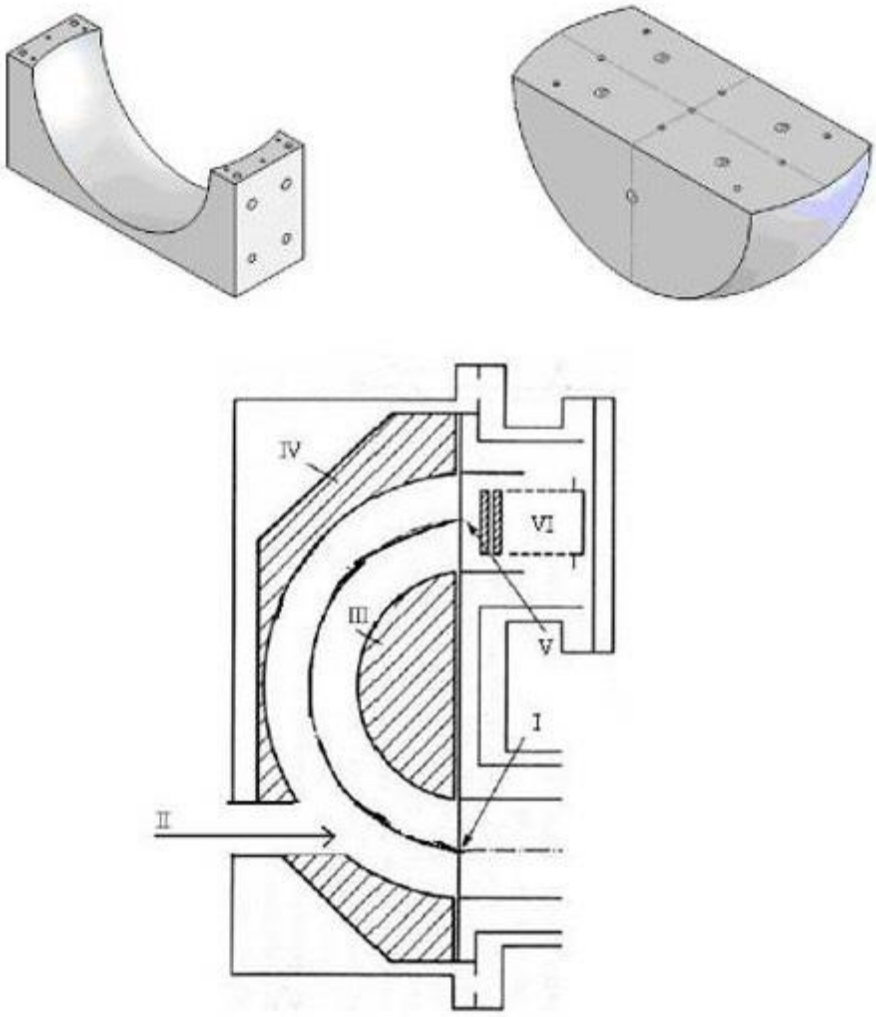

Figure 2.4 Diagram of the Hemispherical sector used for secondary mass separation. The sector is made from two stainless steel blocks which are held together by a separate stainless steel plate. The two blocks are electrically isolated and charged such that an ion of a chosen mass has a stable trajectory to the detector.
I-Ion Beam Entrance
II-Photon Entrance for photo-dissociation studies
III-Negatively Charged portion of the sector
IV-Positively Charged portion of the sector
V-Ion Beam Exit
VI-Micro-Channel plate detector

If the sector is set to transmit ions with the same kinetic energy as that imparted by the acceleration grid, the result is a mass spectrum of the ions formed in the source which reached the acceleration grid intact and did not decay in the TOF. Any dissociation products formed inside the TOF will have the same velocity as the parent

complex but a smaller mass, and therefore a smaller kinetic energy. The charge on each half of the sector can be set to allow the cationic products to reach the detector.

If the reaction follows a simple unimolecular decay process, and proceeds from reactants (A) to products (P) via a single non-reversible step with rate constant k_1, (reaction 2.1)

$$A \xrightarrow{k_1} P \qquad \text{Reaction 2.1}$$

The rate equations for A and P are

$$\frac{dA}{dt} = -k_1 A(t) \qquad (2.2)$$

$$\frac{dP}{dt} = k_1 A(t) \qquad (2.3)$$

The solutions to these rate equations govern the time dependence of the product formation and precursor decomposition.

$$A(t) = A_0 e^{-k_1 t} \qquad (2.4)$$

$$P(t) = A_0 - A_0 e^{-k_1 t} \qquad (2.5)$$

The intensity of the observed peak is determined by the amount of product formed in the TOF, which is equal to the total amount formed, P(t+L), (where L is the amount of time the ion spends in the TOF, which is dependent on the size of parent complex and is usually about 40 microseconds) minus the amount formed prior to orthogonal acceleration, P(t).

$$P(t + L) - P(t) \qquad (2.6)$$

By initiating the reaction at earlier and earlier times, the time spent prior to orthogonal acceleration increases, which decreases the number of daughter ions which

strike the detector. This allows us to extract the time dependent intensity of the daughter fragment production (Figures 2.4 and 2.5). This time dependence is in turn, dependent on the internal energy of the system. The experiment can be used to determine the energy dependence of the overall rate of the reaction by changing the photon wavelength.

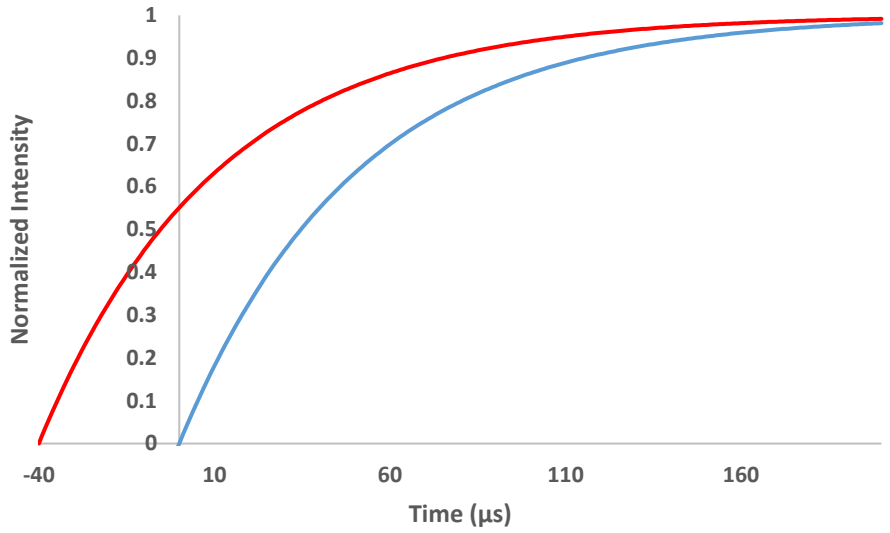

Figure 2.5 Time dependence of the product in the hypothetical $A \xrightarrow{k_1} P$ reaction, with $k_1 = 2 \times 10^{-8}$ s^{-1}. The blue curve models the amount of product formed prior to the molecular beam entering the TOF. The red curve models the total amount formed as a function of time.

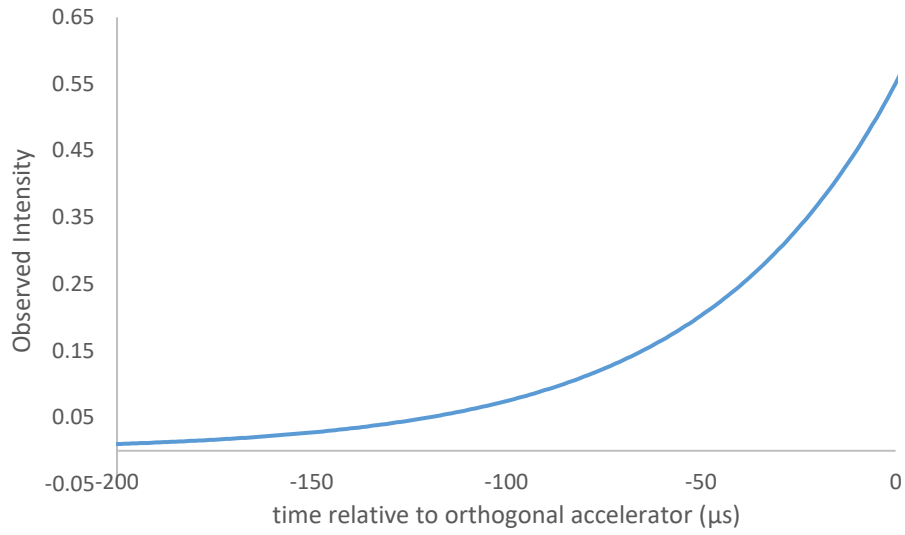

Figure 2.6 Simulation of how this experimental setup would detect the hypothetical $A \overset{k_1}{\rightarrow} P$ reaction. We choose to use negative values for the x-axis because we depict the measured intensity as a function of when the reaction is initiated relative to when the orthogonal accelerator is pulsed on. Thus, the highest intensity occurs when the entire reaction takes place inside the TOF, which occurs when the reaction is initiated simultaneously with the complexes entering the TOF.

CHAPTER THREE

Calculating RRKM Rate Constants from Vibrational Frequencies and their Dynamic Interpretation

Introduction

The essential framework for our understanding of unimolecular reaction rates was developed largely in the first half of the twentieth century.[15] The *Lindemann-Hinshelwood mechanism*, proposed in the 1922 by Lindemann and later expanded upon by Hinshelwood[16], posited that the gas phase unimolecular reactions was initiated by bimolecular collisions, which occurred at a rate independent of the reaction which followed and effectively separated the method of activation from the actual reaction. Later that decade, Rice and Ramsperger and, independently, Kassel developed an improvement on the model known as the *Rice-Ramsperger-Kassel (RRK)* model.[17, 18] The RRK model viewed the molecule as a system of identical harmonic oscillators and introduced the idea of activation energy, that sufficient energy must be deposited into specific modes of motion in order for the reaction to occur. In 1952, Rice and Marcus extended this into what is now known as *Rice-Rampsberger-Kassel-Marcus* theory *(RRKM)*, which incorporates a more complete quantum mechanical description of the molecule and utilized the concept of the transition state, a specific conformation which the molecule must adopt in order for the reaction to proceed.[19] The RRKM model remains the prevailing scientific description of unimolecular chemical kinetics to this day.

Chemical transformations require bonds to break in the reactants and new bonds to form as products are generated. The potential energy associated with these transformations defines an *n*-dimensional *potential energy surface (PES)*, where *n* is the number of atoms.[20] The *reaction pathway* is a one dimensional cross section of the PES composed of the precursor, intermediates, transition states and products of a particular reaction.[20] Reactants and intermediates of a reaction correspond to minima whereas transition states are located at maxima along the reaction pathway.

The rate of the reaction is dependent on the probability of the molecule adopting the conformations along the reaction pathway which, in turn, stems from the probability that a sufficient amount of energy is partitioned into the necessary modes of motion. The RRKM formalism assumes that (1) once the molecule adopts the transition state orientation the reaction proceeds to products and (2) the *internal vibrational energy redistribution (IVR)* is fast with respect to the timescale of the reaction. Under these constraints, the RRKM microcanonical rate constant, k(E) is given by

$$k(E) = \frac{\sigma N^{\ddagger}(E - E_0)}{\rho(E)} \tag{3.1}$$

where E is the internal energy of the system, E_0 is the activation energy for the reaction, $N^{\ddagger}(E\text{-}E_0)$ is the sum of states of the transition state from E_0 to E, ρ(E) is the density of states of the precursor at energy E, h is Planck's constant and σ is the degeneracy of the reaction pathway.[17-19] A state is defined as any unique vibrational configuration that determines the internal energy of the molecule. The sum of states, N(E), is the total number of states within a specific energy range.[20] The density of states is the number of states per energy level. Equivalently, the density of states is the derivative of the sum of states with respect to energy.[20] The density is expressed in units of inverse energy (E^{-1})

while the sum of states is a dimensionless quantity. Thus, the microcanonical rate constant of equation 3.1 has units s^{-1}.

There are 3n-6 vibrational frequencies for non-linear polyatomic molecules, and 3n-7 vibrational frequencies for the corresponding transition state. It is the values of these frequencies, which typically range from 50 – 3500 cm^{-1}, that dictate how the internal energy is distributed in the molecule. The calculation for the sum and density of states is dependent on these frequencies, which can be measured or looked up in standard data tables. However for transition states, these values must be estimated or, more likely, calculated using theoretical packages.

This chapter discusses the use of RRKM to calculate the time dependent behavior of the species involved in a decomposition reaction, using vinyl cyanide as an example. This chapter is divided into the following sections: In Section 2, the sum and density of states for vinyl cyanide ($C_3 H_3N$) are determined through a direct count method analogous to that developed by Beyer and Swinehart.[21] In Section 3, the method is extended to anharmonic oscillators using the Stein-Rabinovitch algorithm.[22] In Section 4, the RRKM microcanonical rate constants are calculated for the unimolecular dissociation of vinyl cyanide and are used to predict various dynamic properties of the chemical reaction.

Direct Count for Harmonic Oscillators – The Beyer-Swinehart Algorithm

Beyer and Swinehart (*BS*)[21] developed a surprisingly simple yet computationally intensive direct count method to calculate the sum and density of states at defined energies of an harmonic oscillator.[21] The advantage of conducting such calculations in *Mathematica* is that the user can leverage high-quality numerical ODE solvers and

interactive graphical features to visualize dynamic properties of the chemical reaction. This is demonstrated in Section 4, where the temporal development of nine different species is plotted and automatically updated as the user sets the internal energy of the system with a slider. All of this can be done in real time after some pre-computations that are exact with *Mathematica*.

There are a number of equivalent ways to implement the BS direct count of states. To ease the exposition, we first illustrate the task with a Do loop. The sum and density of states are determined by the vibrational frequencies of the species of interest, which we define in the list vList. In more complex situations such as biomolecules or reactions at very high energies, to lessen the computational burden it may be necessary to divide the value of the total energy into larger packets and modify the vibrational frequencies to be multiples of the new packet size.[22] In this case, the packet size is 1 $cm^{-1}$and the vibrational frequencies for vinyl cyanide are taken from reference 23, which is a paper by Homayoon et. al.:

```
ChemicalData["VinylCyanide","MoleculePlot"]
```

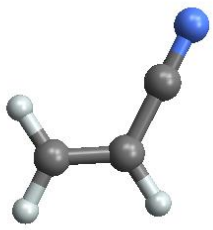

Figure 3.1 Vinyl cyanide

```
vList={235, 344, 570, 696, 872, 980, 1005, 1118, 1331, 1467, 1689, 2322, 3173,
    3214, 3271};
nFreqs=Length[vList];
```

The final result for the sum or density of states is a list with *energy*+1 elements. For the sum of states, this list is initialized with all values set to 1. The sum of states can then be calculated using a nested (or doubly-indexed) Do loop:

```
energy=100000;
sumOfStates=Table[1,energy+1];
Do[
    Do[
        sumOfStates[[w+1]]+=sumOfStates[[w+1-νList[[j]]]],
        {w,νList[[j]],energy}],
    {j,nFreqs}];
```

Because the density of states is the derivative of the sum of states, the density of states can also be determined from the sum of states table by setting the ith element of the density of states to the difference between the i^{th} and $(i-1)^{th}$ elements of the sum of states table. Alternatively and equivalently, this can be done to the initial sum of states table to derive the initial density of states table, which is list with *energy*+1 elements with the initial element set to 1 and all other elements set to 0. This can be conveniently done with PadRight.

```
densityOfStates=PadRight[{1},energy+1];
Do[
  Do[
   densityOfStates[[w+1]]+=densityOfStates[[w+1-νList[[j]]]],
   {w,νList[[j]],energy}],
  {j,nFreqs}];
```

A visual comparison of the sum and density of states, calculated for vinyl cyanide ($C_3 H_3N$), shows the behavior of the two quantities over the 0 – 100000 cm^{-1} energy range. As the general trend of the graphic is clear, we subsample the lists of values to avoid plotting millions of points needlessly increasing file size.

```
takeEvery[nth_]:=Function[list,Part[list,Range[1,Length[list],nth]]]
Show[
  ListLogPlot[takeEvery[1000]@Transpose[{Range[0, energy],
      sumOfStates}],PlotStyle -> Red],
  ListLogPlot[takeEvery[1000]@Transpose[{Range[0, energy],
      densityOfStates}]], Frame->True, FrameLabel->{"Energy (cm^-1)","Sum of
      States (unitless)\n and Density of States (/cm^-1)"}]
```

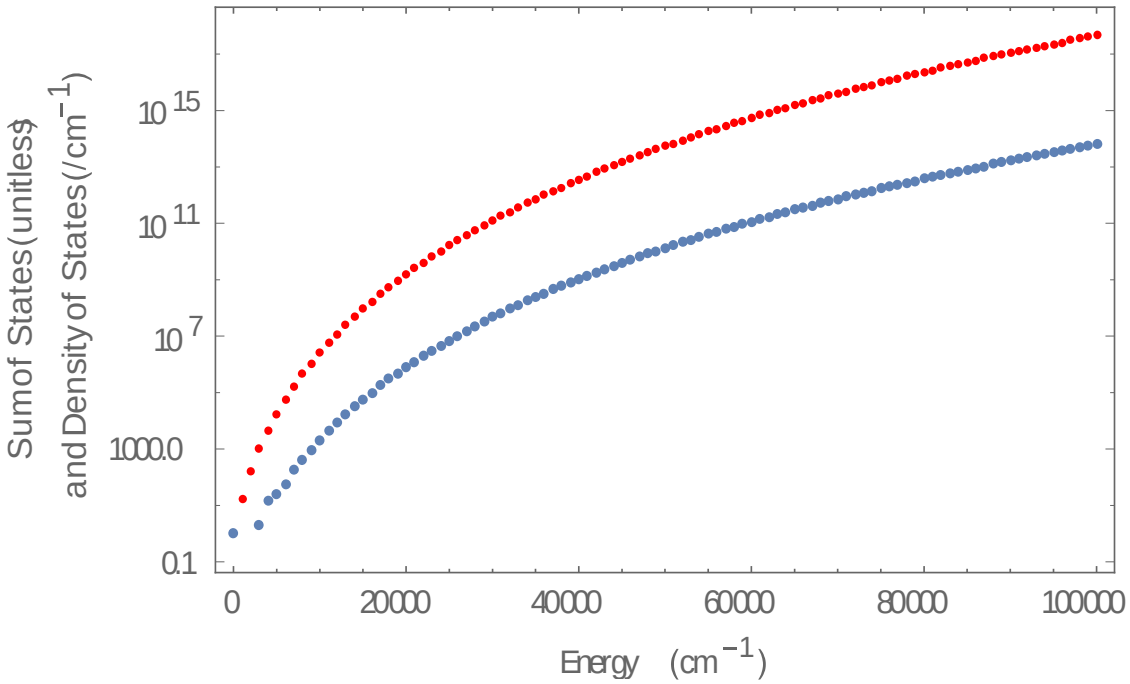

Figure 3.2 Sum and density of states of vinyl cyanide

Thus, when vinyl cyanide has an internal energy of 100000 cm^{-1}, the sum and density of quantum states are $\approx 10^{17.5}$ and $\approx 10^{14}$/wavenumber.

Notice that the Do loops for computing the sum and density of states perform the same basic process – the BS direct count method – on different initial lists. As we proceed, adopting a functional programming approach will ease the exposition and vastly improve code clarity. We do this by introducing two new functions, bsFrequencyUpdate and bsDirectCount. The first updates the list of sums/densities for a single vibrational frequency, and the second uses Fold to iteratively update for each of the vibrational frequencies in the table.

```
bsFrequencyUpdate[stateList_, v_] := Block[{out = stateList, k},
    For[k = v+1, k ≤ Length[out], k++, out[[k]] += out[[k - v]]]; out];
bsDirectCount[stateList_, vList_] := Fold[bsFrequencyUpdate, stateList, vList];
```

We then use these to create the two functions bsComputeSumOfStates and bsComputeDensityOfStates, which take a frequency list and total energy as arguments and do just as their names imply. The last argument to these functions, relEnergy, is used in Section 4.

```
bsComputeSumOfStates[vList_,energy_,relEnergy_:0]:=
    bsDirectCount[Table[1,energy-relEnergy+1],vList];
bsComputeDensityOfStates[vList_,energy_,relEnergy_:0]:=
    bsDirectCount[PadRight[{1},energy-relEnergy+1],vList];
```

For completeness, we re-compute the sum and density of states using the above functions to illustrate how that can be done. It is readily verified that these compute the same quantities.

```
bsSumOfStates = bsComputeSumOfStates[vList, energy];
bsDensityOfStates = bsComputeDensityOfStates[vList, energy];
```

Direct Count for Anharmonic Oscillators – The Stein-Rabinovitch Extension

The harmonic oscillator model assumes that the difference between successive vibrational energy levels remains constant. In real oscillators, this difference decreases as the vibrational excitation increases. These anharmonic effects increase both the sum and density of states and thus often cancel when taking the ratio to determine the RRKM rate constant in Equation 3.1. However, there are some cases where this effect does not completely cancel or where highly resolved measurements necessitate a more accurate description of the vibrational energy.

The *Stein-Rabinovitch (SR)* algorithm extends the BS method to incorporate the effects of anharmonicity into the RRKM rate constant.[22] Following ref. 10, the anharmonic effects are incorporated into the energy level expression through the equation

$$E(n) = v_e\left(n+\frac{1}{2}\right) - v_e\chi_e\left(n+\frac{1}{2}\right)^2 \qquad (3.2)$$

$$n = 0, 1, 2, \ldots$$

where E(n) is the energy of the n^{th} vibrational level, v_e is the vibrational frequency and x_e is the anharmonicity constant. The SR extension counts each energy level of the anharmonic model to calculate the sum and density of states in a way that is functionally similar to the BS method; however, the input table is modified to include the anharmonicity constant for each vibrational mode. For this example, we have organized the anharmonicity constants, x_i, into the table xList. Using the vibrational frequencies of vinyl cyanide from reference 23, and assigning 0.01 as the anharmonicity constant for each vibration, the energy for each level of each mode can be calculated:

```
xList = Table[1/100,{i, nFreqs}];

vEnergies[vList_, xList_]:=Block[{nFreqs = Length[vList], i, n},
```

```
Round@Table[
 {ν,x}={vList[[i]], xList[[i]]};
 ν+ν n (1-n x),
 {i,nFreqs},{n,0,1/2 ((1/xList[[i]])-1)}] ]
```

With these we can calculate the sum and density of states, initializing the lists in the same manner as the BS method (a list of 1's for the sum of states, and a 1 followed by 0's for the density of states). The process is functionally similar to that used to calculate the sum and density of states for a set of harmonic oscillators. In the BS method, the elements of a single table are modified with each iteration of the inner loop. By contrast, in the SR extension the elements of the table are updated through separable computations combined after each complete loop for each oscillator.

```
srShift[stateList_,v_]:=Table[0,v]~Join~Drop[stateList,-v];
srShiftListTotal[stateList_,vList_]:=
        Total@ParallelMap[srShift[stateList,#]&,Prepend[vList,0]];
srCount[stateList_,listOfvLists_]:=Fold[srShiftListTotal,stateList,listOfvLists];
```

The implementations can be verified by replicating the calculations in the appendix of reference 22, which shows the calculation of the density of states up to 10 units of energy for a model system with two oscillators. The energies of the first oscillator are {2, 2, 4, 7} and the energies of the second are {0, 0, 2, 5}:

```
FoldList[
 srShiftListTotal,
 {1,0,0,0,0,0,0,0,0,0,0},
 {{2,2,4,7},{0,0,2,5}} ]//TableForm
```

```
{{1, 0, 0, 0, 0, 0, 0, 0, 0, 0, 0},
 {1, 0, 2, 0, 1, 0, 0, 1, 0, 0, 0},
 {3, 0, 7, 0, 5, 1, 1, 5, 0, 2, 0}}
```

With these, we can define SR analogues to bsComputeSumOfStates and bsComputeDensityOfStates

```
srComputeSumOfStates[vList_,xList_,energy_,relEnergy_:0]:=
  srCount[Table[1, energy - relEnergy+1],vEnergies[vList,xList]];
srComputeDensitiesOfStates[vList_,xList_,energy_,relEnergy_:0]:=
  srCount[PadRight[{1}, energy - relEnergy+1],    vEnergies[vList,xList]];
```

and use them to compute the SR sum and density of states:

```
srSumOfStates = srComputeDensitiesOfStates[vList,xList,energy];
srDensityOfStates = srComputeDensitiesOfStates[vList,xList,energy];
```

Below are two plots comparing the harmonic and anharmonic models for the density and sum of states calculated for vinyl cyanide.

```
Show[
ListLogPlot[takeEvery[1000]@Transpose[{Range[0, energy],
        bsDensityOfStates}],  PlotStyle->Red],
ListLogPlot[takeEvery[1000]@Transpose[{Range[0, energy],
        srDensityOfStates}]],  Frame->True,FrameLabel->{"Energy (cm^-1)",
        "Density of States (/cm^-1)"}]
```

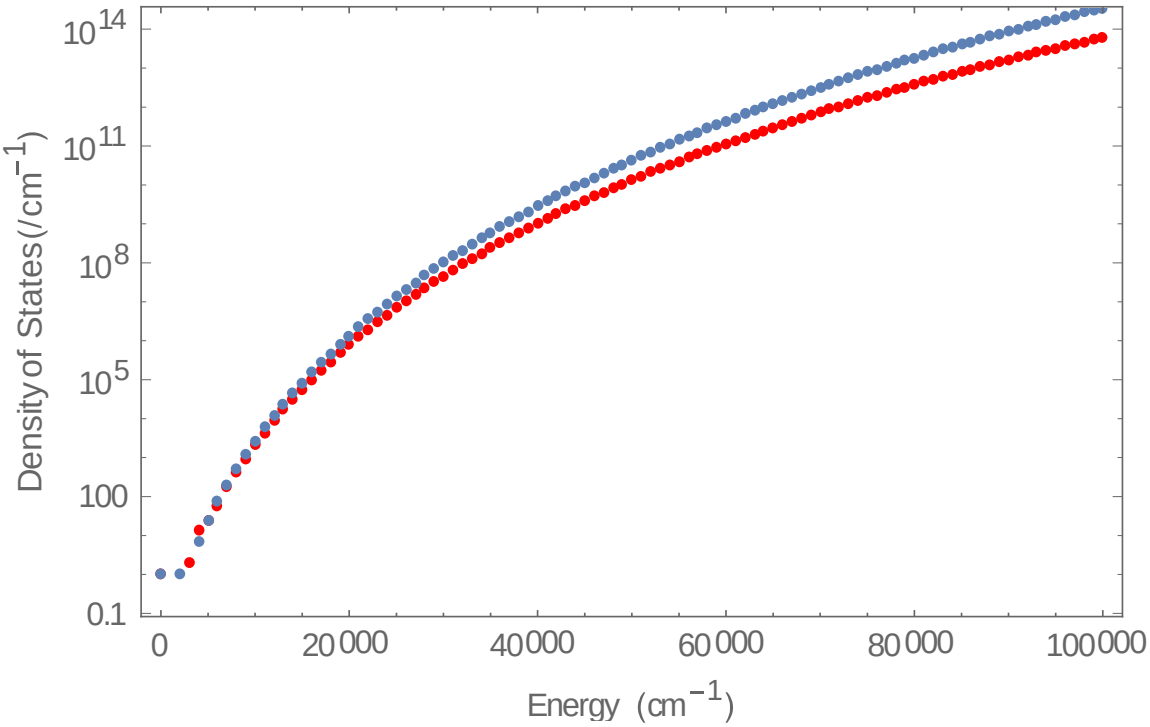

Figure 3.3 harmonic and anharmonic density of states of vinyl cyanide

```
Show[
 ListLogPlot[takeEvery[1000]@Transpose[{Range[0,energy],bsSumOfStates}],
      PlotStyle->Red],
 ListLogPlot[takeEvery[1000]@Transpose[{Range[0,energy],srSumOfStates}]],
      Frame->True, FrameLabel->{"Energy (cm-1)",
      "Density of States (/cm1)"}]
```

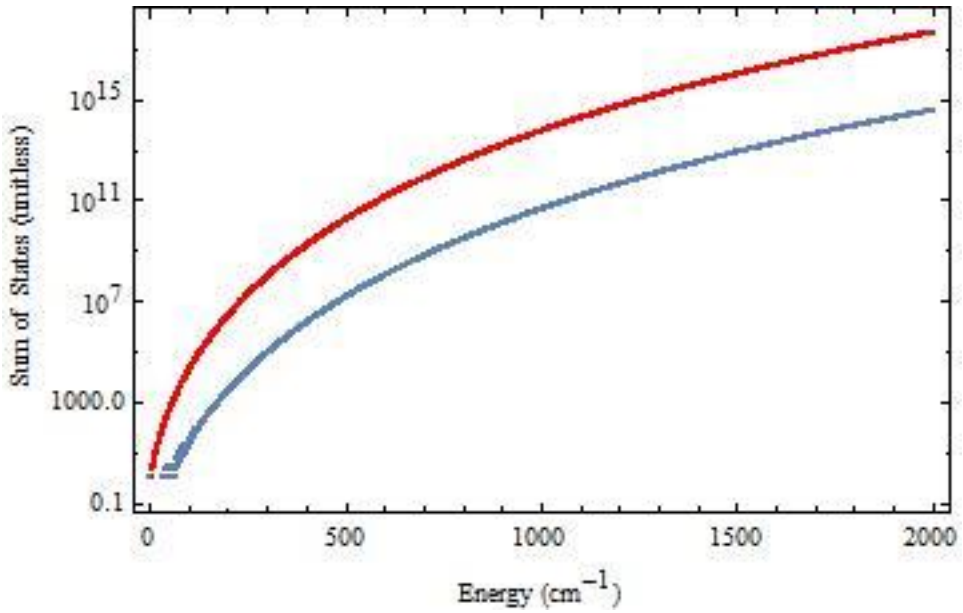

Figure 3.4 harmonic and anharmonic sum of states of vinyl cyanide

Dissociation of Vinyl Cyanide ($C_3 H_3N$)

As a more substantive example, we calculate rate constants for the decomposition of vinyl cyanide (VC, CH_2CHCN) into hydrogen cyanide (HCN), hydrogen isocyanide (HNC) and acetylene ($C_2 H_2$), compare them to published values, and interactively visualize the temporal dependence of the various species. In reference 23, Homayoon and colleagues considered the following kinetic model that involved seven different paths, three different intermediates, thirteen rate constants and three different products:

Path I

$$VC \xrightarrow{k_1} HCCH + HCN$$

Path II

$$VC \overset{k_2}{\rightleftharpoons} HCCH + HCN$$

Path III

$$VC \underset{k_4}{\overset{k_3}{\rightleftharpoons}} Int1_{III} \xrightarrow{k_5} HCCH + HCN$$

Path IV

$$VC \underset{k_7}{\overset{k_6}{\rightleftharpoons}} Int1_{IV} \overset{k_8}{\Rightarrow} HCCH + HNC$$

Path V

$$VC \underset{k_{10}}{\overset{k_9}{\rightleftharpoons}} Int1_{V} \overset{k_{11}}{\Rightarrow} HCCH + HCN$$

Path VI

$$Int1_{III} \overset{k_{12}}{\Rightarrow} HCCH + HNC$$

Path VII

$$Int1_{III} \overset{k_{13}}{\Rightarrow} HCCH + HNC$$

Each step of each path passes through a transition state to yield either an intermediate or a final product. The following differential rate equations characterize the temporal dependence of the amounts of each species.

$$\frac{d}{dt}VC = -(k_1 + k_2 + k_3 + k_6 + k_9)VC(t) + k_4 Int1_{III}(t) + k_7 Int1_{IV}(t) + k_{10} Int1_V(t) \quad (3.3)$$

$$\frac{d}{dt}Int1_{III} = k_3 VC(t) - k_4 Int1_{III}(t) - k_5 Int1_{III}(t) - k_{12} Int1_{III}(t) - k_{13} Int1_{III}(t) \quad (3.4)$$

$$\frac{d}{dt}Int1_{IV} = k_6 VC(t) - k_7 Int1_{IV}(t) - k_8 Int1_{IV}(t) \quad (3.5)$$

$$\frac{d}{dt}Int1_{V} = k_9 VC(t) - k_{10} Int1_V(t) - k_{11} Int1_V(t) \quad (3.6)$$

$$\frac{d}{dt}HCN = (k_1 + k_2)VC(t) + k_5 Int1_{III}(t) \quad (3.7)$$

$$\frac{d}{dt}HNC = k_8 Int1_{IV}(t) + k_{11} Int1_V(t) + k_{12} Int1_{III}(t) + k_{13} Int1_{III}(t) \quad (3.8)$$

$$\frac{d}{dt}HCCH = k_2 VC(t) + k_5 Int1_{III}(t) + k_8 Int1_{IV}(t) + k_{13} Int1_{III}(t) + k_1 VC(t) + k_{11} Int1_V(t) + k_{12} Int1_{III}(t) \quad (3.9)$$

The determination of the sum and density of states requires the vibrational frequencies for each species located at minima and maxima along the reaction pathway. For the decomposition reaction of vinyl cyanide, there are six minima (the geometry of VC along with each intermediate) and 11 maxima (each unique transition state). These seventeen sets of frequencies are taken from reference 23 and are provided in Table 3.1. Here we have chosen the same notation as in reference 23. TS indicates a transition state, the particular path is indicated by a roman numeral and the minimum energy of each species, relative to the minimum energy of vinyl cyanide is prefaced with re.

We now turn to the calculation of the sum and density of states and then use the values to calculate each rate constant. We begin by defining the vibrational constants.

νVC={235, 344, 570, 696, 872, 980, 1005, 1118, 1331, 1467, 1689, 2322, 3173, 3214, 3271};

(* Path I *)

$\nu TS1_{I}$={127, 184, 276, 521, 596, 778, 898, 953, 1353, 1615, 2187, 2272, 3153, 3271};

(* Path II *)

$\nu TS1_{II}$={49, 106, 301, 384, 627, 696, 760, 790, 907, 1853, 2085, 2168, 3353, 3427};

(* Path III *)

$\nu TS1_{III}$={237, 413, 604, 685, 958, 1013, 1044, 1303, 1415, 1652, 1979, 3175, 3264, 3280};

$\nu Int1_{III}$={192, 237, 520, 707, 893, 942, 988, 1141, 1345, 1458, 1698, 2208, 3182, 3230, 3284};

Table 3.1 Vibrational frequencies for vinyl cyanide and each intermediate and transition state (each with one imaginary frequency) in the decomposition reaction. Values taken from reference 23.

Species	Frequencies (cm^{-1})														
VC	235	344	570	696	872	980	1005	1118	1331	1467	1689	2322	3173	3214	3271
TS1 - I	127	187	276	521	596	778	898	953	1353	1615	2187	2272	3153	3271	
TS1-II	49	106	301	384	627	696	760	790	907	1853	2085	2168	3353	3427	
TS1-III	237	413	604	685	958	1013	1044	1303	1415	1652	1979	3175	3264	3280	
Int1-III	192	237	520	707	893	942	988	1141	1345	1458	1698	2208	3182	3230	3284
TS2-III	124	253	338	405	600	678	891	900	976	1759	1877	2123	3303	3403	
TS1-IV	411	469	570	597	753	954	970	1076	1272	1365	1778	2120	3047	3211	
INT1-IV	452	457	713	844	845	890	930	1048	1146	1281	1576	1832	3245	3281	3516
TS2-IV	346	392	503	633	715	917	989	1088	1278	1444	2113	3050	3124	3718	
INT2-IV	229	344	516	591	670	739	941	990	1156	1254	1414	2122	2981	3116	3692
TS3-IV	78	282	525	630	632	687	871	882	1156	1708	1837	3320	3364	3625	
TS1-V	208	255	428	584	718	881	972	1081	1481	1686	1974	2338	3126	3220	
Int1-V	162	221	379	589	866	904	953	1073	1147	1489	1707	2206	3132	3214	3498
TS2-V	84	115	272	401	436	474	664	803	1289	1651	2113	3128	3284	3839	
INT2-V	74	76	148	157	164	436	743	772	779	1258	1704	2093	3137	3230	3579
TS1-VI	111	150	210	447	466	835	853	920	1308	1624	2053	2176	3143	3260	
TS1-VII	40	132	330	395	615	682	855	877	935	1813	2060	2097	3329	3409	

$\nu TS2_{III}$={124, 253, 338, 405, 600, 678, 891, 900, 976, 1759, 1877, 2123, 3303, 3403};

(* Path IV *)

$\nu TS1_{IV}$={411, 469, 570, 597, 753, 954, 970, 1076, 1272, 1365, 1778, 2120, 3047, 3211};

$\nu Int1_{IV}$={452, 457, 713, 844, 845, 890, 930, 1048, 1146, 1281, 1576, 1832, 3245, 3281, 3516};

$\nu TS2_{IV}$={78, 282, 525, 630, 632, 687, 871, 882, 1156, 1708, 1837, 3320, 3364, 3625};

(* Path V *)

$\nu TS1_{V}$={208, 255, 428, 584, 718, 881, 972, 1081, 1481, 1686, 1974, 2338, 3126, 3220};

$\nu Int1_{V}$={162, 221, 379, 589, 866, 904, 953, 1073, 1147, 1489, 1707, 2206, 3132, 3214, 3498};

$\nu TS2_{V}$={84, 115, 272, 401, 436, 474, 664, 803, 1289, 1651, 2113, 3128, 3284, 3839};

(* Path VI *)

$\nu TS1_{VI}$={111, 150, 210, 447, 466, 835, 853, 920, 1308, 1624, 2053, 2176, 3143, 3260};

(* Path VII *)

$\nu TS1_{VII}$={40, 132, 330, 395, 615, 682, 855, 877, 935, 1813, 2060, 2097, 3329, 3409};

Because the internal energy is defined relative to the well depth of vinyl cyanide, the sums and densities of states for the other species must be calculated using energy adjusted by the lowest energy of each species relative to the lowest energy of vinyl cyanide (peak height for the transition states and well depth for the intermediates).

```
reVC=0;
reTS1I=35185;
reTS1II=41271;
reTS1III=20076;
reInt1III=7380;
reTS2III=40327;
reTS1IV=37494;
reInt1IV=17418;
reTS2IV=29939;
reTS1V=36724;
reInt1V=13675;
reTS2V=33402;
reTS1VI=38508;
reTS1VII=40292;
```

Beyer Swinehart Sum and Density of States

Using bsComputeSumOfStates and bsComputeDensityOfStates from Section 1, we can now compute the sums and densities of states in parallel.

```
sumsOfStates = Parallelize@MapThread[bsComputeSumOfStates[#1, energy,
#2]&,{
```

```
    {vTS1I, vTS1II, vTS1III, vTS2III, vTS1IV, vTS2IV, vTS1V, vTS2V, vTS1VI,
  vTS1VII},
    {reTS1I, reTS1II, reTS1III, reTS2III, reTS1IV, reTS2IV, reTS1V, reTS2V,
  reTS1VI, reTS1VII}}];
densitiesOfStates = Parallelize@MapThread[bsComputeDensityOfStates[#1,
  energy, #2]&,{
    {vVC, vInt1III, vInt1IV, vInt1V},
    {reVC, reInt1III, reInt1IV, reInt1V}}];
```

Rate Constants

Using equation 3.1, we now compute the 13 rate constants, taking care to avoid indeterminate values such as 0/0:

```
h =
QuantityMagnitude@UnitConvert[Quantity[1,"PlanckConstant"],"SIBase"]*5.03
4*10^22;
(* Multiplying by 5.034*10^22 incorporates the conversion of Wavenumbers to
Joules into the rate constant determination step*)
ple[vec_]:=PadLeft[vec,energy+1];(* PadLeft to same length as energy *)
paddedDivide[x_,y_]:=Quiet[ple[x]/ple[y]]/.{ComplexInfinity -> 0, Indeterminate
-> 0}
{k1,k2,k3,k4,k5,k6,k7,k8,k9,k10,k11,k12,k13}=
 MapThread[paddedDivide,{
   sumsOfStates[[{1,2,3,3,4,5,5,6,7,7,8,9,10}]],
   h densitiesOfStates[[{1,1,1,2,2,1,3,3,1,4,4,2,2}]]}];
```

The rate constants can now be visualized. Note that as energy increases, all the reaction rates also increase.

```
Show[
 ListLinePlot[takeEvery[1000]@Transpose[{Range[0,energy],Log10[k1]}]],
 ListLinePlot[takeEvery[1000]@Transpose[{Range[0,energy],Log10[k2]}],
  PlotStyle -> Orange],
 ImageSize -> 400, Frame -> True,FrameLabel->{"Energy (cm^-1)","k(E)  (s^-1)"},
 FrameTicks -> {Automatic,{#,HoldForm[10^#]}&/@Range[0, 40, 2]} ]
```

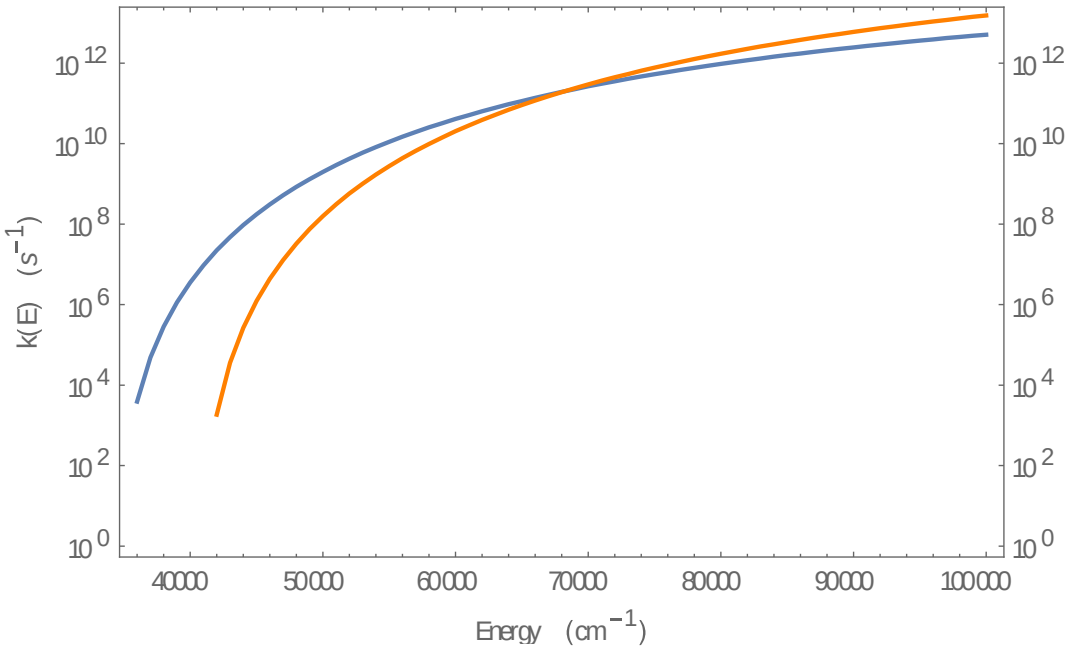

Figure 3.5 Energetic dependence of k_1 and k_2

Temporal Dependence of the Various Species

The temporal dependence of the relative concentrations of each stable species (precursor, intermediates and products) can be determined using the rate equations and NDSolve. The reaction dynamics of the decay of the precursor vinyl cyanide, the subsequent build up and decay of the intermediates, and the formation of products, each

normalized with respect to VC, are plotted at a given internal energy determined by a variable slide bar.

```
{κ1,κ2,κ3,κ4,κ5,κ6,κ7,κ8,κ9,κ10,κ11,κ12,κ13} =
takeEvery[2000]/@{k1,k2,k3,k4,k5,k6,k7,k8,k9,k10,k11,k12,k13};
Manipulate[
 (* Numerically solve rate equations *)
 pS = (p-20000)/2000+20000/2000+1;
    concentrationCurves = Evaluate[{VC[t], Int1III[t], Int1IV[t], Int1V[t], HCN[t],
HNC[t], HCCH[t]}/.
   NDSolve[{
     h^-1 VC'[t] == -(κ1[[pS]] + κ2[[pS]] + κ3[[pS]] + κ6[[pS]] + κ9[[pS]])VC[t] +
κ4[[pS]]Int1III[t] + κ7[[pS]]Int1IV[t]+ κ10[[pS]]Int1V[t],
          h^-1 Int1III'[t] == κ3[[pS]]VC[t]-(κ4[[pS]] +κ5[[pS]] +κ12[[pS]]
+κ13[[pS]])Int1III[t],
          h^-1 Int1IV'[t] == κ6[[pS]]VC[t]-(κ7[[pS]]+κ8[[pS]])Int1IV[t],
          h^-1 Int1V'[t] == κ9[[pS]]VC[t]-(κ10[[pS]]+κ11[[pS]])Int1V[t],
          h^-1 HCN'[t] == (κ1[[pS]]+κ2[[pS]])VC[t]+κ5[[pS]]Int1III[t],
          h^-1 HNC'[t] ==
κ8[[pS]]Int1IV[t]+κ11[[pS]]Int1V[t]+(κ12[[pS]]+κ13[[pS]])Int1III[t],
          h^-1 HCCH'[t] ==
(κ1[[pS]]+κ2[[pS]])VC[t]+(κ5[[pS]]+κ12[[pS]]+κ13[[pS]])Int1III[t]+κ8[[pS]]Int1I
V[t]+κ11[[pS]]Int1V[t],
```

```
    VC[0] == 1,Int1III[0] == 0,Int1IV[0] == 0,Int1V[0] == 0,HCN[0] == 0,HNC[0]
== 0,HCCH[0] == 0
    },{VC,Int1III,Int1IV,Int1V,HCN,HNC,HCCH},{t,0,1.5}
   ](* End NDSolve *)
  ];
 (* Plot concentration curves *)
 Plot[
  concentrationCurves,{t,0,1.5},PlotRange->{{0,1.5},{-.05,1.05}},
  ImageSize->320,Frame->True,FrameStyle->Directive[12,Thickness[.0025]],
  PlotStyle->{{Red},{Green},{Blue},{Black},{Gray},{Cyan},{Magenta}},
  FrameLabel->{Text@Style["Time (10^-13 s)",12],Text@Style["Relative
Abundance",12]},
  PlotLegends->LineLegend[{ Red, Green, Blue, Black, Orange, Cyan, Magenta},
{"VC","Int1III","Int1IV","Int1V","HCN","HNC","HCCH"}]
  ],
 (* Set Manipulate parameters *)
 {{p, 62000, Text@Style[ "Energy (cm^-1)",12]}, 20000, 100000, 2000},
 SaveDefinitions->True ]
```

A number of qualitative and quantitative results can be gleaned by simple inspection of figure 3.6. For example, the amount of time it takes for the reaction to run to completion, as energy increases. The plot also indicates that there is never a significant amount of any intermediate apart from that in path III. This is not surprising, given the

significantly lower energy for the first transition state in path III relative to the first transition state in pathways IV and V, and given that three pathways share $Int1_{III}$.

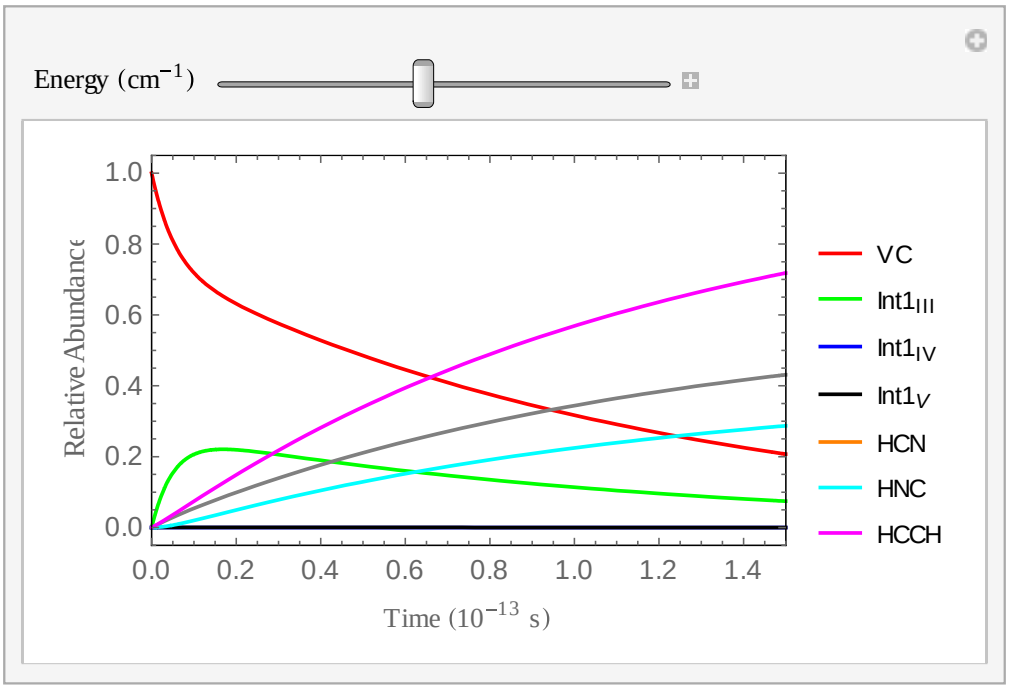

Figure 3.6 Still shot of manipulate plot showing the temporal dependence of vinyl cyanide, intermediates and products

Product Distribution Ratios

A final element determined from this analysis is the exit channel ratios (or product distribution ratios) determined at reaction completion and for a specific system internal energy. This is important because many experimental measurements are only capable of measuring product ratios as a function of precursor internal energy. Thus, experimental scientists require such an RRKM analysis to provide a dynamic and atomistic picture of the chemical reaction. The following code determines and plots the final HNC:HCN ratio at internal energies up to 100000 cm^{-1}.

Do[mechanism$_p$=

```
 NDSolve[{
        h^-1 VC'[t]==-(k1[[p]]+ k2[[p]]+ k3[[p]]+ k6[[p]]+ k9[[p]])VC[t]+
k4[[p]]Int1III[t]+ k7[[p]]Int1IV[t]+ k10[[p]]Int1V[t],
        h^-1 Int1III'[t]== k3[[p]]VC[t]-(k4[[p]]+ k5[[p]]+ k12[[p]]+
k13[[p]])Int1III[t],
        h^-1 Int1IV'[t]==k6[[p]]VC[t]-(k7[[p]]+ k8[[p]])Int1IV[t],
        h^-1 Int1V'[t]==k9[[p]]VC[t]-(k10[[p]]+ k11[[p]])Int1V[t],
        h^-1 HCN'[t]==(k1[[p]]+k2[[p]])VC[t]+k5[[p]]Int1III[t],
        h^-1 HNC'[t]== k8[[p]]Int1IV[t]+ k11[[p]]Int1V[t]+ (k12[[p]]+
k13[[p]])Int1III[t],
        h^-1 HCCH'[t]== (k1[[p]]+ k2[[p]])VC[t]+ (k5[[p]]+ k12[[p]]+
k13[[p]])Int1III[t]+ k8[[p]]Int1IV[t]+ k11[[p]]Int1V[t],
VC[0]==1,Int1III[0]==0,Int1IV[0]==0,Int1V[0]==0,HCN[0]==0,HNC[0]==0,HCC
H[0]==0
   },{VC,Int1III,Int1IV,Int1V,HCN,HNC,HCCH},{t,10^13}],{p,21000,100000,100}]
productRatios =
Table[{p,First@Quiet[HNC[10^13]/HCN[10^13]/.mechanismp]},{p,21000,100000,1
000}]/.{Indeterminate->0};
ListLinePlot[
 productRatios,
 AxesOrigin->{0,0}, Frame->True,FrameLabel->{"Energy (cm^-1)", "HNC:HCN
at t = 1s"}]
```

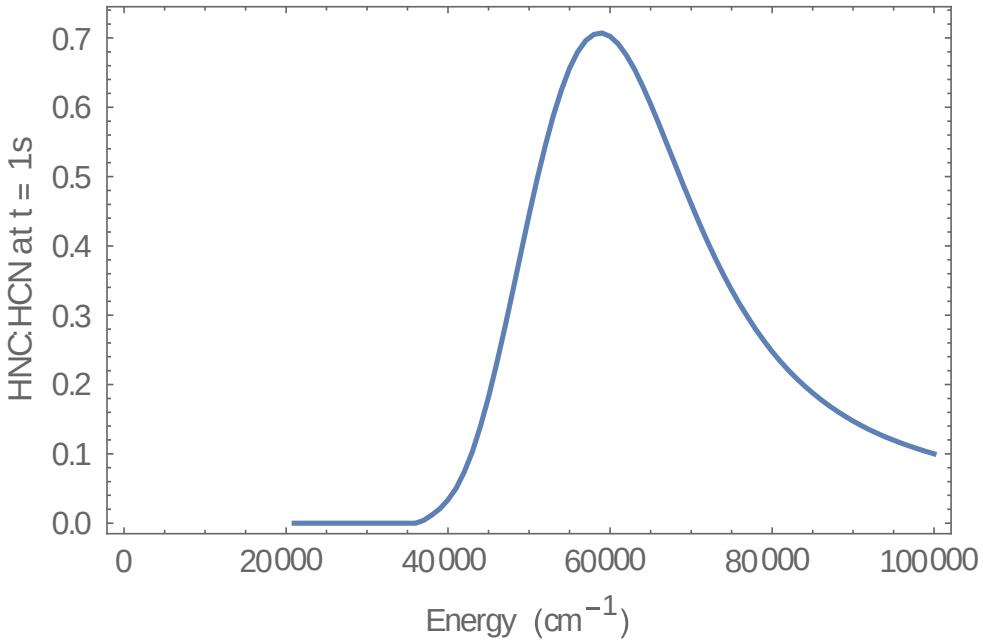

Figure 3.7 Energetic dependence of HNC:HCN product ratios

The energy at which HNC reaches its maximum relative abundance can be determined by

SortBy[productRatios,Last]//Last

{59000,0.707044}

The plot above indicates that HCN production is favored at all system internal energies. Isocyanide (HNC) only becomes a noticeable product at a system internal energy above 30000 cm^{-1}. This is due to paths IV-VII becoming competitive with path I at higher energies. Surprisingly, the product ratio reduces at energies greater than 58800 cm^{-1} (equivalently, there is a maximum in the product distribution curve). This result would be difficult to predict, even qualitatively, with just the calculated rate constants, demonstrating the usefulness of the powerful tools available in *Mathematica*.

CHAPTER FOUR.

Submerged Barriers in the Ni^+ Assisted Decomposition of Propionaldehyde

This chapter published as: Mansell, A.; Theis, Z.; Gutierrez, M. G.; Nieto Faza, O.; Silva Lopez, C.; Bellert, D. J. Submerged Barriers in the Ni^+ Assisted Decomposition of Propionaldehyde. *J. Phys. Chem. A* 2016, *120*, 2275-2284

Introduction

A submerged barrier is a saddle point on a potential energy surface that exists below the separated reactant limit.[25] Catalysts lower activation barriers that separate reactants from products, and it is possible that this reduction is to an extent that only submerged barriers govern the dynamics along the reaction coordinate.[2,26-28] This situation is characteristic of a catalyst that operates with an efficiency that is limited only by the rate of collision. Such systems are of considerable importance to chemistry, particularly if the catalyst is selective toward desired products. Gas phase ion/molecule studies provide a valuable arena to investigate the fundamental interactions which dictate catalytic efficiency and selectivity removed from the complexities of the condensed phase which often limit experimental resolution. In this regard, gas phase studies supplement and enhance traditional catalysis research in addition to providing benchmark measurements for the theoretical community.

The importance of modeling catalysis with ion/molecule reactions has prompted numerous advances in mass spectrometry.[9,10,31] In this respect, Guided-Ion Beam (GIB) techniques have been among the most important and successful. GIB measures the reaction cross section (σ) for an ion/molecule system as a function of collision energy.[32]

Typically, these experiments can be divided into two main classes. The most common involves a bimolecular collision between reaction partners whereas the other uses a collision with an inert compound (typically a rare gas atom such as Xe) to induce unimolecular dissociation of the reactant precursor. In both techniques, σ is determined by directing the ion into a collision cell with specified translational energy and the subsequent mass spectral peak intensities monitored. Thus, σ represents the probability that a collision of a given energy will generate products. Reaction kinetics are acquired by multiplying σ by the relative velocity of the reactants ($k(E) = \sigma v$) to yield second order rate constants.

Bimolecular GIB studies of group 10 cations can provide details of the potential energy surface at energies above the separated reactant limit.[33-39] These studies have yielded zero Kelvin bond dissociation energies for many systems as well as room temperature rate coefficients for low energy reactions.[40] Additionally, isotopic labeling experiments have provided valuable mechanistic insights,[39, 41-43] and the specificity of Ni^+ has been nicely demonstrated by such studies.[39,44] Threshold collisional activation (TCA) represents the unimolecular class of GIB.[24] TCA has the distinct advantage of sampling the potential energy surface below the separated reactant limit and submerged barrier energies have been quantified in several transition metal/alkane systems using this technique.[45-47]

Another prominent unimolecular technique apart from GIB is kinetic energy release distributions (KERD). Like TCA, KERD can determine the energy of submerged barriers.[42-43,48] In KERD, metastable precursor ions are generated, mass selected, and allowed to dissociate prior to kinetic energy analysis. The energy difference between

submerged barriers and separated reactants are estimated by modeling the experimental KERD using statistical phase space theory. Knowledge of the cluster bond energy in addition to this energy difference provides the submerged barrier height.[48]

The technique pioneered in our research group makes direct kinetic measurements of ion/molecule reactions within the energy regime of TCA and KERD and with improved energy resolution.[49-53] There are similarities between our technique and the more traditional approaches described, but the key difference is that precursor ions are cooled in supersonic expansion and formed into binary clusters prior to laser photon activation. The isolated clusters absorb a quantum of photon energy and if the quanta is at an energy greater than the highest submerged barrier, but less than the cluster adiabatic bond energy, the precursor rearranges and fragments into products exothermic with respect to separated reactants. These single photon initiated dissociative rearrangement reactions (SPIDRR) allow for real time monitoring of fragment production from which the microcanonical rate constant $k(E)$ can be extracted. Figure 4.1 compares the energetic range and kinetics studied by SPIDRR, TCA and KERD to those acquired through bimolecular studies. In the following kinetic study, we determine the activation barriers for the Ni^+ induced decarbonylation of propionaldehyde. Our results suggest that the decarbonylation coordinate can be made selective by the energy supplied to the reaction.

Methods

This current work is a collaborative effort between theory and experiment to extend our studies of rearrangement decomposition reactions initiated by an absorbed photon and mediated by the naked Ni^+ cation. Here, the submerged barriers that separate

the Ni^+(propionaldehyde) encounter complex from products are experimentally measured and their associated mechanistic pathways computationally explored.

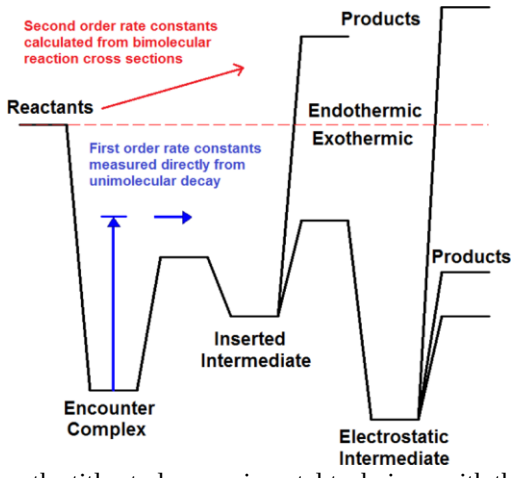

Figure 4.1 Comparison between the title study experimental technique with the more conventional bimolecular approach.

(*Experimental*) In general, the Ni^+/C_3H_6O reactants are formed as a binary cluster in a laser vaporization / supersonic expansion source. The cold precursor ion is the encounter complex (EC) that undergoes a photo-initiated decarbonylation reaction (Figure 4.1). The quantum of absorbed photon energy closely approximates the total energy of the cluster as absorption occurs in the collisionless environment of the cold, supersonic expansion. Unimolecular decay ensues as the cation selectively activates bonds within the propionaldehyde molecule and mediates the formation of products. The resulting fragment ions are selectively detected and their production temporally monitored in a custom time of flight mass spectrometer.

More specifically, a pulse of KrF eximer radiation is focused onto a pure nickel target within a large vacuum chamber. The ensuing vaporization products are entrained in a helium pulse that is doped with the vapor pressure of propionaldehyde. Collisions within the source volume form the $Ni^+(C_3H_6O)$ encounter complex. The expanding

plume is skimmed twice as it travels through ~80 cm of field free space before entering into a Wiley-McLaren, pulsed orthogonal accelerator (OA).[14] The OA is situated at the entrance to a custom time of flight mass spectrometer. As the densest portion of the ion packet enters the parallel capacitor plates, the OA is pulsed from ground to +1.75 kV potential, imparting this kinetic energy to the ions. Mass separation occurs as the ions drift through the 1.8 meter field free flight of the TOFMS. The separated ion packets enter a voltage controlled hemispherical kinetic energy analyzer (or sector). The potential difference across the halves of the sector can be selected to transmit the full kinetic energy of the ion beam, thus allowing the different ionic species produced in the expansion to strike a Chevron microchannel plate (MCP) detector located at the sector's terminus. A 500 shot averaged precursor mass spectrum is shown in Figure 4.2.

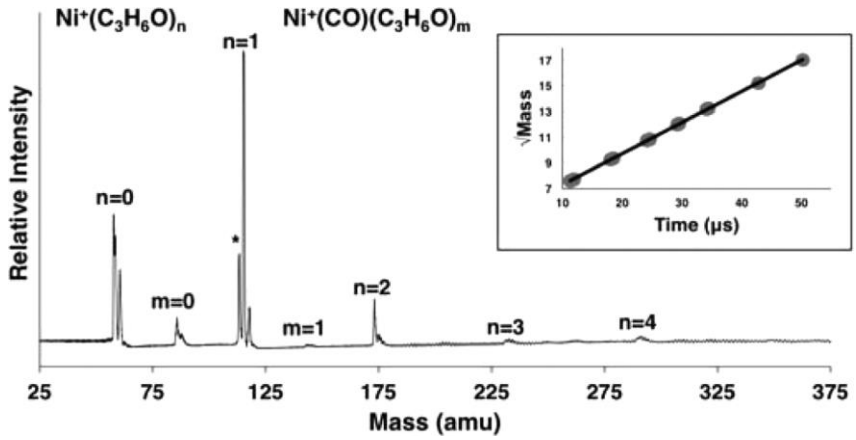

Figure 4.2 Typical precursor mass spectrum. The inset plots the square root of mass against time to calibrate the mass spectrum. The starred peak has a calculated mass of 114 amu. The corresponding system with this mass could not be photodissociated upon intense irradiation with either 532 or 355 nm light suggesting that it is not a cluster containing the Ni^+ cation

The calibration curve is shown as the inset with the mass of every labeled peak included as calibrants. Here, the voltage to the horizontal deflector was increased as the signal was averaged. This turns higher masses into the plane of the detector providing a more complete picture of the clusters produced in the source. This also attenuates the

low mass signal, slightly changes the time of ion arrival at the detector, and reduces the apparent mass resolution.

Mass peaks labeled by n and m = 0 indicate Ni^+ and Ni^+CO. The 58:60 isotopic ratios in Figure 4.2 do not match the natural relative nickel isotopic abundances. This is either due to electronic saturation of our detector (evident by baseline drops just past the n=0 and n=1 peaks) or, possibly, the presence of the $(C_3H_6O)_n^+$ ion contaminating each $^{58}Ni^+$ peak. The Ni^+CO mass peak is likely formed by unquenched $Ni^+(C_3H_6O)$ decarbonylation reactions that occur in the source region. It is very common in these studies to observe the fragment ion peak in the precursor mass spectrum. Although source conditions could be modified to both enhance and attenuate the intensity of the Ni^+CO peak, no other fragment peaks were observed resulting from the runaway precursor decomposition in the source. Subsequent mass peaks labeled by m = 1 and n = 1- 4 indicate propionaldehyde molecules clustering onto the Ni^+ and Ni^+CO cations. Such clustering is suggestive of the rather cold conditions typical to supersonic expansions. Indeed the internal energy of the precursor cation is reduced by establishing source conditions that minimize the precursor velocity distribution and it is under these conditions that such clustering becomes most evident in the mass spectra. The precursor velocity distribution is sampled by measuring the time required for the ions to span the ~80 cm distance between the pulse valve and OA center. The time difference is estimated by subtracting the time values between trigger pulses sent to the OA and vaporization excimer laser (the time difference between formation of the ions and right angle extraction from the molecular beam). Thus, measurements of displacement over time provide an estimate to the parallel velocity component of the precursor ions within

the supersonic beam. Figure 4.3 presents such a velocity distribution for the precursor $Ni^+(C_3H_6O)$ clusters. It is noteworthy that the center velocity within the distribution, 1.59 x 10^3 m/s, approaches terminal velocity, 1.77 x 10^3 m/s, for a pure helium expansion.

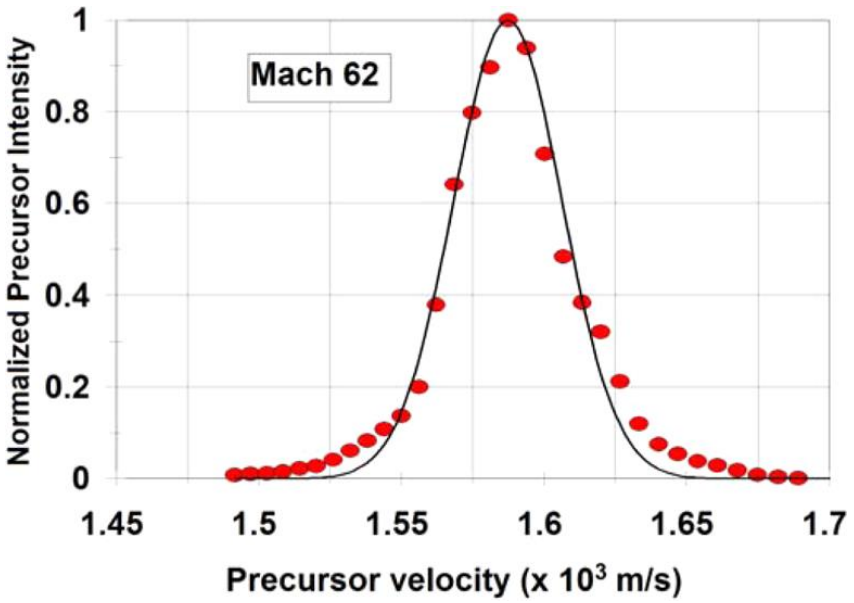

Figure 4.3 Precursor velocity distribution. The curve is fit to equation 2.1 For a temperature = 0.25 K.

The solid curve through the points is determined by fitting to the velocity distribution expected for a collimated supersonic beam,[55-57]

$$f(v) = Nv^3 e^{\left(-\frac{m(v-\bar{u})^2}{2kT}\right)} \tag{2.1}$$

where *T* is the local temperature, is the average parallel velocity component of the precursor ions, *N* is a normalization constant such that the integral of the function over all space equals unity, and *m* is the weighted mass of the carrier gas (assumed to be 97% He and 3% propionaldehyde vapor). The only variable parameter in equation 2.1 is the temperature which optimizes at values less than a single Kelvin. It is common to correlate the temperature of a supersonic expansion with a Mach number, which here is

Mach 62. This approximate treatment only addresses the translational temperature of ions within our beam, however, despite our inability to unambiguously specify the beam temperature, does suggest the significant cooling associated with supersonic expansions within our apparatus.

Laser induced dissociation of precursor ions results in charged fragments that transmit through the sector at characteristic potential differences. Although the dissociation event does not significantly alter the fragment velocity, the sector transmission voltage changes in accordance with the mass of the fragment. Therefore, the various fragments resulting from laser induced dissociation of any cluster peak in Figure 4.2 can be identified by their sector transmission voltage. Dissociation induced by high energy photons is used as another tool to identify the mass peaks in Figure 4.2 as well as to suggest their geometric form. This is demonstrated in Figure 4.4 where fragment intensity as a function of transmission voltage is shown for three different photon energies and two distinct orientations of the laser field.

In the top two traces of Figure 4.4, the laser is oriented through the time-of-flight (TOF) to interrogate the molecular beam 500 ns before entering the sector. In this setup, dissociation must occur within the allotted 500 ns for successful transmission through the sector. Thus, the fast production of fragments suggests a precursor geometry where very little rearrangement occurs prior to dissociation. The top two traces of Figure 4.4 shows a peak ~330 V corresponding to the fast dissociation of $^{58}Ni^{+}(C_3H_6O)$ into $^{58}Ni^{+}$ which suggests the Ni^{+} cation is bound to the periphery of the propionaldehyde molecule. This is consistent with assignment of the EC as a component within the beam. The peak at ~505 V, seen also in the top two traces of Figure 4.4, shows the fast dissociation of

$^{58}Ni^{+}(C_3H_6O)$ into $^{58}Ni^{+}$ CO. This suggests that there is another isomer within the beam that quickly eliminates $Ni^{+}CO$. This must be a Ni^{+} cation bound to intact CO and C_2H_6 molecules, an intermediate along the reaction coordinate. We conclude that the mass peak at 118 amu in Figure 4.2 primarily contains two Ni^{+} bound isomers: the EC and the electrostatic intermediate (Figure 4.1), which is formed late along the dissociative reaction coordinate.

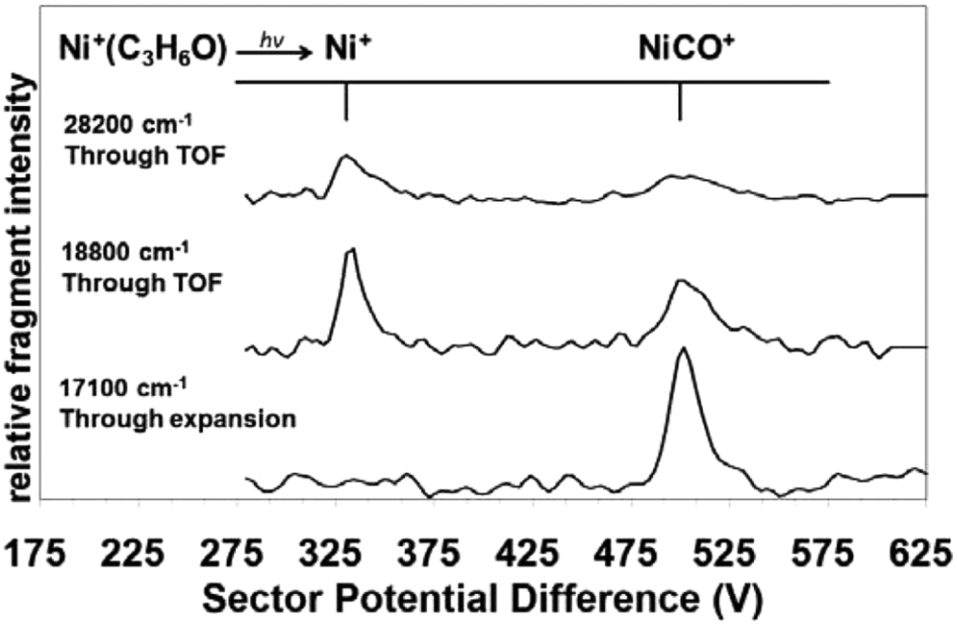

Figure 4.4 Scan of the potential difference across the sector halves to transmit photodissociated fragments from $Ni^{+}(C_3H_6O)$.

The bottom trace of Figure 4.4, where laser radiation is timed to interrogate precursor molecules five microseconds prior to orthogonal extraction, demonstrates the possible fragments resulting from relatively slow rearrangement reactions. Here, any dissociation that occurs prior to or within the extraction field will not be transmitted to the detector through our sector. The peak at 505 V again corresponds to transmission of the $^{58}Ni^{+}$ CO from the precursor $^{58}Ni^{+}(C_3H_6O)$. However, this peak must exclusively

result from rearrangement of the EC since the near barrierless decarbonylation of the electrostatic intermediate occurs on timescales too fast to be measured when laser interrogation occurs along the expansion axis. Furthermore, there is no Ni^+ peak in the bottom trace of Figure 4.4 whereas it is present in the top traces. This indicates that the production of $^{58}Ni^+$ from $^{58}Ni^+(C_3H_6O)$ occurs faster than can be sampled when excitation occurs prior to extraction.

The bottom trace of Figure 4.4, where only relatively slow dissociative processes may be sampled, shows that the $^{58}Ni^+(C_3H_6O)$ precursor ion exclusively dissociates into the $^{58}Ni^+CO$ fragment channel when energized with 17100 cm^{-1} radiation. This is corroborated by the many, single amu resolved precursor mass spectra that we have measured for this system (Figure 4.2) where again the only observed fragment has a mass that is consistent with Ni^+CO assignment. Rearrangement reaction into an isobaric cationic fragment, such as production of $Ni^+C_2H_4 + CH_2O$, is improbable. If such a exit channel existed, the large dipole moment of formaldehyde makes dissociation into $Ni^+CH_2O + C_2H_4$ far more likely but the ~3:1 isotopic pattern at mass 88 and 90 amu expected for the Ni^+CH_2O fragment is not observed. We, in fact, find no evidence of any other exit channels. Therefore, we conclude that the reaction sampled by our technique is reaction 1, the relatively slow decarbonylation of the Ni^+(propionaldehyde) encounter complex into the single exit channel indicated.

$$Ni^+(C_3H_6O) \rightarrow Ni^+CO + C_2H \qquad \text{Reaction 4.1}$$

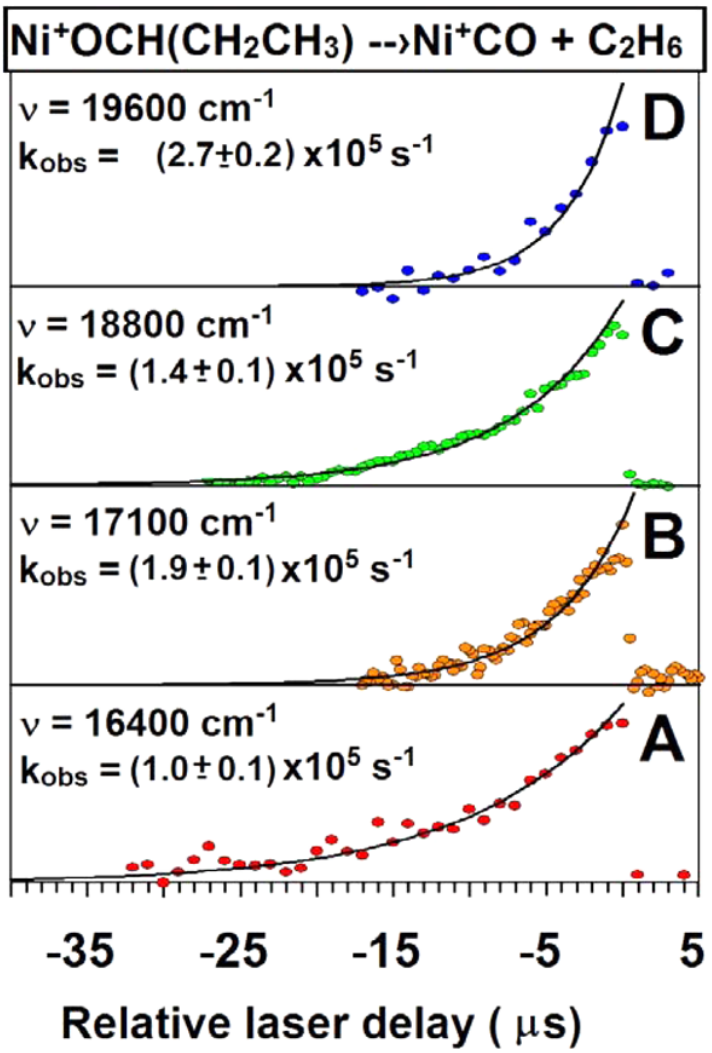

Figure 4.5 Exponential fits to the waveforms acquired in this study. The fits yield the observed rate constants (k_{obs}) at the indicated laser frequencies.

Temporal resolution of fragment production is acquired by scanning the delay between the trigger pulse to fire the dye laser and the one to charge the OA to full potential. Laser radiation intersects the counter propagating ions along the expansion axis. The jet-cooled precursor absorbs a quantum of photon energy which initiates the decarbonylation reaction. All fragment ions produced between the location of photon absorption and the OA receive the same (full) kinetic energy imparted to the precursor ions during right angle extraction and are, therefore, not sampled. Only those excited

precursor ions that decay within the field free flight of the TOF produce detectable fragments via selective transmission through the voltage tuned sector. The relative intensity of the fragment ions formed within the TOF are plotted versus the timing delay between triggering pulses to the OA and dye laser. These points combine into a waveform that is analyzed to extract the kinetic information from the rearrangement dissociative reaction.

Zero microseconds is defined to be the coincident firing of both the dye laser and the OA. The dye laser is temporally scanned to times earlier than the OA trigger pulse and thus the fragment ion intensity is plotted versus negative relative timing delay values. The four panels of Figure 4.5 show the results for the Ni^+ assisted decarbonylation reaction of propionaldehyde into the $^{58}NiCO^+$ channel. The $^{60}NiCO^+$ product channel was also monitored yielding nearly identical rate constants indicating a 58:60 kinetic isotope effect that is roughly one, as is expected.

First order rate constants have been measured and recorded for the dissociative $Ni^+(C_3H_6O)$ rearrangement reaction as evident in the panels of Figure 4.5 The dynamic range by which reaction rates may be monitored is limited in two ways in this experiment. First, the cluster must absorb a photon to couple energy into the reaction coordinate and is thus limited by the Franck-Condon factors governing electronic excitation. For studies where Ni^+ is the chromophore, this prohibits study at long wavelengths due to its fairly sparse electronic structure at low energy.[58] Second, reactions must occur with a rate within our sampling time window. Any reaction that occurs with a rate constant greater than ~1 x 10^6 s^{-1} produces fragments too quickly to be measured. However, with a residence time of roughly 400 microseconds, rate constants as small as

1.7×10^4 s^{-1} have been easily measured and it is expected that unimolecular decay lifetimes as long as a millisecond can be confidently recorded.

(*Theoretical*) The potential energy surface for the Ni^+ mediated decarbonylation of propionaldehyde has been explored computationally employing Density Functional Theory (DFT)[59,60] in order to obtain a reasonable balance between accuracy and cost. There are a number of density functionals and basis sets that can be combined to perform this task. In this work all the minima and transition state optimizations were performed with the *parameter free* functional form from Perdew, Burke and Hernzerhof (PBE)[61] coupled with the correlation consistent triple-zeta quality basis set cc-pVDZ.[62,63] This choice was driven by certain requirements: 1- we refuse to use heavily parametrized functionals, whose performance in chemistry not included in the training set may be poor; 2- the functional form should provide consistently good results for a wide range of metal mediated catalysis processes, and 3- vibrational scaling factors have to be available for the functional/basis couple since accurate thermochemistry may be desired for future experimnets. We found that scaling factors for a few GGA functionals (BLYP, BPW91, PBEPBE, HCTH93, and BP86) have reported recently with the correlation consistent family of basis sets.[62] From this small set we chose PBEPBE given its general good performance in catalysis and metal cluster chemistry.[65-68]

For all the stationary points, second derivatives of the energy with respect to nuclear displacements were computed. Harmonic analysis confirmed the nature of the stationary points and normal modes were obtained. Thermochemistry values reported have been obtained under the harmonic approximation, using a 0.9601 scaling factor for

the vibrational frequencies to obtain zero point energies. The stability of the wavefunction was also tested for all the stationary points reported in this work.[69]

In order to further refine the energetics of the potential energy surfaces computed, a coupled cluster energy evaluation was performed at the UCCSD(T)/cc-pVDZ level. The energies reported in this work are therefore a combination of UCCSD(T) electronic energies and the DFT computed enthalpic and entropic contributions, usually noted UCCSD(T)/cc-pVDZ//PBEPBE/ cc-pVDZ. This combination is designed to provide energetics of higher accuracy than what it is obtained with the use of DFT alone. All the electronic structure calculations reported in this work have been performed with Gaussian 09.[70]

(RRKM) A general RRKM program was acquired online and used to calculate the microcanonical rate constants for $Ni^+(C_3H_6O)$ decomposition.[71] The RRKM rate constant, expressed in terms of the cluster internal energy is:

$$k(E) = \frac{\sigma N^{\ddagger}(E - E_0)}{h\rho(E)} \tag{3.1}$$

where the $N^{\ddagger}$ is numerator is the transition state's sum of states, ρ(E) is the unimolecular reactant density of states, and E_0 is the threshold energy. Vibrational frequencies were calculated at the PBEPBE/cc-pVDZ level and used as input parameters to calculate the sum and density of states.

Results

(Experimental) The $Ni^+(C_3H_6O)$ EC precursor ion absorbs a visible laser photon and dissociates into $Ni^+CO + C_2H_6$. Since the Ni^+ portion of the precursor has low lying visible electronic transitions, whereas the propionaldehyde does not, it must be the

chromophore within the cluster. However, these atom-centered transitions are parity forbidden and only become weakly allowed as the dipolar field of the propionaldehyde molecule inductively lowers the spherical electronic symmetry of the Ni^+ cation. Therefore, single photon absorption promotes the cluster into an excited state that is metastable; emission to the ground state is optically forbidden and energy cannot be removed by simple cleavage of the cluster bond. Rather, the system crosses back to the ground state potential where the energy of the absorbed photon is redistributed as vibrational energy within the reactant cluster. The photo-excited precursor will rearrange and dissociate into products if its internal energy is in excess of the reaction activation requirements but less than the adiabatic bond energy of the cluster. When the photon energy is in excess of the cluster bond energy, absorption primarily leads to dissociation of the cluster into the entropically favored products—Ni^+ and propionaldehyde. Absorption of two visible photons excites the precursor to states well in excess of the cluster adiabatic bond energy (estimated as 20 kcm^{-1} from charge-dipole interactions) again forming the entropically favored Ni^+ and propionaldehyde products.

The Ni^+CO fragment ion yield is measured at a fixed laser delay value. Scanning this delay in time provides the temporal response of the unimolecular decay and this is shown in panels A-D of Figure 4.5. Each point within a panel represents from 50 to 300 shot averages of the observed fragment production at the indicated laser timing delay value. Each point is normalized to the maximum averaged Ni^+CO fragment intensity value within each panel. The solid curve is a single exponential fit to the Ni^+CO fragments yields acquired at the indicated laser energy. The rate constant in each panel is extracted from this exponential fit and is recorded as $k_{obs}(E)$, where E is the absorbed

laser energy that approximates the internal energy of the precursor ion. Ten such measurements between 16000 and 20000 cm^{-1} have been made for the photon initiated, Ni^+ assisted rearrangement decomposition of the propionaldehyde molecule. The observed *k*(E) values are provided in Table 1 and plotted against the internal energy of the precursor in Figure 4.6.

(Theoretical) The Ni^+ assisted dissociative reaction of propionaldehyde was computed at the UCCSD(T)/cc-pVDZ/PBEPBE/cc-pVDZ level of theory. Both the Ni^+CO stretching vibrational frequency, 2159 cm^{-1}, and bond energy,192 kJ/mol, were computed and verified against experimental determinations (2176 cm^{-1}, 178 ±11 kJ/mol).[72-74] The potential energy surface, Figure 4.7, shows parallel reaction coordinates initiated by either the Ni^+ activation of the C-C or aldehyde C-H bonds. Motion along the H-activation coordinate is initially less demanding as the energy required to form $TS1^{CH}$ is less than $TS1^{CC}$. The energetic demands of the ensuing rearrangement along both coordinates culminate at TS3, and the formation of this late transition state controls the reaction kinetics along both dissociative pathways. Theory predicts that the formation of $TS3^{CC}$ requires ~1000 cm^{-1} less energy than from the H-activation approach. The parallel coordinates recombine past this point forming the third intermediate and subsequent structures.

Figure 4.7 shows computed structures at critical locations along the PES. The encounter complex can be formed with any of the two lone pairs available from the carbonyl group. The most stable isomer is with the Ni^+ cation syn to the aldehyde hydrogen (the energy difference computed between the syn and ati conformeres is 8.5 kcal/mol). From this complex H or C activation occurs through TS1. The nickel hydride

resulting from the H activation must reorganize before the following insertion can take place (see Int1 to Int2 in Figure 4.7). This second metal insertion occurs at TS3, after which both reaction pathways merge.

Table 4.1 Rate Constants (x10^5 s^{-1}) from Single Exponential Fits to the Waveforms Acquired from the Title Reaction at the Internal Energies (cm^{-1}) Indicated[a]

Cluster Internal Energy	Observed k(E) (x 10^5 s^{-1})
16400	1
16900	1.6
17100	1.9
17800	2.6
18000	2.7
18250	2.6
18500	1.7
18800	1.4
19200	1.6
19600	2.7

[a.] The error in each measurement is less than 10% as determined through linear regression analysis.

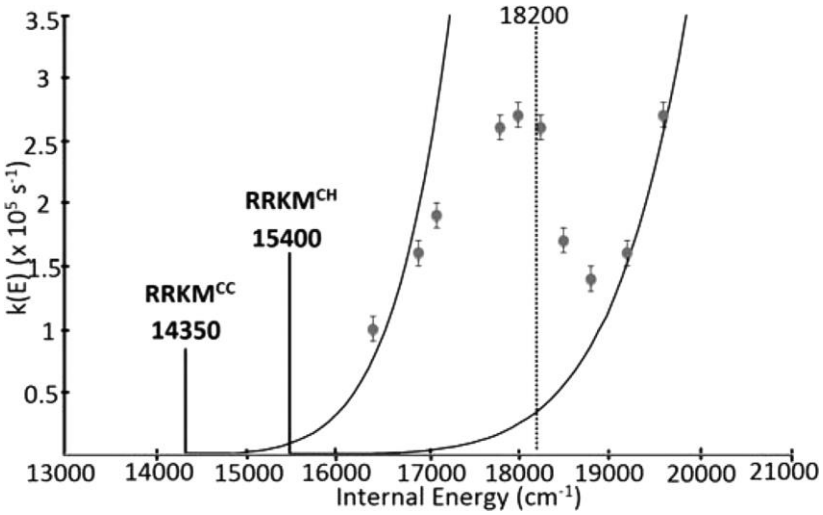

Figure 4.6 Plot of measure rate constants with respect to the laser energy used to initiate the Ni^+ mediated decarbonylation reaction of propionaldehyde.

The metal, σ-bond insertion transition states, TS1 and TS3, are the two kinetically important barriers separating reactants from products. The C-activation coordinate initiates with Ni^+ addition into a C-C bond followed by aldehyde C-H insertion, whereas the H-activation path is in the reverse sequence; aldehyde C-H followed by C-C insertion. A tri-coordinated Ni^+ complex (Int3) is formed at the merging point of the alternate pathways. Reductive elimination of ethane and Ni^+CO follows through the low-lying TS4 as the aldehyde hydrogen atom transfers onto the α-carbon.

Tunneling corrections applying the Wigner model were calculated to determine the role that hydrogen atom tunneling played in the decomposition dynamics.[75,76] These computations resulted in a decrease in the energy of the rate limiting TS3 by less than 10 cm^{-1}. This insignificant improvement indicates that tunneling contributes negligibly to the decomposition dynamics. This is expected since the rate limiting kinetic barrier is a second Ni^+ σ-bond insertion process with little chemical activity attributed to any hydrogen atom.

Discussion

Figure 4.6 shows that the measured k(E) values possess an unusual energy dependence. Ordinarily, the rate constant extracted from a single exponential fit is the rate limiting constant of the reaction, and assuming that the internal energy of the $Ni^+(C_3H_6O)$ cluster can be closely approximated by the absorbed photon energy, this should correspond to the microcanonical rate. As such, the microcanonical rate constant is expected to continuously increase with increasing internal energy in accord with the RRKM formalism. But despite the initial agreement with this trend from measurements at 16400, 16800, and 17100 cm^{-1}, there is a clear deviation from this behavior above

17100 cm^{-1} as the k(E) values reach a local maximum, drop suddenly, and then rapidly increase above 19100 cm^{-1}. In light of these considerations, we conclude that the measured rate constants do not correspond to a single microcanonical rate constant for the $Ni^{+}(C_3H_6O)$ decomposition and a more subtle interpretation is required to explain the observed behavior.

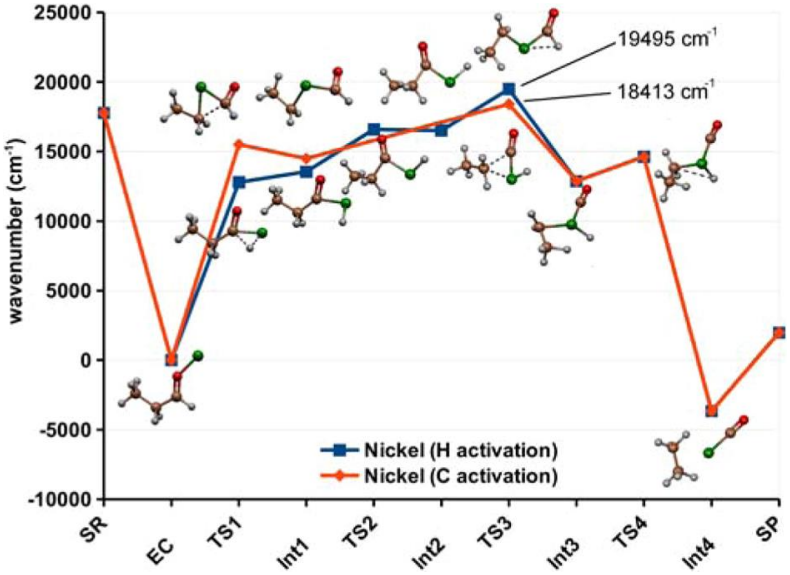

Figure 4.7 Potential energy surface (PES) for the Ni^{+} assisted dissociative reaction of propionaldehyde computed at the UCCSD(T)/def2-TZVP//PBEPBE/cc-pVDZ level of theory. Computed structures at critical locations along the PES are indicated. SR, EC, TS, INT, and SP are the separated reactants, encounter complex, transition states, intermediates and separated products.

At this point, we turn to the calculated potential energy surface of Figure 4.7 which shows two parallel pathways that result in the same decarbonylation product. This result is chemically intuitive in that both pathways begin with Ni^{+} insertion into either a C-C or C-H bond. Furthermore, this suggests that the unusual energy dependence observed in Figure 4.6 may somehow be a result of the interplay between these two competitive processes. This hypothesis is tested by reducing the PES of Figure 4.7 to a simple mechanism where each coordinate is described by an oxidative addition / reductive elimination two-step sequence as provided in scheme 1. Here, the odd

numbered rate constants, k_1 and k_3, connect the precursor to products through the coupled C-C/C-H insertion, deethanation (1-2-4) sequence, whereas rate constants k_2 and k_4 are for the consecutive C-H/C-C insertion, deethanation (1-3-4) sequence. Focusing only on the forward reactions permits exact integration of the corresponding differential rate equations to yield equations 4.1 - 4.4 which detail the temporal development of the EC, intermediates, and product,

$$EC_t = EC_0 e^{-k't} \tag{4.1}$$

$$Int1_t^{CC} = \frac{k_1 EC_0}{k_3 - k'}\left(e^{-k't} - e^{-k_3 t}\right) \tag{4.2}$$

$$Int1_t^{CH} = \frac{k_2 EC_0}{k_4 - k'}\left(e^{-k't} - e^{-k_4 t}\right) \tag{4.3}$$

$$Ni^{+}CO_t = EC_0 - EC_t - Int_t^{CC} - Int_t^{CH} \tag{4.4}$$

Equations 4.1 – 4.4 form the basis of a computer program to model product production convoluted by our instrument response providing a simulated contour for comparison to the measured waveforms of Figure 4.5. The program requires the input of five parameters to be optimized, EC_0 and k_1-k_4. However, this program is not meant to be quantitatively rigorous. Although neglecting the effects of back reactions permits exact integration of the differential equations, this renders the model incomplete and will not accurately describe all aspects of the decomposition. Indeed, reaction dynamics such as intermediate lifetimes are likely overestimated by this model. Nevertheless, the purpose of the model is to identify conditions, if any exist, that may provide rationale for

the unique energy dependence of the observed rate constants in Figure 4.6. Before beginning this search, we establish that each rate constant must increase when simulating subsequent waveforms acquired at higher energies. We further assume that the opening of a parallel coordinate can be modeled by setting one of the four rate constants to zero and then increasing its value in subsequent simulations of waveforms acquired at higher energies. We initiate the search to model the dynamic behavior observed in Figure 4.6 by very generally narrowing the acceptable parameter space. The possibility of a fully concerted reaction, one where reactants are directly converted into products sans any intermediate, is eliminated. This is done by generating four contour simulations to compare to the experimental SPIDRR waveforms (lowest two panels of Figure 4.8). The first two low energy acquisitions are simulated by setting k_1 to zero with subsequent increases in k_2. The third and fourth simulations are generated by increasing both rate constant values. The result is the lower panel in Figure 4.8 where the lower traces agree with experiment whereas the upper two do not. We find that there is no rate constant value that, when increased from zero, will simulate the measured waveforms. The fully concerted reactions are thus eliminated from the acceptable parameter space.

In a similar fashion, we test the condition where four rate constants model the dynamics (an oxidative addition / reductive elimination sequence along both coordinates), but where the magnitudes of k_1 and k_2 rate limit the reaction (k_1, $k_2 < k_3$, k_4). Here, either k_1 or k_2 is set to zero at low acquisition energies and then each rate constant is systematically increased to generate simulations that are tested against the higher energy measurements. Again, there are no rate constant combinations that show the observed decrease in the measured rate constant with increased precursor internal energy

(Figure 4.8). We therefore conclude that the early transition states cannot control the reaction kinetics.

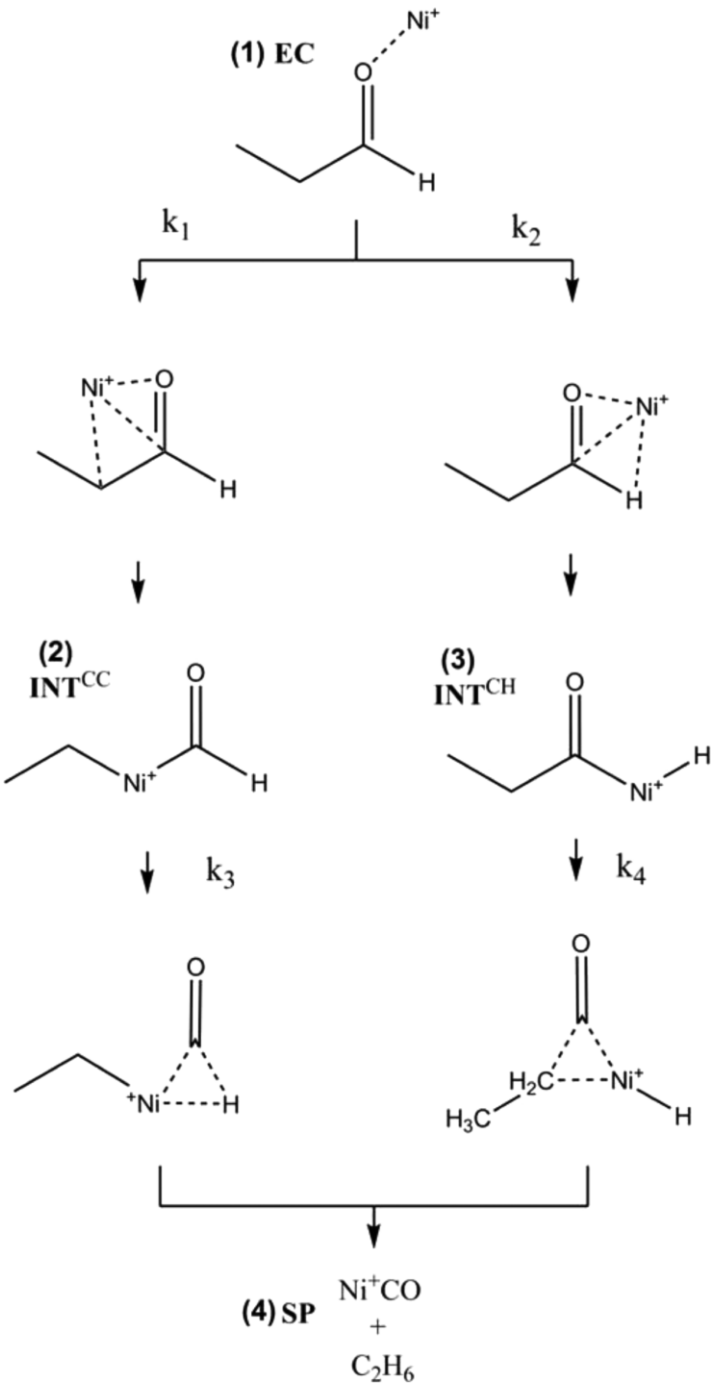

Scheme 1. EC_0 is the initial photo excited EC concentration and $k'=(k_1+k_2)$.

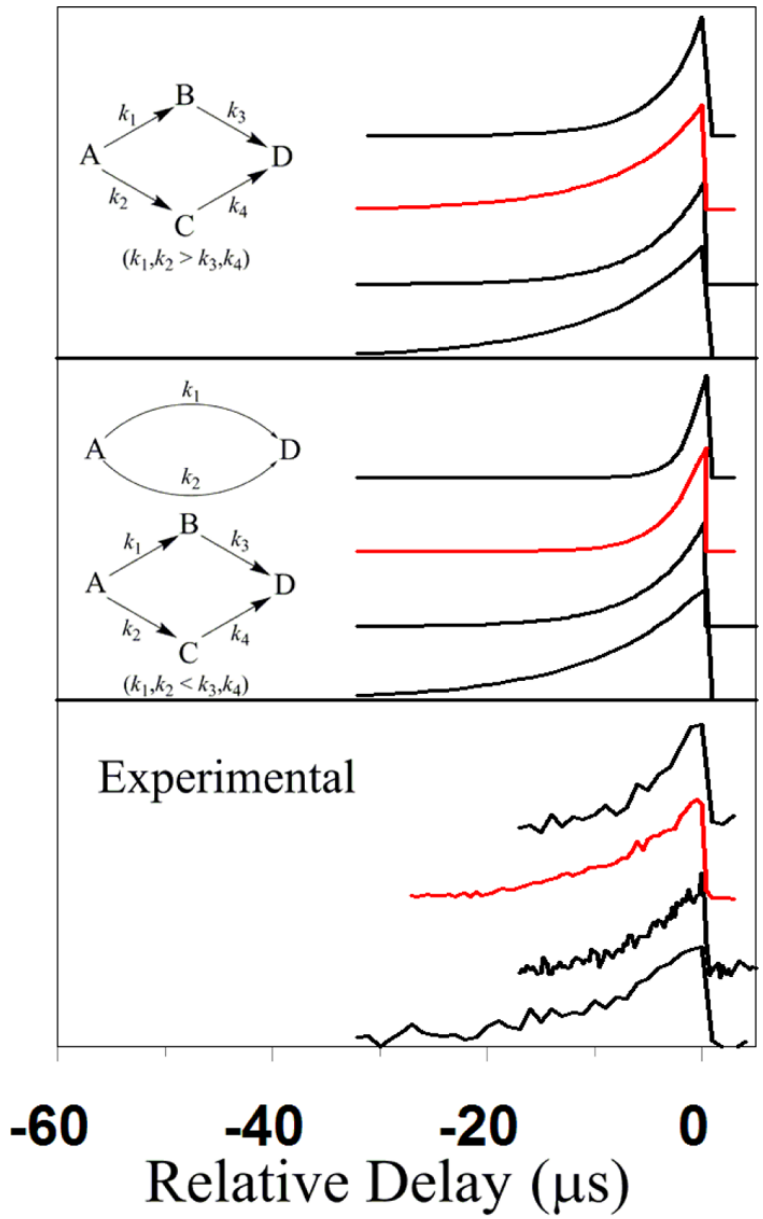

Figure 4.8 Simulations used to determine the parameters capable of reproducing the decrease in the observed rate constant as energy to the system is increased. The bottom panel is another rendering of the waveforms of Figure 4.5. The four traces in upper panels simulate product formation. The red trace is the result of increasing one of the rate constants from zero value.

We test one final condition where the reaction is again described by an oxidative addition / reductive elimination sequence along both coordinates, however, here the magnitudes of the rate constants are such that the steps leading to elimination rate limit product production (k_1, $k_2 > k_3$, k_4). Here, either k_3 or k_4 is set to zero at low acquisition energies while the remaining rate constants are optimized to simulate the measured waveform. Each rate constant is systematically increased to simulate the waveforms acquired at higher energies. Under this circumstance, there is qualitative agreement with observation (top panel, Figure 4.8). We thus conclude that the only condition where such a phenomena as suggested by Figure 4.6 may occur for the Ni^+ mediated decomposition of propionaldehyde is if there are competitive parallel dissociative reaction coordinates rate limited by reductive elimination.

Scheme 1 associates k_1-k_4 as the rate constants to surmount the specific kinetic barriers attributed to the 1-2, 1-3, 2-4, and 3-4 legs of the parallel reaction coordinates. The corresponding transition states from the PES of Figure 4.7 are $TS1^{CC}$, $TS1^{CH}$, $TS3^{CC}$, and $TS3^{CH}$. If we assume the usual inverse relationship between rate constant and barrier height (a fair assumption considering that each of these tight transition states requires significant rearrangement of the reactants to form the corresponding activated complexes) then the relative rate constant ordering is directly comparable to the transition state ordering. The simulations of Figure 4.8 indicate that it is the formation of late transition states on each coordinate that rate limit product production and these, therefore, should represent the most energetic demanding features on the PES. This is in agreement with the computations of Figure 4.7 where the TS3 energy > TS1 along both coordinates.

The simulation derived from equations 4.1-4.4 is incapable of unambiguously assigning the relative magnitudes of k_3 and k_4, and thus the corresponding relative energetic ordering of $TS3^{CC}$ and $TS3^{CH}$ as well. To ascertain this ordering, we turn to a similar study where the SPIDRR technique was used to study the Ni^+ mediated decomposition of acetaldehyde. In that study there were also two parallel competitive reaction coordinates leading to the decarbonylation of the precursor. However, the acetaldehyde results were not ambiguous and the most energetic demanding path was the one that initiated with C-H bond activation. The similarity in the two studies suggests that the higher energy path in this titular study also lies along the C-H activation coordinate and is in agreement with the PES of Figure 4.7.

The qualitative agreement observed between experiment and DFT allows us to confidently use the results of computation to pursue a more complete description of the reaction dynamics. The vibrational frequencies for the EC and each rate limiting TS were calculated at the PBEPBE/cc-pVDZ level and used as input parameters to calculate the sum and density of states to determine the RRKM microcanonical rate constant. The RRKM rate constants calculated from the $TS3^{CC}$ transition state vibrational frequencies and a critical energy equal to 14350 cm^{-1} provides the best overlap with the observed rate constants measured at internal energies less than 17100 cm^{-1} (Figure 4.6). There is however, clear deviation from this curve (labeled $RRKM^{CC}$) at all observed rate constants measured at energies greater than 17100 cm^{-1}. Extrapolation of the $RRKM^{CC}$ curve to k = 1 x 10^6 s^{-1} occurs at an energy = 18200 cm^{-1}. Recall that the SPIDRR technique is incapable of sampling fragments from decomposition reactions with rate constants this large. Thus, a k(E=18200 cm^{-1}) = 1 x 10^6 s^{-1} represents an upper limit to our sampling

ability and this E=18200 cm^{-1} is inscribed as a vertical dashed line in Figure 4.6. It is not happenstance that the measured rate constants decrease dramatically at energies ~ 18200 cm^{-1}. In fact, these results suggest that both propionaldehyde decarbonylation reaction coordinates are open at energies less than 18200 cm^{-1} but the fast component masks the slower at these energies. At energies in excess of this limit, the fast component can no longer be sampled and the slower becomes observable. This further suggests that the rate constants measured at energies much greater than the 18200 cm^{-1} limit are likely free from products produced via the lower energy pathway. Therefore another RRKM analysis was conducted however using the computed vibrational frequencies of $TS3^{CH}$ as input. The best overlap between the highest energy observed rate constants occurs when the $RRKM^{CH}$ curve is calculated with a critical energy = 15400 cm^{-1} (Figure 4.6). The difference in critical energies between $RRKM^{CC}$ and $RRKM^{CH}$ is 1050 cm^{-1} which is in remarkable agreement with the energetic difference between computed the transition states $TS3^{CC}$ and $TS3^{CH}$, 1082 cm^{-1} (Figure 4.7).

Figure 4.6 indicates that both slow and fast processes occur at most of the sampled energies and thus, the observed rate constants contain contributions from the decarbonylation along each coordinate. This contribution from each microcanonical rate constant to the measured rate constant is approximated by extrapolation of the RRKM curves in Figure 4.6. We now return to the waveform simulator and use the RRKM predicted rate constants for k_3 and k_4 as initial input parameters. The remaining two rate constants, k_1 and k_2, as well as A_0 are varied to optimize overlap between the simulated contour and the measured waveform. If needed, the k_3 and k_4 rate constants are slightly modified to optimize overlap. As before, the rate constants are required to increase when

simulating subsequent waveforms acquired at higher energies. These results are shown in Figure 4.7.

Panel B of Figure 4.9 shows the waveform acquired at energy = 17100 cm^{-1} with $k_{obs} = 1.9 \times 10^5\ s^{-1}$ (Table 1). RRKM predicts that the microcanonical rate constants $k_3 = 2.5 \times 10^5\ s^{-1}$ and $k_4 = 0.03 \times 10^5\ s^{-1}$ contribute to the decarbonylation reaction at this energy. These two rate constants are input into the simulator and we find acceptable agreement with measurement when the ratio of $k_1/k_2 = 3.5$, however, the absolute values of k_1 and k_2 cannot be specified with any certainty. The temporal dependence of the precursor, each intermediate, and final product are shown beneath the simulated contour. Under the conditions specified, product production nearly exclusively follows the decay of INT^{CC}. Panel C of Figure 4.9 shows the waveform acquired at a cluster internal energy = 18800 cm^{-1}. The k_4 rate constant had to be increased to $1.25 \times 10^5\ s^{-1}$ from the RRKM predicted value ($0.86 \times 10^5\ s^{-1}$) to optimize overlap between the simulated contour and the measured waveform. Additionally, k_1 and k_2 rate constants have increased but their ratio was decreased to 1.75. RRKM predicts that k_3 has increased to $32.8 \times 10^5\ s^{-1}$ at this energy and the resulting decay of INT^{CH} only contributes to product production at very early times. The traces under the contour suggest that the decarbonylation of propionaldehyde is governed by the decay of INT^{CH} at a cluster internal energy = 18800 cm^{-1}. Further increases in internal energy (panel D, Figure 4.9) follow suit with the product yields controlled by the decay of INT^{CH} with negligible contributions from INT^{CC} decay.

Conclusions

The simulations of Figure 4.9 suggest a scenario to describe the rather unique energy dependent rate constant behavior observed in Figure 4.6. The dissociative reaction must occur along parallel reaction coordinates rate-limited by the formation of late transition states. The rate constants to surmount these kinetic barriers are approximately the one provided in the legend of Figure 4.9. Furthermore, the simulations suggest that the early transition states control the reaction dynamics, that is, the k_1/k_2 ratio determines the probability of parallel path followed. However, this analysis is insufficient to unambiguously assign values to either of these rate constants or their ratio.

The RRKM analysis suggests that these late transition states are separated by 1050 cm^{-1} and this difference agrees with the difference in theoretical computed transition state energies, 1082 cm^{-1}. However, theory overestimates the barriers by ~4080 cm^{-1}. Despite the absolute difference observed between measurement and calculation, the relative agreement is promising and we believe the atomistic picture provided by theory is likely quite accurate. From Figure 4.7, the Ni^+ cation is localized on the carbonyl oxygen of the encounter complex. The first transition state along both coordinates has the Ni^+ activate either the aldehyde C-H or the C-C bond of propionaldehyde. The highest energy transition state along both coordinates is a second addition to another σ-bond by either Ni^+ or NiH^+ cations. Thus each parallel component of the dissociative reaction is best described as consecutive σ-bond insertions where the second controls the reaction kinetics and the first influencing the reaction dynamics.

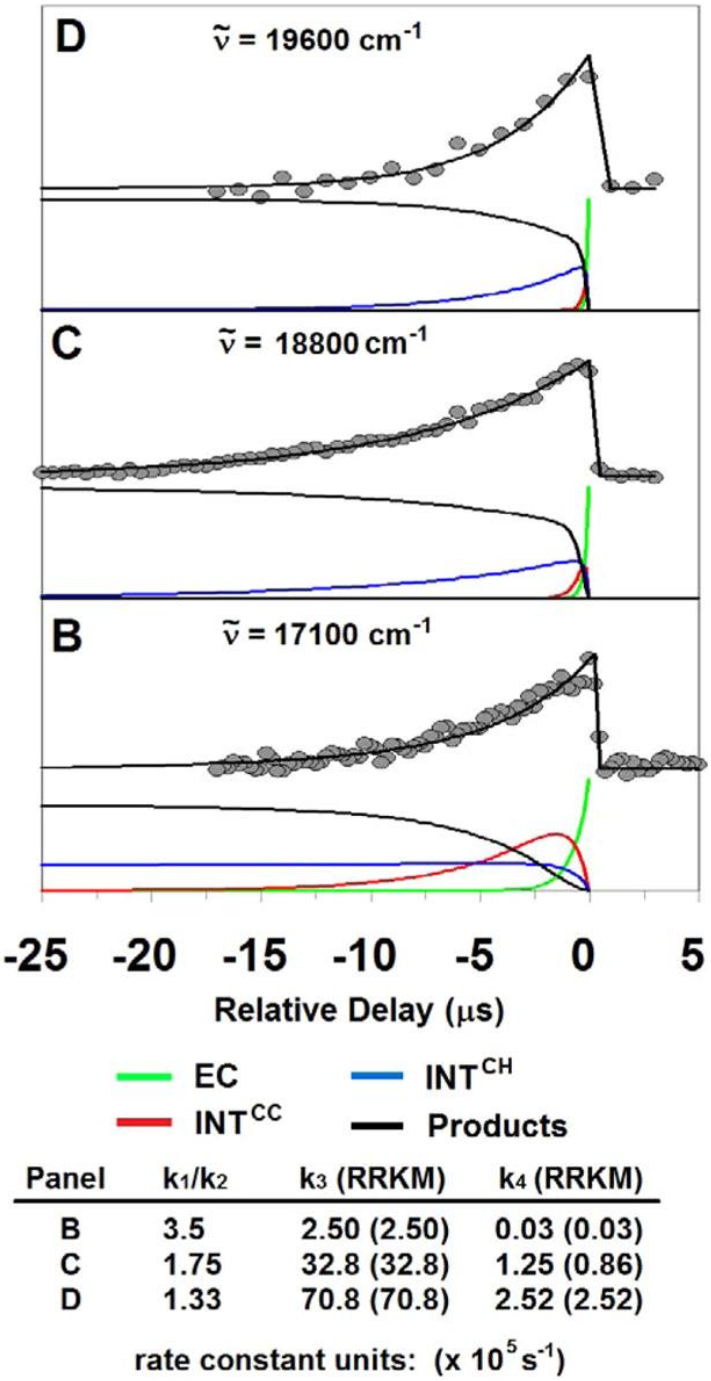

Panel	k_1/k_2	k_3 (RRKM)	k_4 (RRKM)
B	3.5	2.50 (2.50)	0.03 (0.03)
C	1.75	32.8 (32.8)	1.25 (0.86)
D	1.33	70.8 (70.8)	2.52 (2.52)

rate constant units: (x 10^5 s^{-1})

Figure 4.9 Temporal dependence of the encounter complex, intermediates, and product formation during the Ni^+ mediated decarbonylation reaction. The legend indicates the rate constants used to simulate the dependence and generate the simulated contour. Predictions from RRKM are in parentheses. Letter designations are consistent with Figure 4.4.

CHAPTER FIVE

Preliminary Results for the Dissociation of Ni^+Acetic Acid

Introduction

Protodecarboxylation and dehydration of carboxylic acids are utilized widely in nature and chemistry laboratories of all kinds. Metal catalysts are often required for these reactions both to reduce the required temperature to a reasonable value as well as to increase the selectivity of the reaction. For example, acetic acid pyrolysis, which occurs at temperatures > 500^0 C, results in both dehydration (rxn. 3.1) as well as decarboxylation (rxn. 3.2) at a 2:1 ratio.[77,78]

$$H_3COOH \rightarrow H_2O + CH_2CO \qquad \text{Reaction 5.1}$$

$$H_3COOH \rightarrow CH_4 + CO_2 \qquad \text{Reaction 5.2}$$

In the presence of copper catalysts, the required temperature drops to 260^0 C, and the ratio shifts to favor decarboxylation almost exclusively.[79] Similarly, in experiments between acetic acid and M^+Phenanthroline (where M is Nickel, Palladium and Platinum), Matthew Woolley and coworkers observed only CO_2 and CH_4 production.[80] Decomposition of acetic acid over a platinum catalyst results in both CO and CO_2 formation. However, over a graphitized platinum surface, the reaction results exclusively in ketene and water.[81]

The carboxylation of methane to form acetic acid is a promising method of CO_2 sequestration which results in an industrially useful product. Furthermore, the process converts methane to a more easily transportable liquid, while being 100% atom efficient.

However, a catalyst which can make this reaction practical has not yet been found.[82] Its elusiveness comes from the fact that the catalyst would need to activate both the methane and the CO_2, and while there are transition metals which activate one or the other, there does not seem to be much overlap between the two groups.

Given that such small changes to the catalyst surface can result in the drastic chemical changes mentioned above (which essentially arise from a competition between C-O, C-C, O-H and C-H activation), a fundamental understanding of how transition metals change the potential energy landscape of reactions will make finding the most appropriate catalyst for a particular purpose a more streamlined process, based on easily measured or calculated properties. Accordingly, a significant amount of condensed phase, molecular ion beam, and theoretical studies have been done to elucidate the details of these reactions.[80-85] Our group's ability to make energy resolved kinetic measurements will further this global effort by providing details of the region of the reaction coordinate submerged with respect to separated reactants, as well as providing experimental values which can be used to assess computational results.

This chapter presents the data which has been gathered by our group up to the point of writing and discusses its analysis and provides current thoughts concerning the mechanism and potential energy surface. This study provides the first opportunity for our group to study reactions involving C-O activation which in this case is in competition with both C-C and C-H activation. The activation steps likely proceed from two different encounter complexes, which are separated by a shallow barrier, and have different zero point energies. This means that the comparison between the two rate constants is not just

a comparison of the different activation energies, but also incorporates the different densities of states and zero point energies, according to RRKM (eqn. 3.1).[18,19,91]

$$k(E) = \frac{\sigma N^{\ddagger}(E - E_0)}{\rho(E)} \tag{3.1}$$

Where k(E) is the energy dependent microcanonical rate constant, E is the internal energy of the system, σ is the reaction symmetry, $N^{\ddagger}(E\text{-}E_0)$ is the sum of states of the transition state, E_0 is the activation energy for the reaction and ρ(E) is the density of states of the reactant. Competitive reactions, by definition, share a common reactant, which corresponds to a shared denominator in equation 3.1. Therefore, a comparison of competitive steps is essentially a comparison of the sums of states of the transition states. Similarly, forward and back reactions share a common transition state so that a comparison between a forward and back reaction is a comparison between the densities of states of the reactants. By breaking the rate constants into these two parameters, which are shared by multiple steps, the overall number of parameters is reduced and the modeled rate constants can be constrained to behave in a manner predicted by RRKM.

Identification of Products

The products of the decomposition of Ni^+Acetic Acid and $Ni^+(d_3)$Acetic Acid were identified using the kinetic energy filter described in chapter 2. In Figures 5.1 and 5.2, the x-axis is the ratio of the potential difference between the halves of the sector to the parent sector, which is the same as the ratio of the product masses to the parent mass. Both sector scans have three peaks. The peaks in Figure 5.1 are centered at 0.64, 0.76 and 0.85. These values correspond to masses of 76, 90 and 100 amu. The peaks in Figure 5.2 are centered at 0.64, 0.77 and 0.84, which correspond to masses of 77, 93 and

102. The change in mass from 90 to 93 indicates that this product contains all three methyl hydrogen/ deuterium atoms. Similarly, the mass change in the other products indicates that the lightest and heaviest product channels contain one and two of the originally methyl hydrogens respectively. Therefore, the products of Ni^+Acetic Acid decomposition are $Ni^+H_2O + C_2H_2O$, $Ni^+CH_4O + CO$ and $Ni^+C_2H_2O + H_2O$, as shown in reactions 5.1 through 5.3 in scheme 5.1.

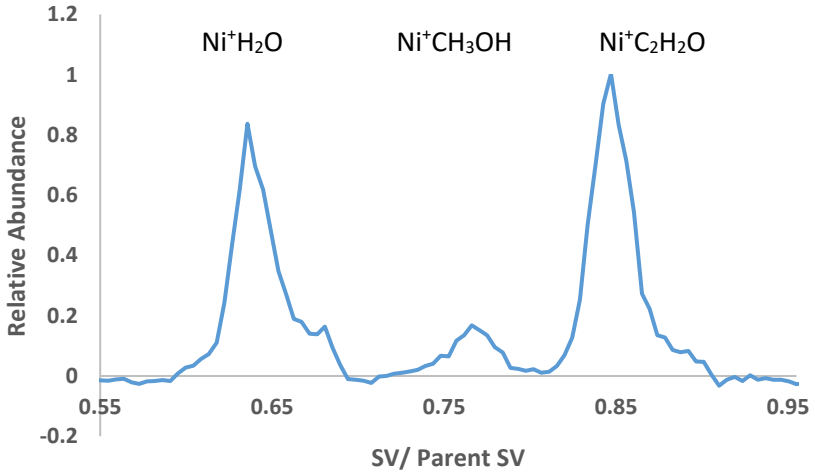

Figure 5.1 Sector Scan of Ni^+Acetic Acid → Products

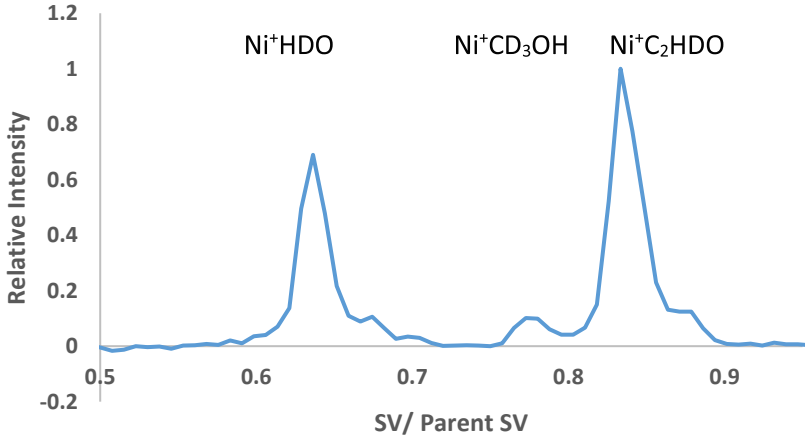

Figure 5.2 Sector Scan of $Ni^+(d_3)$Acetic Acid → Products

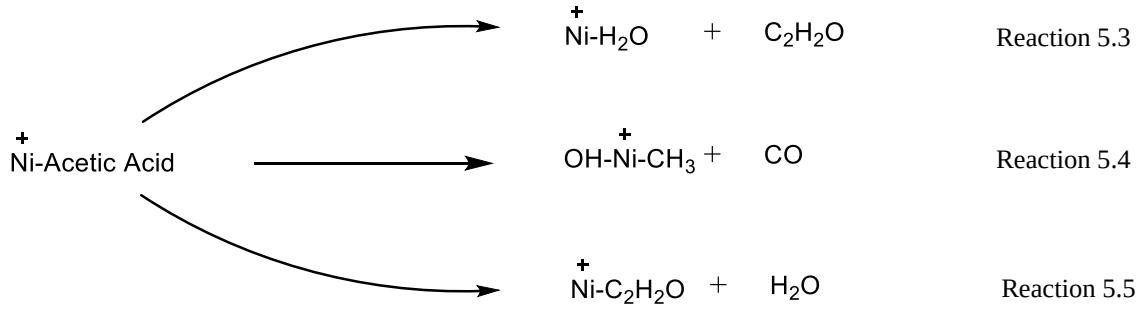

Scheme 5.1

The similarities between reactions 5.3 and 5.5 indicates that they both come from the same electrostatic intermediate (Reactions 5.6 and 5.7), specifically, ketene and water electrostatically bound to the nickel cation. Reaction 5.2 does not seem to have a counterpart resulting in the CO remaining electrostatically bound to the nickel cation, which suggests that the CO may dissociate from the complex while the other non-metal atoms are in a conformation that would be unstable without the metal cation (reaction 5.8).

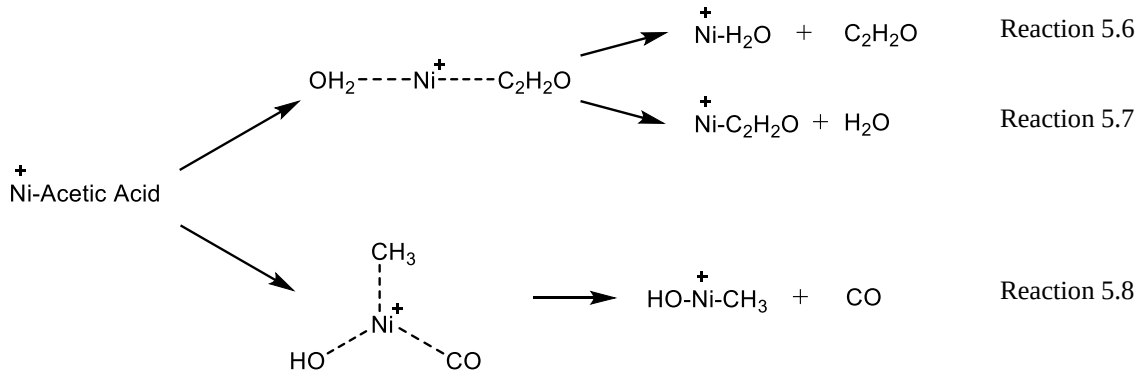

Scheme 5.2

The electrostatic intermediate shared by reactions 5.6 and 5.7 requires activation of both the C-O bond and a C-H bond by the nickel cation. The intermediate involved in reaction 5.8 is formed from activation of both the C-C bond and the C-OH bond.

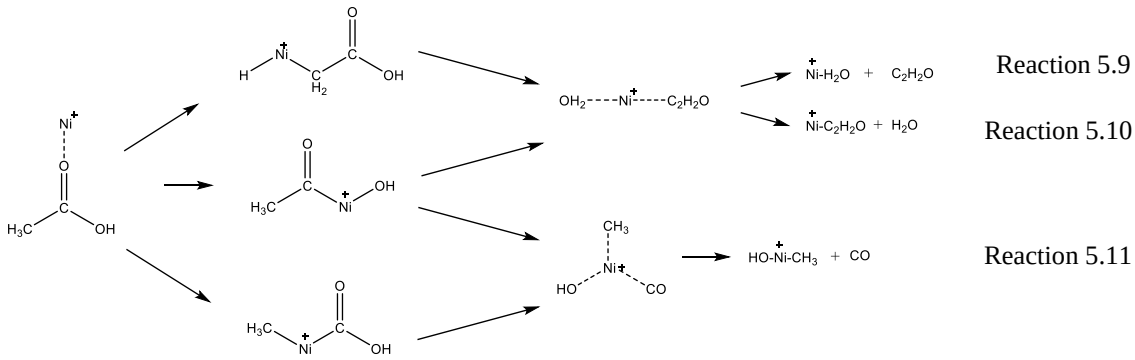

Scheme 5.3

Finally, there are two possible conformations for the initial Ni^{+}Acetic Acid complex, since the nickel cation can interact with either dipole on the acetic acid, leading to the mechanism presented in scheme 5.4. The presence of each product indicates that C-H activation cannot be preferable to both C-C and C-O activation to the point that it dominates the reaction.

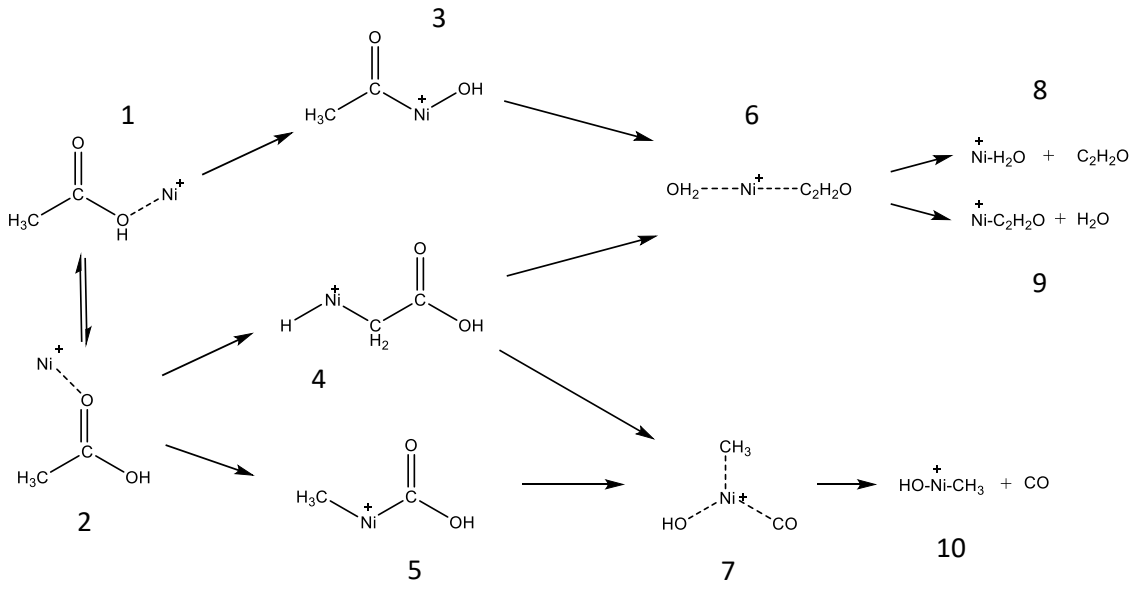

Scheme 5.4

Kinetic Scans: Decomposition of Ni^+Acetic Acid

The temporal dependence of the formation of $Ni^+C_2H_2O$ and Ni^+H_2O from Ni^+Acetic Acid at various internal energies is shown in Figures 5.3a-q. A single exponential curve is fit to each data set.

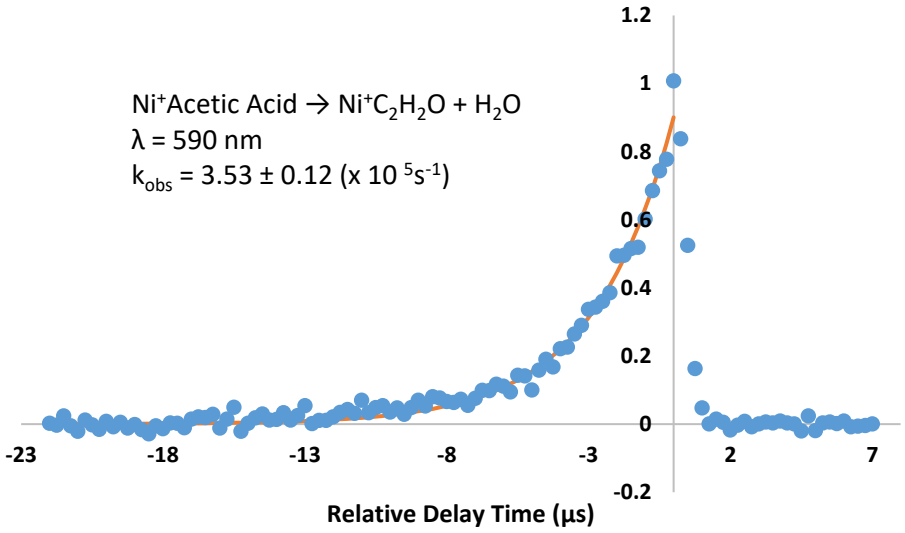

Figure 5.3a

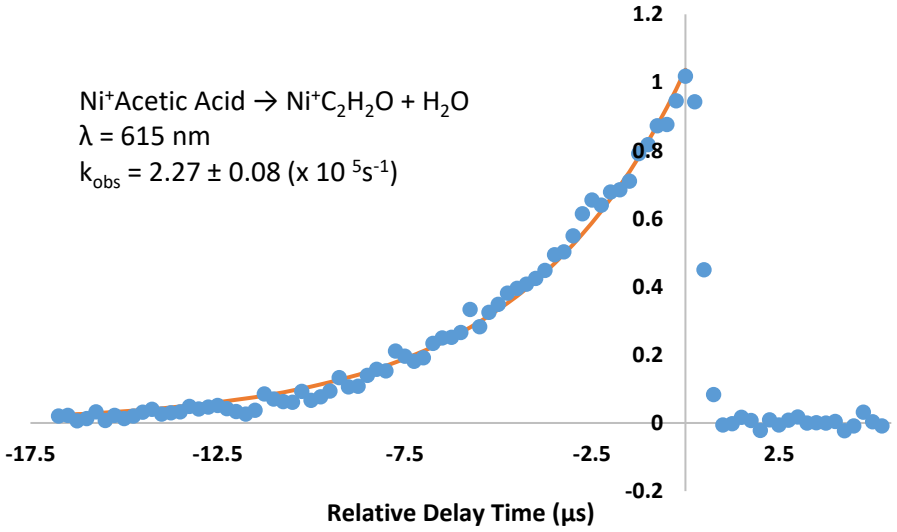

Figure 5.3b

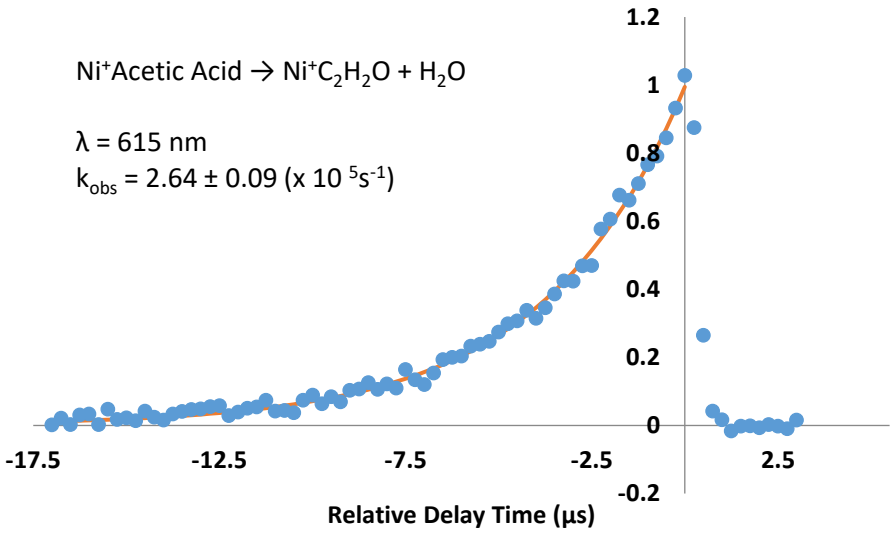

Figure 5.3c

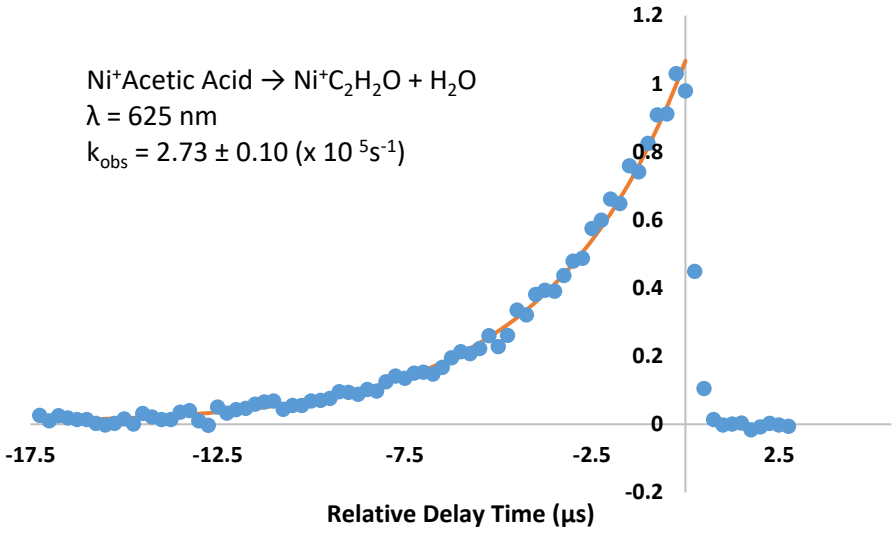

Figure 5.3d

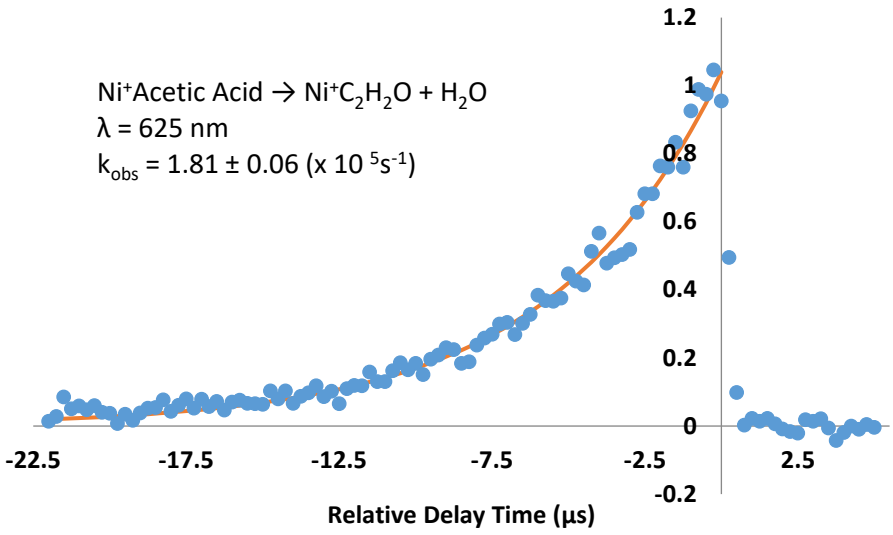

Figure 5.3e

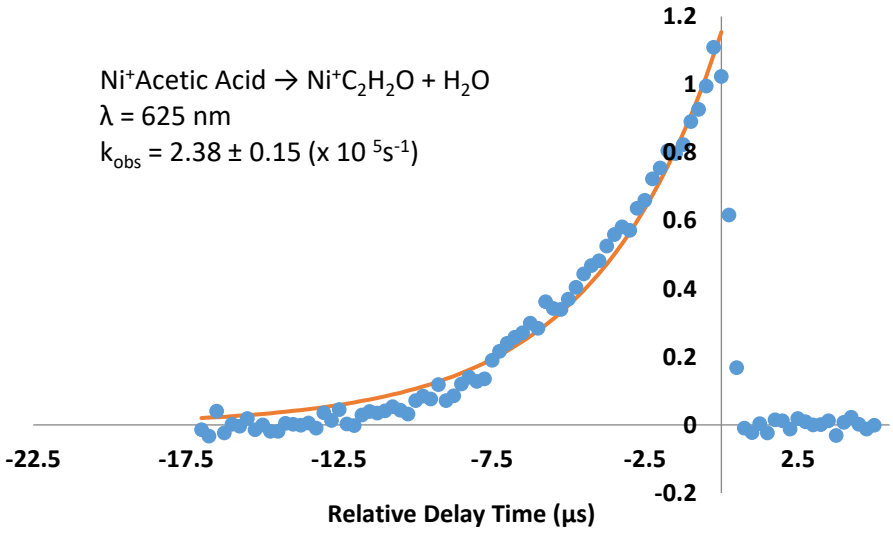

Figure 5.3f

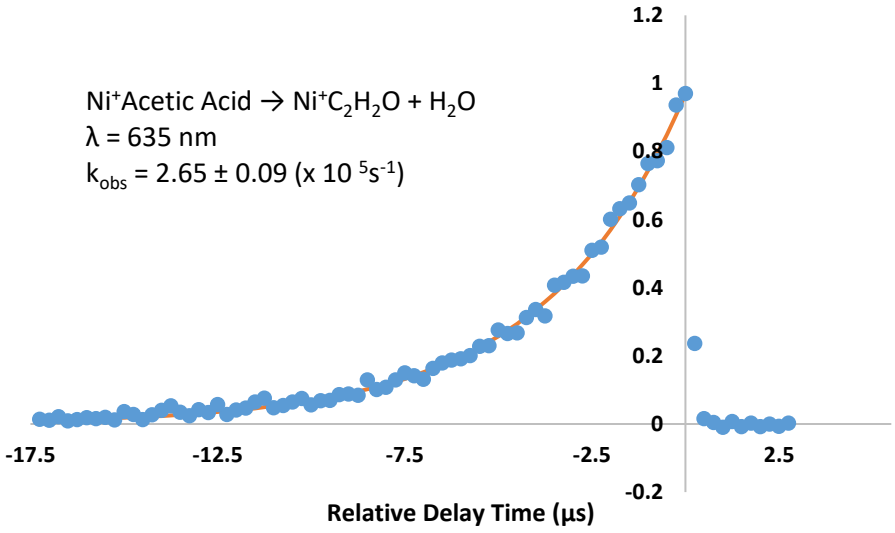

Figure 5.3g

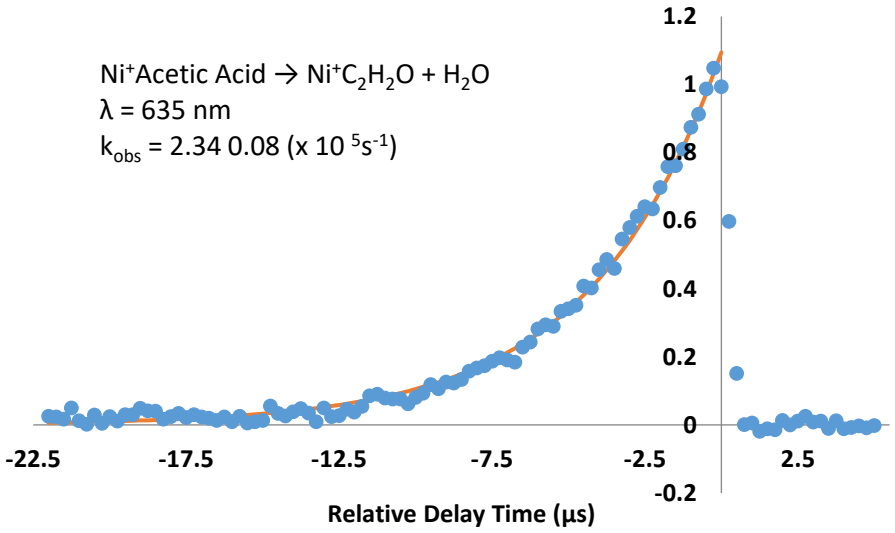

Figure 5.3h

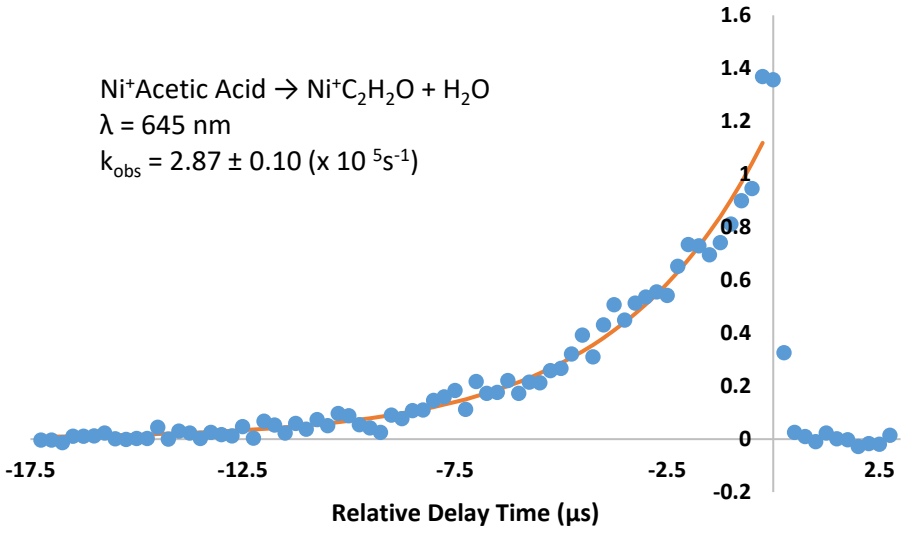

Figure 5.3i

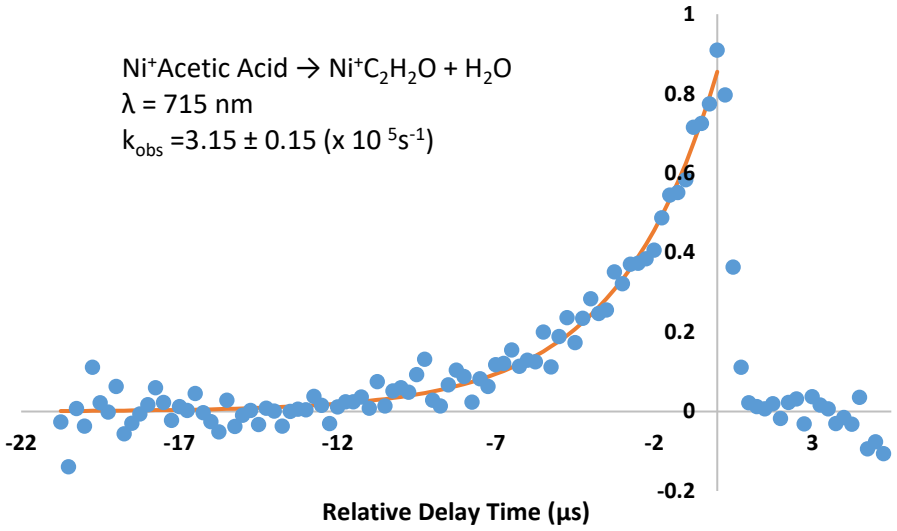

Figure 5.3j

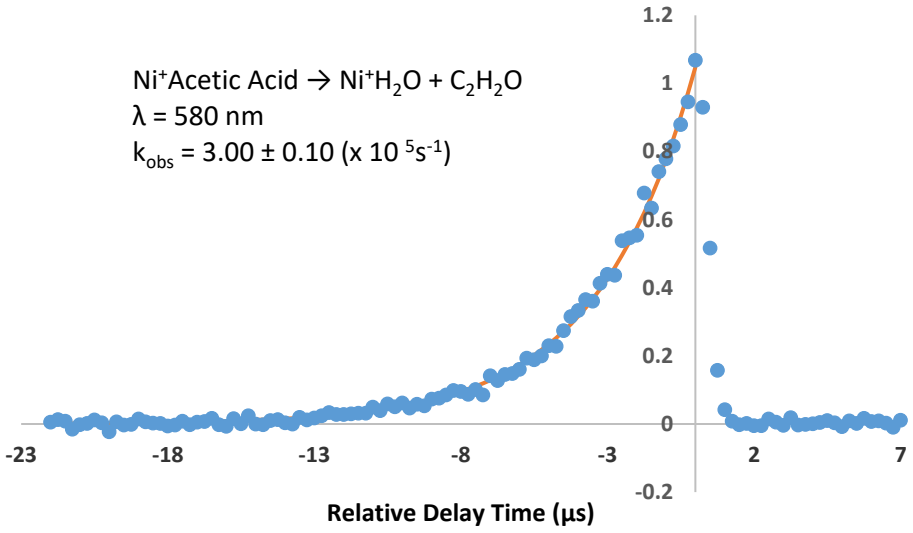

Figure 5.3k

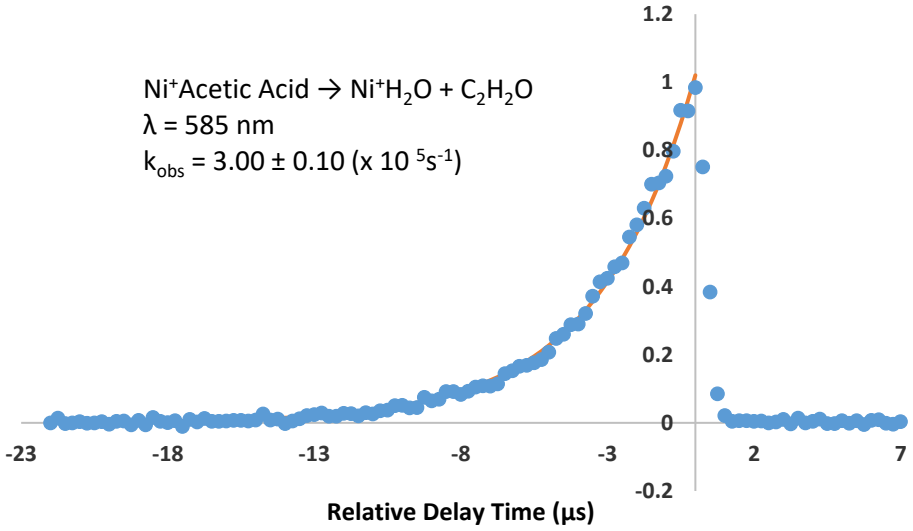

Figure 5.3l

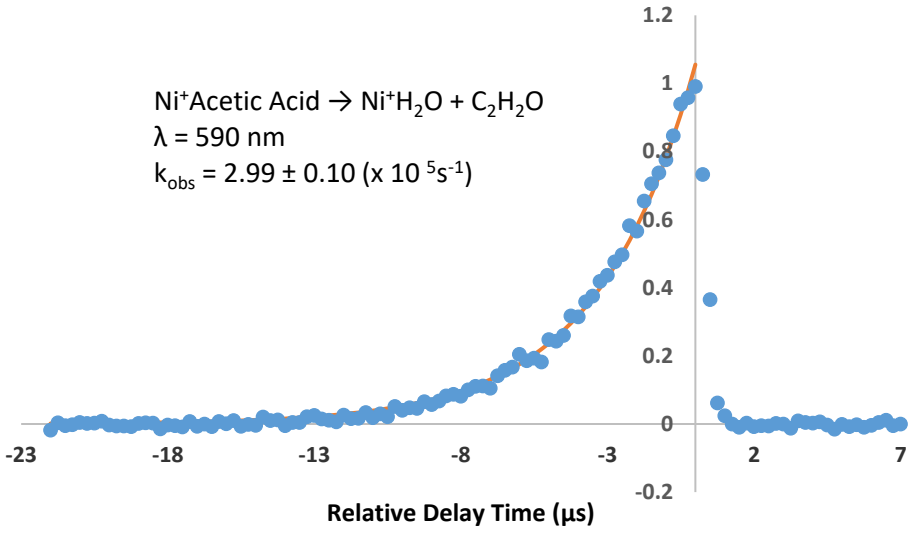

Figure 5.3m

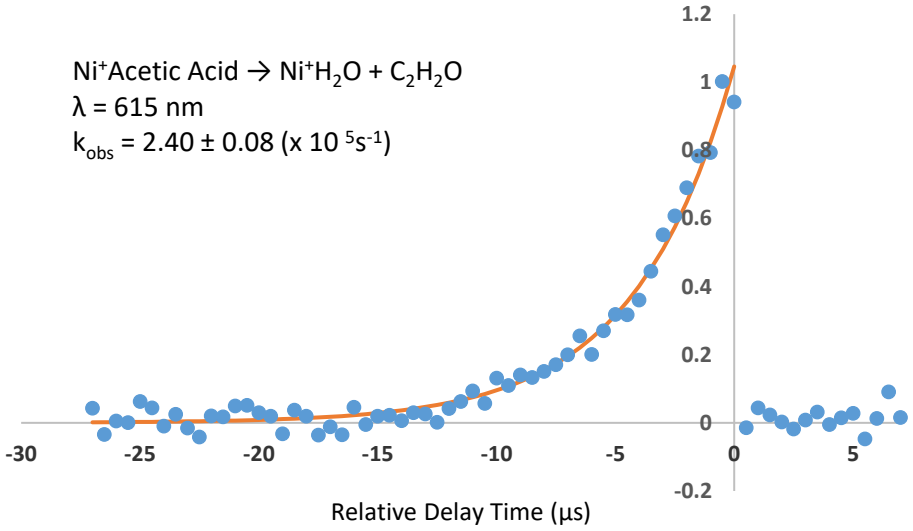

Figure 5.3n

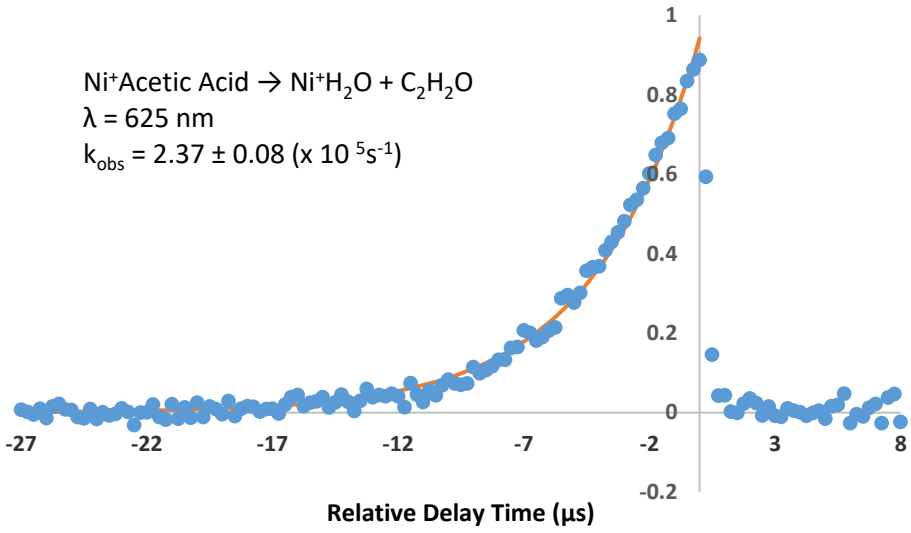

Figure 5.3o

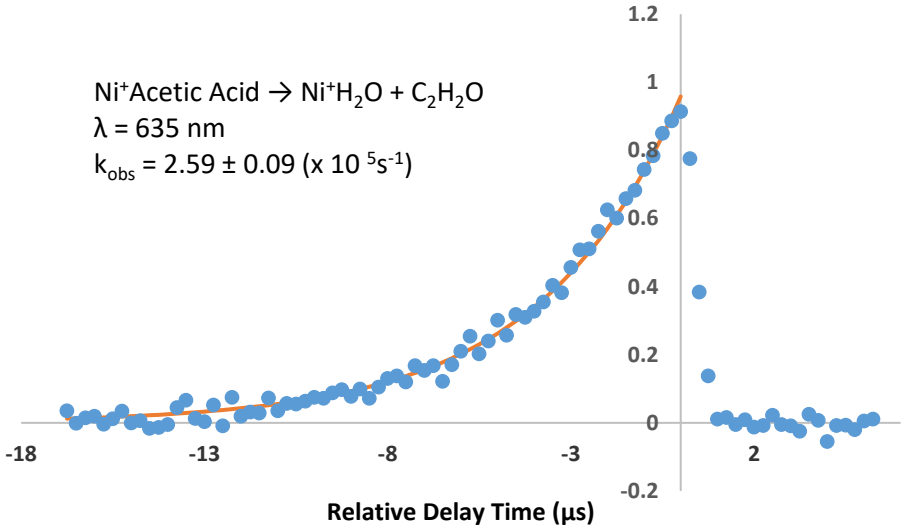

Figure 5.3p

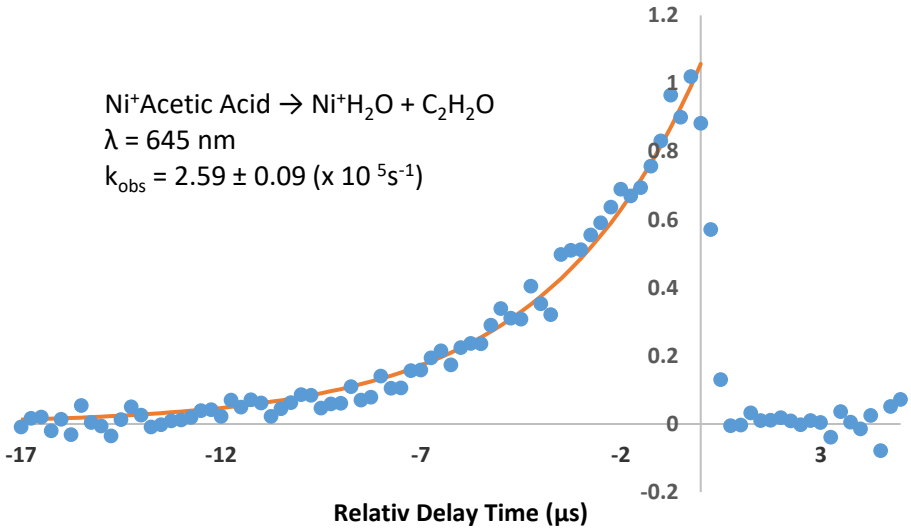

Figure 5.3q

Figures 5.3a-q show scans of $Ni^+C_2H_2O$ and Ni^+H_2O product intensities as a function of laser timing delay. Each plot is fit to a single exponential ($\boldsymbol{Ae^{-kt}}$) and the measured rate constant provided in each Figure.

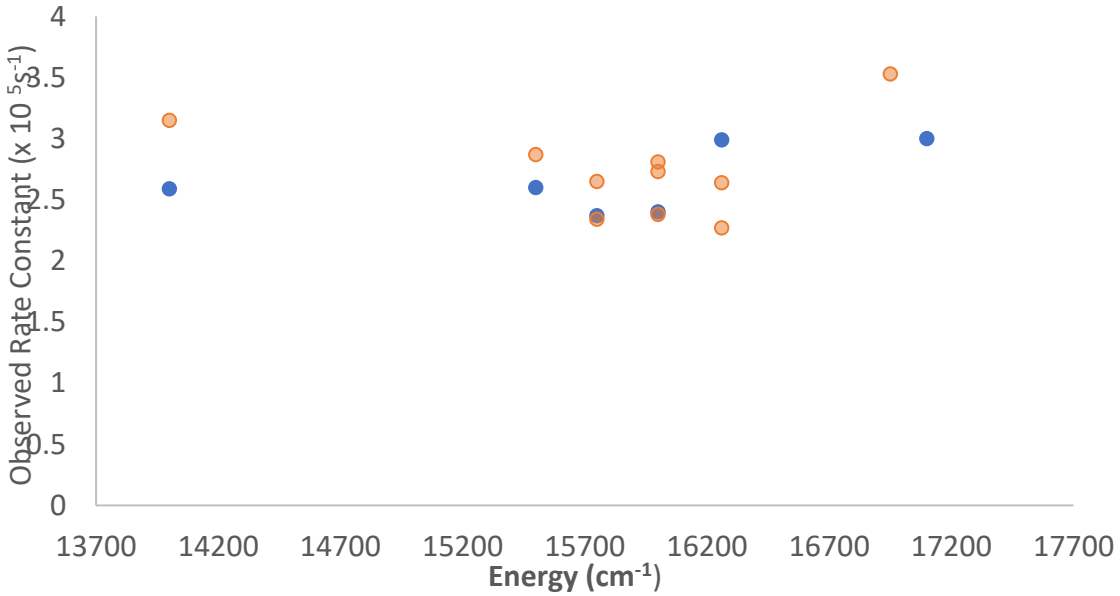

Figure 5.4 The observed rate constant for each data set vs. internal energy for Ni^+Acetic Acid → $Ni^+C_2H_2O$ + H_2O (orange) and Ni^+Acetic Acid → Ni^+H_2O + C_2H_2O (Blue).

Table 5.1 The observed rate constant for each data set at each energy for the decomposition of Ni^+Acetic Acid into $Ni^+C_2H_2O$ and Ni^+H_2O.

	observed rate constant ($x10^5 s^{-1}$)	
Energy (cm^{-1})	Ni^+H_2O	$Ni^+C_2H_2O$
17100	3.00	
16950		3.53
16260	2.99	2.27
16260		2.64
16000	2.40	2.73
16000		2.81
16000		2.38
15750	2.37	2.65
15750		2.34
15500	2.60	2.87
14000	2.59	3.15

The $Ni^+(h_4$-)Acetic Acid decomposition is well described by a single exponential at each photon energy, but the entire data set has two unexpected results. *(1)* The rate constants from multiple scans at the same internal energy vary. This variance is well outside the noise of each scan and on the same scale as those observed at different internal energies. *(2)* The observed rate constants do not increase with energy in a predictable manner. Instead, there seems to be little energetic dependence on the overall rate of decay (Figure 5.4). Clearly, a model using a single limiting rate constant is inadequate to describe these observations for this system over this energy range.

Both of these unexpected observations can be explained by assuming that multiple isomers along the reaction coordinate are populated during supersonic expansion. If decomposition from one species is measurably slower than the other, but both are relatively similar, then the observed temporal dependence will be a combination of both of these profiles. Figure 5.5 shows a qualitative potential energy surface which demonstrates this concept.

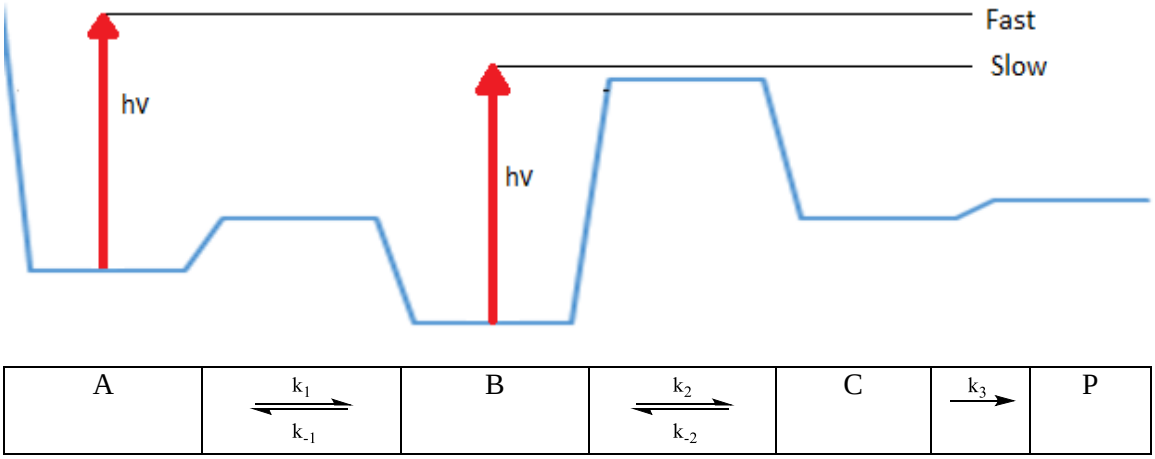

Figure 5.5 A model reaction coordinate in which two wells are initially populated. Excitation with a photon promotes both species with the same amount of energy (symbolized by the red line). In the energy region where this amount results in similar rates of product formation, the observed overall rate of reaction would be a combination of both profiles.

Figure 5.5 presents the simplest form of this model, where A → P and B → P each have only one kinetically important step. The difference in the rates of these reactions is primarily governed by the difference in the zero point energy of A and B.

Because the reactions begin as complexes with two distinct energies, there are two sets of rate equations, which are distinguished with a subscript A or B to indicate the starting complex. These are:

$$\frac{dA_A}{dt} = -k_{1A}A_A(t) + k_{-1A}B_A(t) \tag{5.1}$$

$$\frac{dB_A}{dt} = -(k_{-1A} + k_{2A})B_A(t) + k_{1A}A_A(t) + k_{-2A}C_A(t) \tag{5.2}$$

$$\frac{dC_A}{dt} = -(k_{-2A} + k_{3A})C_A(t) + k_{2A}B_A(t) \tag{5.3}$$

$$\frac{dA_B}{dt} = -k_{1B}A_B(t) + k_{-1B}B_B(t) \tag{5.4}$$

$$\frac{dB_B}{dt} = -(k_{-1B} + k_{2B})B_B(t) + k_{1B}A_B(t) + k_{-2B}C_B(t) \tag{5.5}$$

$$\frac{dC_B}{dt} = -(k_{-2B} + k_{3B})C_B(t) + k_{2B}B_B(t) \tag{5.6}$$

$$\frac{dP}{dt} = k_{3A}C_A(t) + k_{3B}C_B(t) \tag{5.7}$$

The assumption that the unexpected kinetic behavior can be explained by two initially populated wells in the reaction coordinate can be verified if a set of rate constants which increase with energy can be used to globally model the results presented in Figures 5.3a-q. Furthermore, the extent to which that set of rate constants is unique in its ability to reproduce the data determines the useful information about the potential energy surface that can be extracted from this particular result.

The ideal approach to determine the values of each rate constant using this model would begin with solving the above set of equations, but inclusion of back reactions makes this task impractical. However, since P(t) can be determined numerically, it was possible to optimize the rate constant values to yield waveforms that overlap the data in Figures 5.3a-j. These rate constants were made to increase with energy in a manner predicted by RRKM, by calculating each rate constant as a ratio of two separate functions of energy, $f(E\text{-}E_0)$ and $g(E)$, which are conceptually related to the sum and density of states in equation 3.1, respectively.

$$k(\mathrm{E}) = \frac{f(E - E_0)}{g(E)} \tag{5.8}$$

$$f(E - E_0) = \begin{cases} 0, & E < E_0 \\ (E - E_0)^n, & E \geq E_0 \end{cases} \tag{5.9}$$

$$g(E) = E^m \tag{5.10}$$

Where E is the energy available to the system relative to the zero point energy of A in Figure 5.5, E_0 is the activation barrier, also relative to the zero point energy of A, and m and n are dimensionless values chosen to guarantee that $f''(E\text{-}E_0) > g''(E) > 0$ and $k''(E) > 0$ at all energies. Also, the two sets of rate constants are required to increase in the same manner (i.e. k_{1A} and k_{1B} are two points on the same k(E) curve). If the energy

levels of the model PES minimize to values qualitatively similar to those presented in Figure 5.5, (A and B are separated by a small barrier, and the barrier between B and C is the only major influence on overall kinetic behavior), then product formation along the 1 → 2 → 4 → 6 → 8/9 pathway can be treated as the only major pathway in the reaction. However, if the data requires that at least one isomer traverse two influential barriers, then C-O activation plays a role in product formation, and this simplification is not appropriate. The results from the minimization are shown below in Figure 5.6.

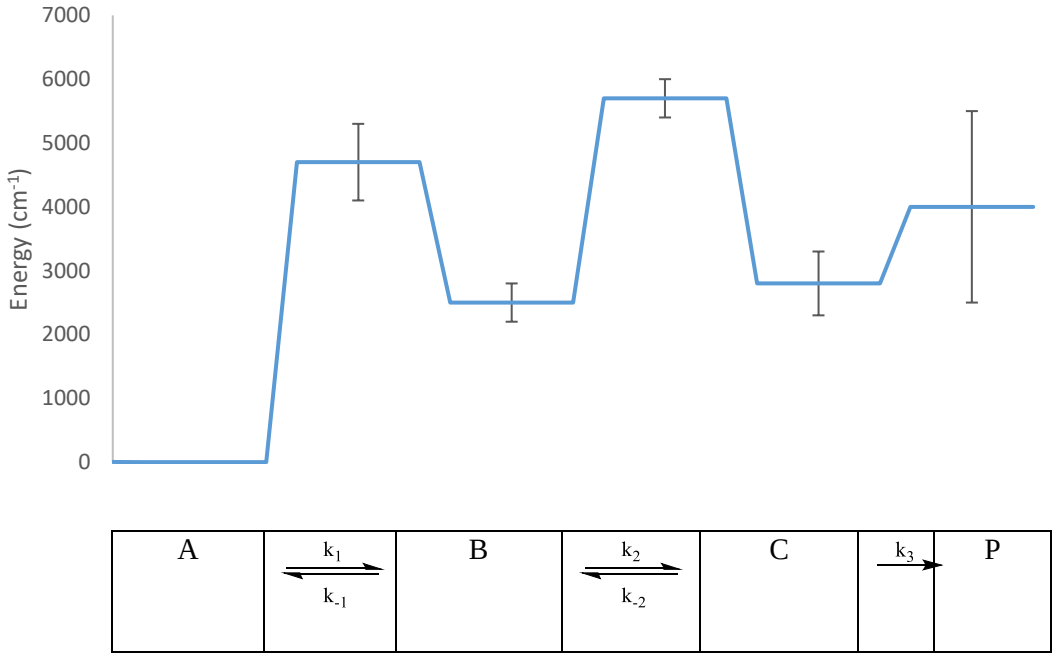

Figure 5.6 Results of the minimization of fitting the data to the linear mechanism, A → B → C → P.
The energies of the wells and barriers are
A is defined to be 0 cm^{-1},
First transition state = 4700 ± 600 cm^{-1},
B = 2500 ± 300cm^{-1},
Second transition state = 5700 ± 300 cm^{-1},
C < 2800cm^{-1} ± 500cm^{-1}
Final barrier < 6000 cm^{-1}

The best fit for each data set using the simplified model is shown in Figure 5.7.

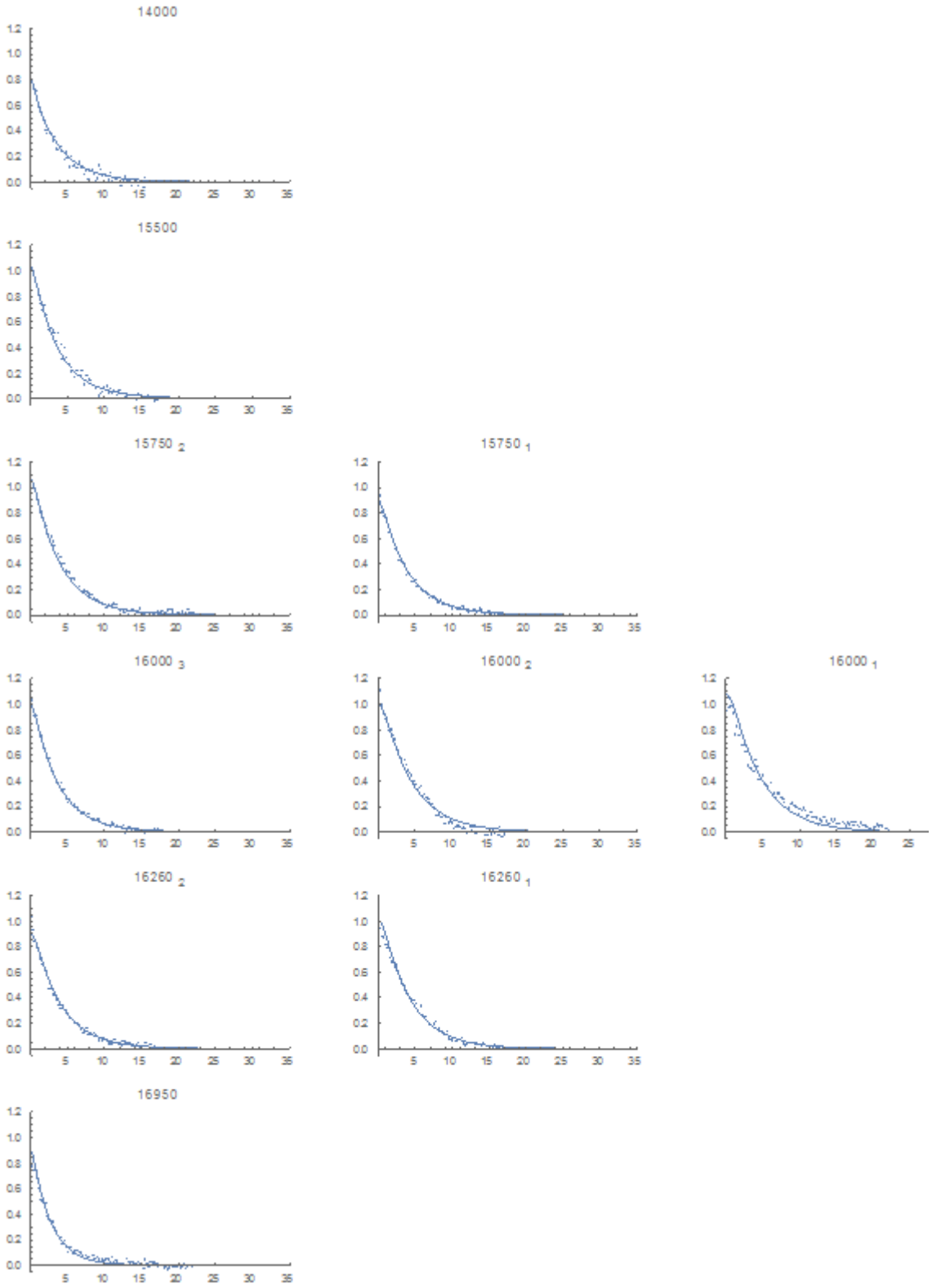

Figure 5.7 The decomposition of Ni^{+}Acetic Acid into $Ni^{+}C_2H_2O$ at various energies, fit using the potential energy surface illustrated in Figure 5.6.

As shown in Figure 5.7, rate constants constrained to behave in a manner predicted by RRKM and generated using the potential energy surface shown in Figure 5.6 are able to produce good fits to the kinetic data at all internal energies. This indicates that the unexpected behavior described above are likely the result of multiple isomers being populated in the molecular beam prior to photon absorption, and that the ratio of the isomers is sensitive to small changes in experimental parameters described in chapter 2 (backing pressure, ablation photon energy etc.). However, the barrier between A and B is large enough to influence the overall kinetic behavior of the system. This, along with the large energy difference between the zero point energies of A and B, and the fact that B never minimized to a value less than A, indicate that the behavior is not governed by two isomers crossing the same barrier with relatively different energies (which would correspond to pathway 1→2→4→6→8/9 in scheme 4). Rather, the results indicate that at least two barriers influence the overall reaction, implying that C-H activation plays a role. Therefore, a full elucidation of the PES will require an analysis which takes both pathways into account.

Kinetic Scans: Decomposition of $Ni^+(d_3)$Acetic Acid

The temporal dependence of the decay of $Ni^+(d_3)$Acetic Acid into $Ni^+C_2D_2O$ + HDO and Ni^+HDO + C_2D_2O at various internal energies are shown below in Figures 5.8a-o.

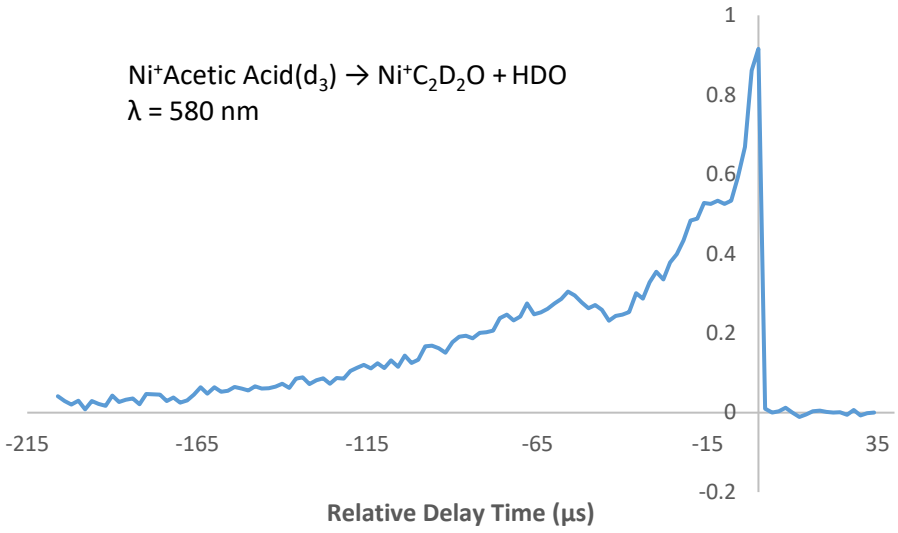

Figure 5.8a

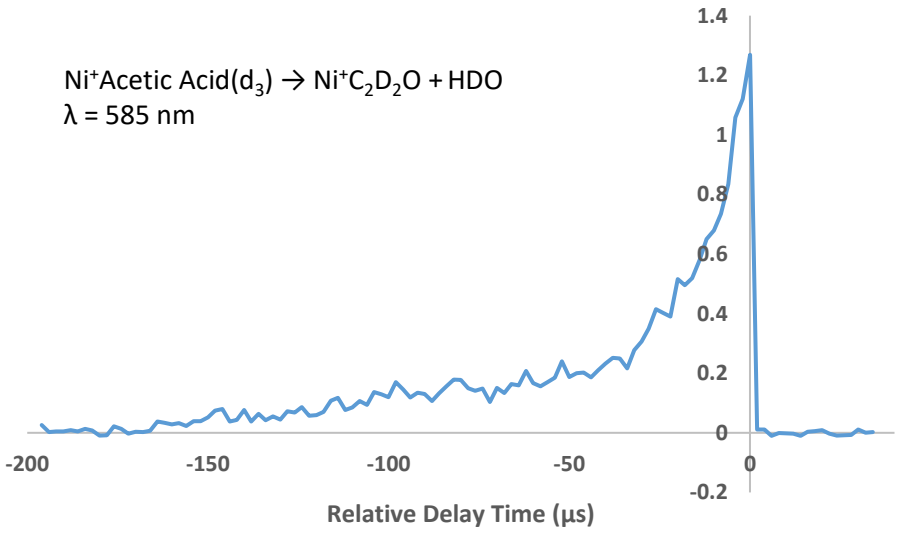

Figure 5.8b

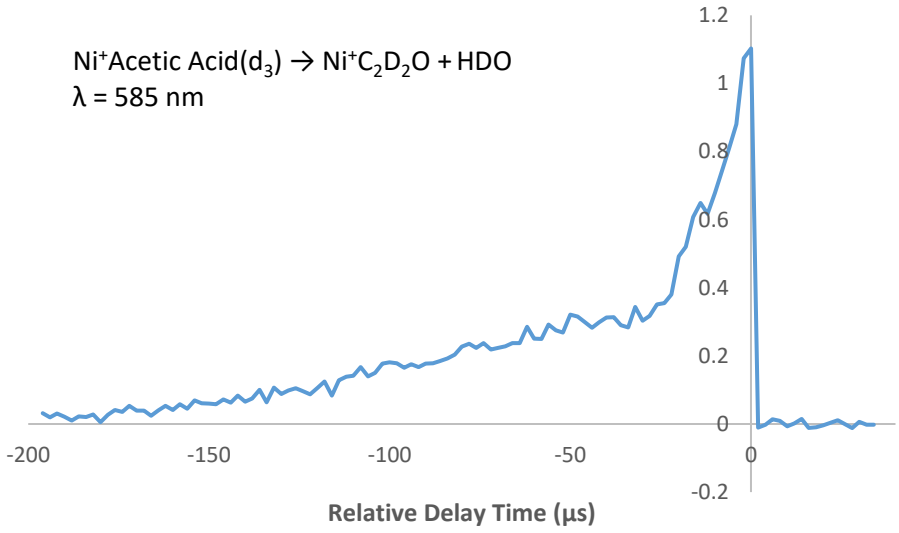

Figure 5.8c

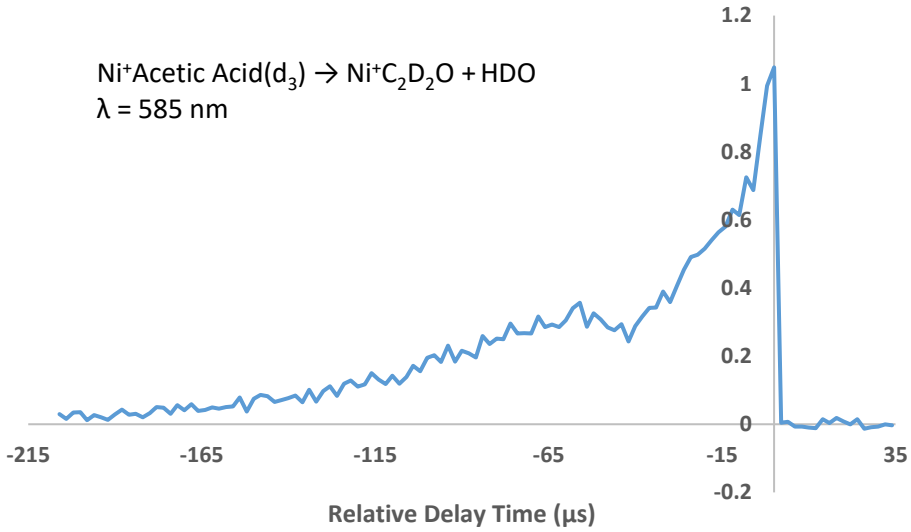

Figure 5.8d

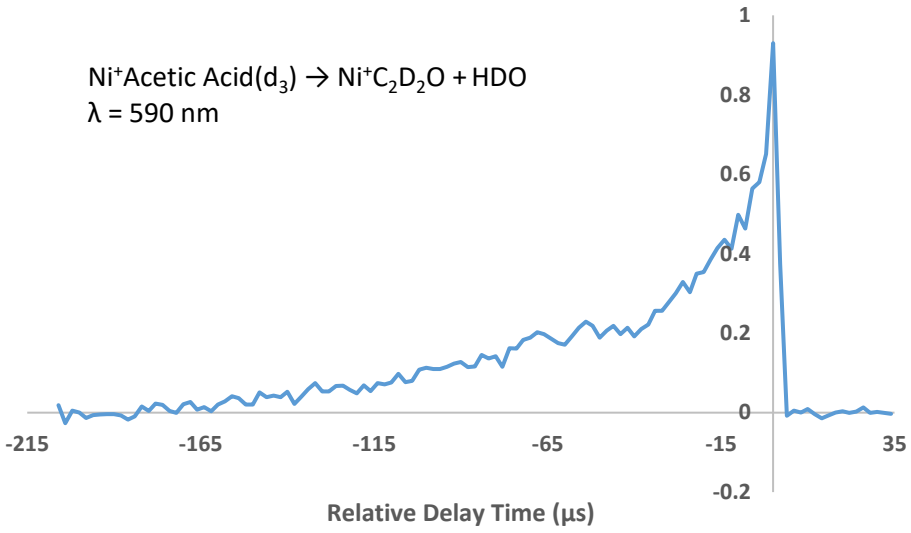

Figure 5.8e

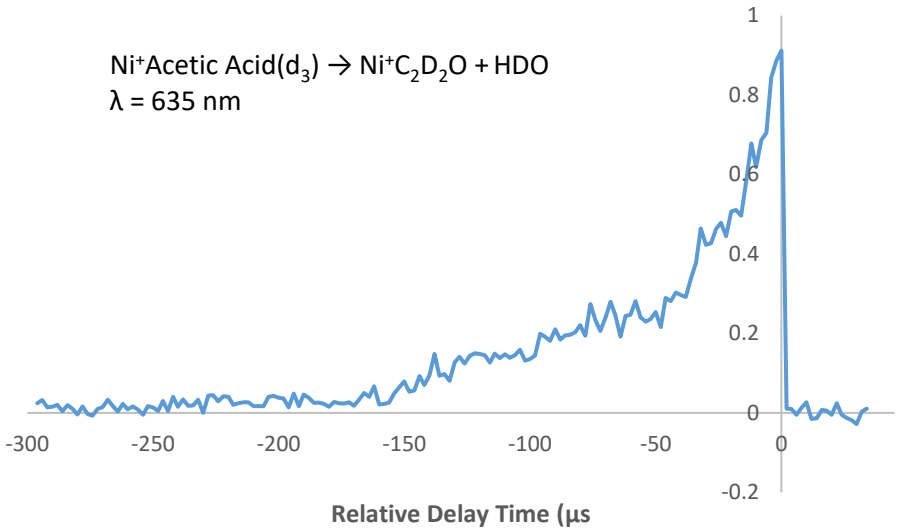

Figure 5.8f

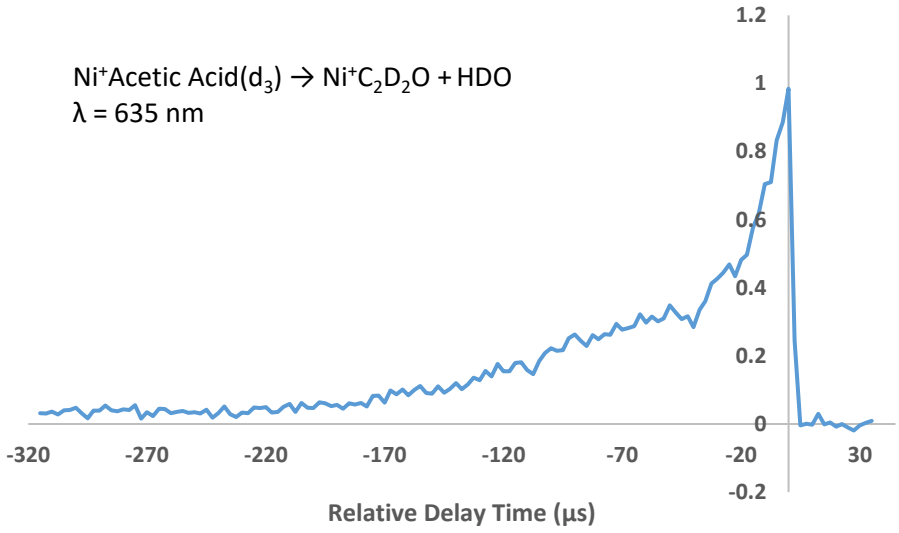

Figure 5.8g

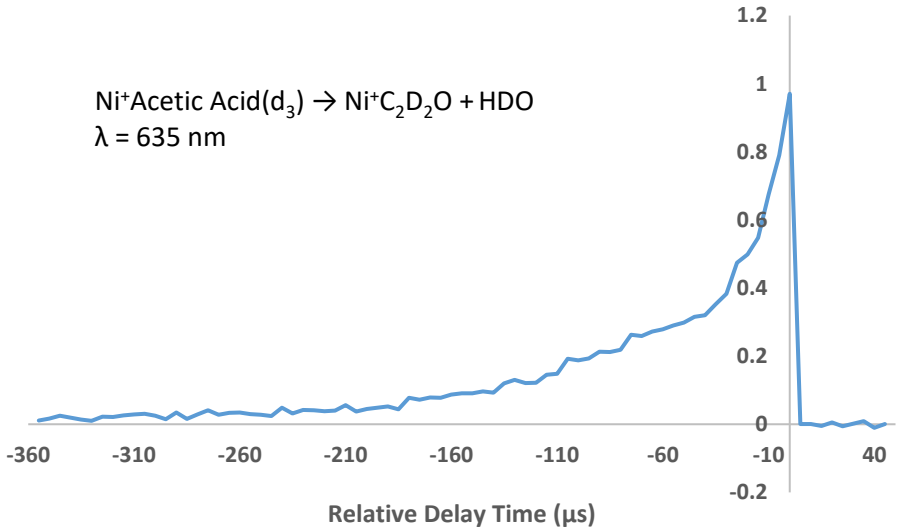

Figure 5.8h

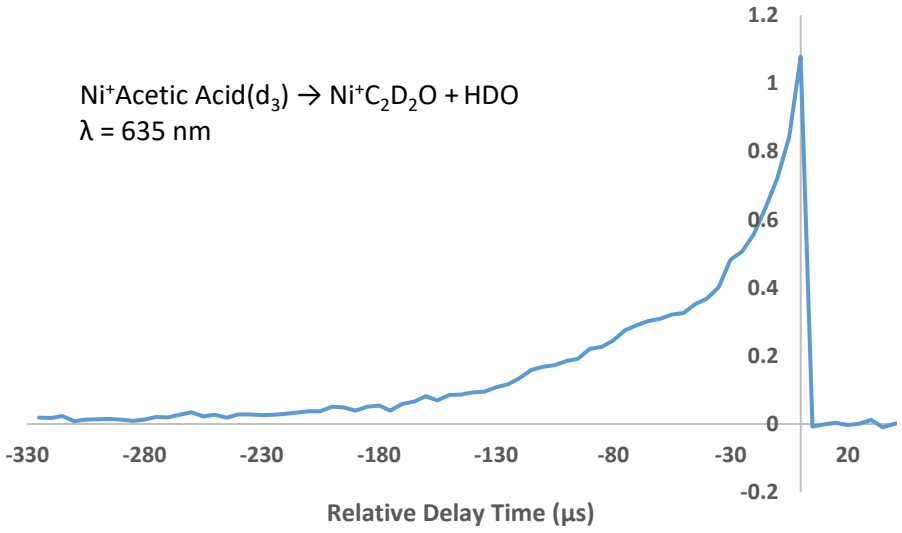

Figure 5.8i

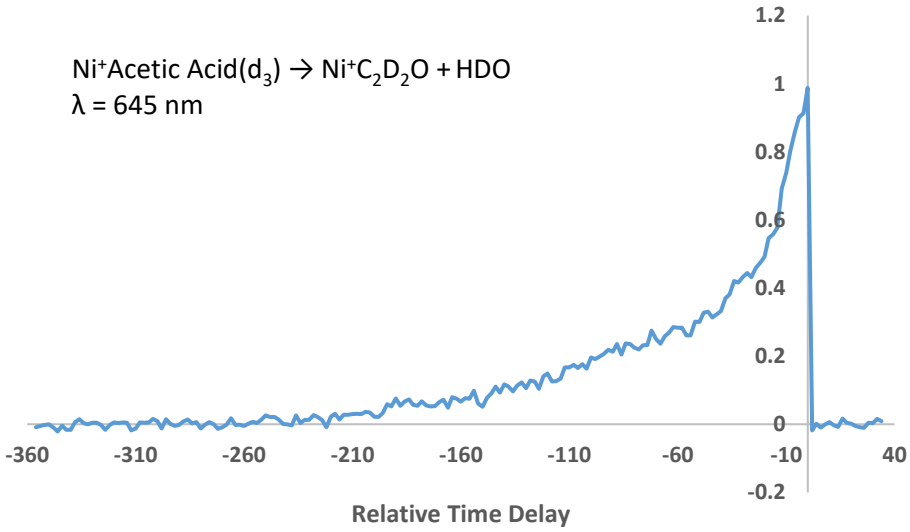

Figure 5.8j

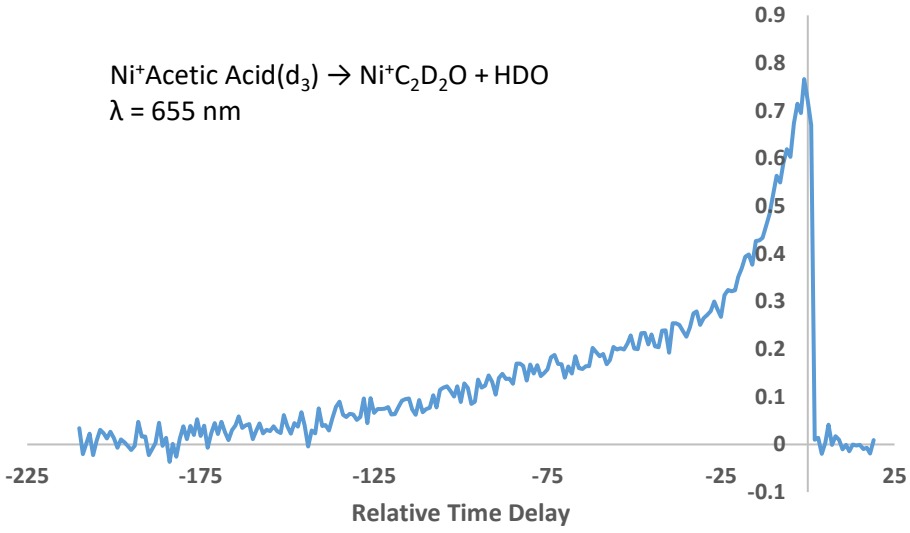

Figure 5.8k

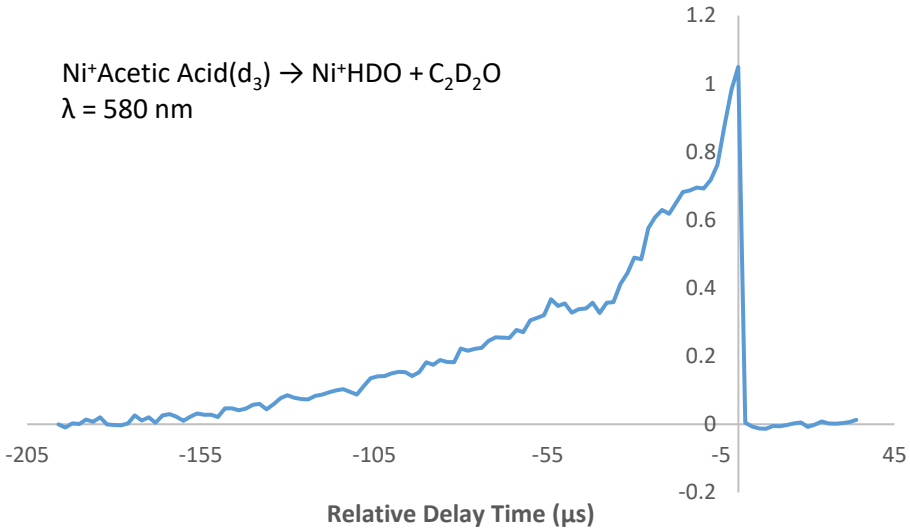

Figure 5.8l

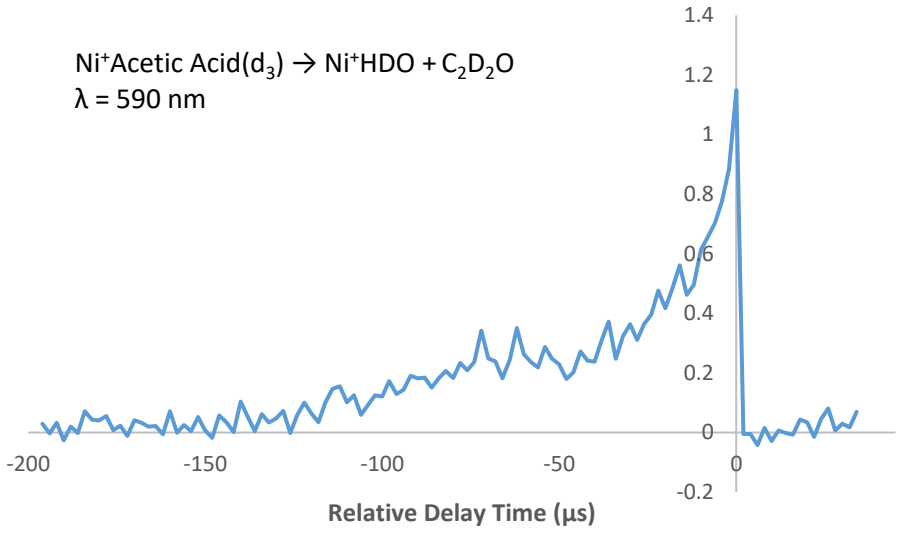

Figure 5.8m

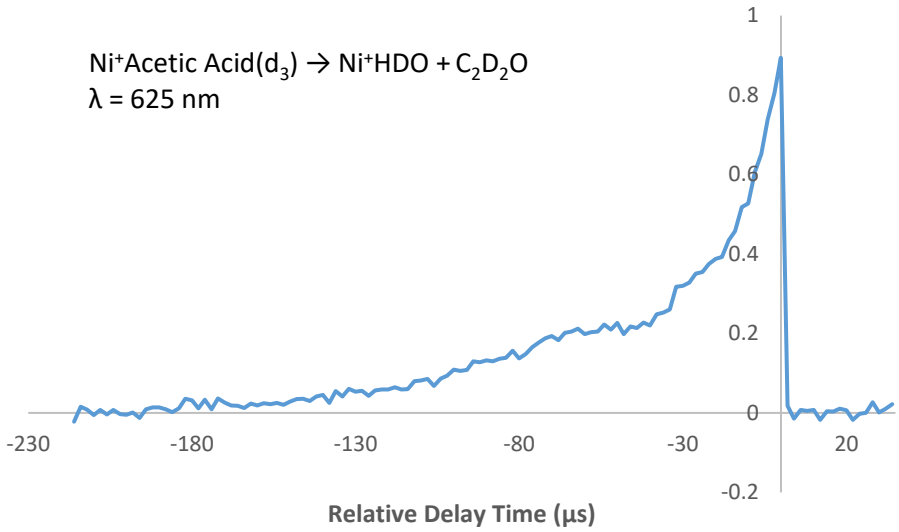

Figure 5.8n

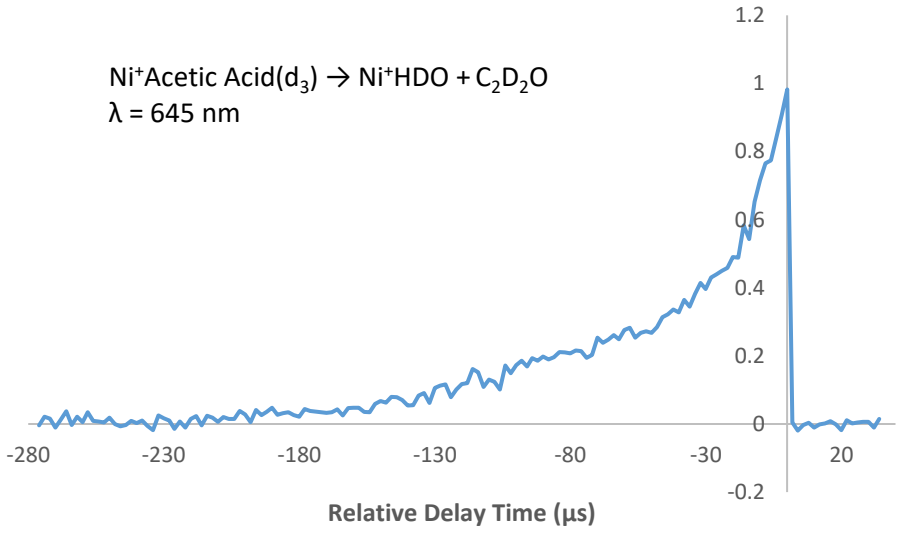

Figures 5.8o
Figures 5.8 a-o show the temporal dependence of the intensity of $Ni^+C_2D_2O$ and Ni^+HDO fragment production at various internal energies.

While a single exponential provides a relatively good fit at times past -50 µs, at times closer to coincident firing of the orthogonal accelerator and the dye laser, a single exponential fit both over and under predicts the data (Figure 5.9). The relatively good fit at larger absolute time values gives a kinetic isotope effect (KIE) of about 15 at all energies studied.

Typical kinetic isotope effects (KIE) for deuterium labeling range between 2 and 20 for primary effects (KIE's at the higher end of this range typically involve proton tunneling), and between 1 and 3 for secondary effects.

For deuterium labeled species, the KIE comes largely from a decrease in the zero point energy of the reactant, which effectively shifts the sum of states function in equation 3.1 to higher energies, thus reducing the rate constant at each energy. Deuterium, due to its larger mass, behaves more classically than hydrogen, and so the zero point energy for a deuterium labeled complex is closer to the classical minimum.

This will have a large effect on the rate constant if the deuterium replaces a hydrogen directly involved in the reaction, and a smaller effect otherwise. The very large KIE indicates that hydrogen tunneling plays a major role in the reaction.

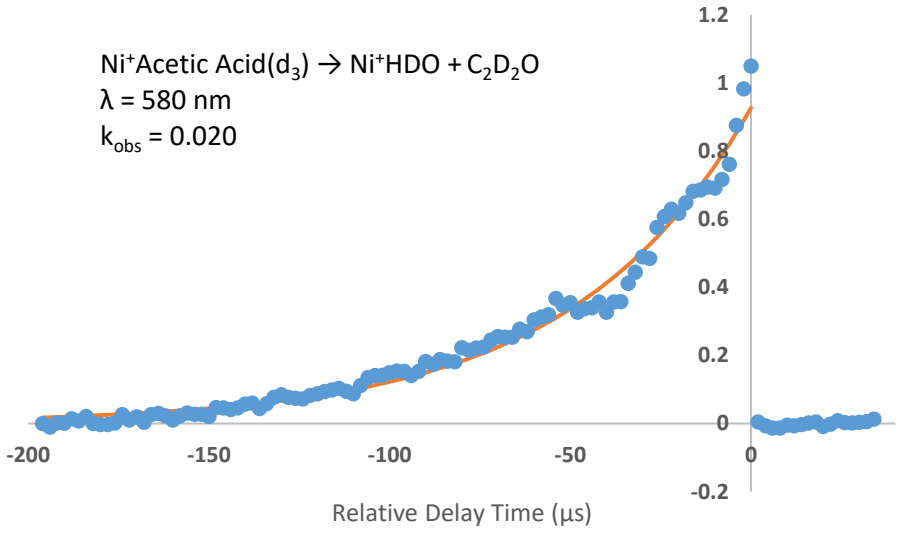

Figure 5.9 Temporal dependence of the decay of $Ni^+(d_3$-)Acetic Acid into $Ni^+HDO + C_2D_2O$ at 580 nm (blue data points) with a single exponential fit (red line).

The regions in the temporal profile of (d_3-)Acetic Acid decomposition that are over or under predicted by a single exponential fit are more prominent in higher energy scans. This is likely related to the competition between the different pathways in the mechanism. Quantification of this energetic dependence would be a significant step toward the quantification of the PES, but thus far has eluded our efforts.

Conclusion

The temporal dependence of $Ni^+C_2H_2O$ and Ni^+H_2O production resulting from the decomposition of Ni^+Acetic Acid was monitored at various internal energies. The identification of products led to the mechanism presented in scheme 4. The

decomposition profiles presented some unexpected results, which can be explained by assuming that both Ni^+Acetic Acid encounter complex isomers in scheme 4 can result in the observed products. Thus, the observed data is a combination of these two decomposition profiles, the influence of each being determined by their relative populations in the supersonic expansion. The data for the temporal dependence of products resulting from the decomposition of $Ni^+(d_3$-)Acetic Acid had some unexpected behavior which could also be explained by assuming that the reaction can proceed from both structures 1 and 2 in scheme 4 in the supersonic expansion. The data from the deuterated system also indicates that multiple steps in each pathway are kinetically important. This has been used to demonstrate that the kinetic data gathered here can be used to test the extent to which the overall mechanism can be simplified.

The most pressing data set that needs to be gathered for the completion of this study is the temporal dependence of Ni^+CH_3OH and Ni^+CD_3OH production at various energies. This data set will shed light on the details of the potential energy surface, as it is still unknown if it behaves in the same way as the rest of the data. Related to that, the relative intensity of each channel should be measured over the visible energy range to get direct information on the rate constants which govern the partitioning. Finally, the identity of the products (especially Ni^+CH_3OH since it is unclear if methanol has formed by the time of detection, or if the methyl and hydroxyl groups are independently bound to the nickel cation) and intermediates can be more accurately identified if 355 nm light is used to dissociate the species of interest while the species is in the time of flight portion of the instrument.

This study presents a number of interesting challenges. However, once completed, a full analysis should provide a level of detail about the potential energy surface which we have not been able to achieve in previous systems.

CHAPTER SIX

Conclusion

In conclusion, the studies presented in this manuscript illustrate the potential for kinetic measurements on single photon induced dissociation rearrangement reactions (SPIDRR) to serve in a unique role in elucidating the mechanism by which transition metals can act as catalysts. Specifically, the measurement of unimolecular kinetics of microcanonical systems below the separated reactant limit provides detailed information about the potential energy landscape. A comparison of the kinetics between different complexes provides insight into the role transition metals play in lowering activation barriers and stabilizing intermediates. When coupled with high level calculations, this growing body of experimental work sheds light on how the electronic structure of transition metals can affect both the rate of a catalyzed reaction and the specific energy dependent partitioning between reaction pathways.

Of particular note in this dissertation, is the kinetic measurements on the Ni^+ mediated dissociation of propanal. In this reaction, the product can form from two different pathways, with different energy dependent kinetic behavior. This difference leads to a counterintuitive inverse relationship between energy and the overall rate of formation of products at internal energies between about 17500 cm^{-1} and 19000 cm^{-1}. This data set, along with calculations of the vibrational energy levels of the species along the reaction coordinate led to quantification of the C-C and C-H bond activation energies. This demonstrates the highly sensitive nature of this experimental technique, and the utility that this growing body of data can provide to the scientific community.

Preliminary work done on the nickel mediated decomposition of acetic acid provides the first insights by our group into a system with two separate dipoles, leading to two distinct encounter complex isomers. Initial analysis on the results of this system demonstrate that the kinetic data gathered by our group may be used to quantify, to an extent, certain parts of the potential energy surface. Completing this study will provide a unique contribution to the expanding library of systems our group has investigated,

Overall, details concerning the energetic dependent overall kinetic behavior of transition metal mediated decomposition reactions provides a unique piece of the puzzle in the global attempt to elucidate how transition metals change the potential energy landscape of a reaction allowing them to act as catalysts. This information, when extrapolated out to the canonical ensemble and the condensed phase can lead to new methods in the ongoing global search for catalysts for specific reactions.

REFERENCES

1. D. Frattini; G. Cinti; G. Bidini; U. Desideri; R. Cioffi; E. Jannelli, "A system Approach in Energy Evaluation of Different Renewable Energies Sources Integration in Ammonia Production Plants" *Renewable Energy,* 2016, *99*, 472-482. DOI:10.1016/j.renene.2016.07.040

2. Fechete, I.; Wang, Y.; Vedrine, J. C., "The Past, Present and Future of Heterogeneous Catalysis" *Catalysis Today*, 2012, *189*, 2-27

3. Thayer, A. M. "Nobel Prizes Recognized Notable Developments in Catalysis" *C&EN*, 2013, 91, 68

4. Brauman, J. I.; Blair, L. K., "Gas-Phase Acidities of Alcohols", *J. Am. Chem. Soc.* 1970, *92*, 5986-5992

5. Sweeney, A. F.; Armentrout, P. B., "Hydrated copper ion chemistry: guided ion beam and computational investigation of $Cu^{2+}(H_2O)_n$ (n=7-10) complexes" *European Journal of Mass Spectrometry,* 2015, *21*, *3*, 497-516

6. Mo, O.; Yanez, M.; Salpin, J. Y.; Tortajada, J. "Thermochemistry, Bonding, and Reactivity of Ni^+ and Ni^{2+} in the Gas Phase" *Mass Spectrometry Reviews*, 2007, *26*, 474-516

7. Baer, T.; Lafleur, R.; Mazyar, O. The Role of Ion Dissociation Dynamics in the Study of Ion and Neutral Thermochemistry. In *Energetics of Stable Molecules and Reactive Intermediates,* Minas da Piedade, M. E., Ed.; Kluwer Academic: Dordrecht, 1999; pp 303-322.

8. Rodgers, M. T.; Armentrout, P. B. "Noncovalent Metal-Ligand Bond Energies as Studied by Threshold Collision-Induced Dissociation", *Mass Spec. Rev.* 2000, *19,* 215-247.

9. Laskin, J.; Lifshitz, C., "Kinetic Energy Release Distributions in Mass Spectrometry" *J. Mass. Spectrom.* 2001, *36*, 459-478

10. Eller, K.; Schwarz, H. Organometallic Chemistry in the Gas Phase. *Chem. Rev.* 1991, *91*, 1121−1177

11. Blagojevic, V.; Orlova, G.; Bohme, B. K., "O-Atom Transport Catalysis by Atomic Cations in the Gas Phase: Reduction of N_2O by CO", *J. Am. Chem. Soc.* 2005, *127*, 3545-3555

12. Ard, S. G.; Johnson, R. S.; Melko, J. J.; Martinez Jr., O.; Shuman, N. S.; Ushakov, V. G.; Guo, H.; Troe, J.; Viggiano, A. A. "Spin-Inversion and Spin – Selection in the Reactions $FeO^+ + H_2$ and $Fe^+ + N_2O$" *Phys. Chem. Chem. Phys.* 2015, *17*, 19709

13. Clemmer, D. E.; Chen, Y. M.; Khan, F. A.; Armentrout, P. B. *J. Phys. Chem.* 1994, *98*, 6522

14. Wiley, W. C.; McLaren, I. H. *Rev. Sci. Instrum.* 1955, *26*, 1150

15. D. I. Giacomo, "A Short Account of RRKM Theory of Unimolecular Reactions and of Marcus Theory of Electron Transfer in a Historical Perspective", *J. Chem. Educ.* 92, 2015, pp. 476-481.

16. F. A. Lindemann. "Discussion on 'The Radiation Theory of Chemical Action'", *Transactions of the Faraday Society.* 17, 1922, pp. 598-606.

17. O. K. Rice and H. C. Ramsperger, "Theories of unimolecular gas reactions at low pressures", *Journal of the American Chemical Society* 49(7), 1927 pp. 1617-1629. doi:10.1021/ja01406a001

18. L. S. Kassel, "Studies in Homogeneous Gas Reactions I", *The Journal of Physical Chemistry* 32(2), 1928 pp. 225-242, doi:10.1021/j150284a007

19. Marcus, Rudolph A, "Unimolecular Dissociations and Free Radical Recombination Reactions", *The Journal of Chemical Physics* 20(3), 1952 pp. 359-364, doi:10.1063/1.1700424

20. IUPAC Compendium of Chemical Terminology, 2nd ed. (the "Gold Book"). Compiled by A. D. McNaught and A. Wilkinson. Blackwell Scientific Publications, Oxford (1997). XML on-line corrected version: http://goldbook.iupac.org (2006-) created by M. Nic, J. Jirat, B. Kosata; updates compiled by A. Jenkins. ISBN 0-9678550-9-8. doi:10.1351/goldbook.

21. T. Beyer and D. F. Swinehart, "Algorithm 448: number of multiply-restricted partitions," *Communications of the ACM,* 16(6), 1973 pp. 379. dx.doi.org/10.1145/362248.362275

22. S. E. Stein and B. S. Rabinovitch, "Accurate Evaluation of Internal Energy Level Sums and Densities Including Anharmonic Oscillators and Hindered Rotors," *The Journal of Chemical Physics,* 58(6), 1973 pp. 2438-2445. dx.doi.org/10.1063/1.1679522

23. Z. Homayoon, S. A. Vázquex, R. Rodríguez-Fernández, and E. Martínez-Núñez, "Ab Initio and RRKM Study of the HCN/HNC Elimination Channels from Vinyl Cyanide," *The Journal of Physical Chemistry A,* 115, 2011 pp. 979-985. dx.doi.org/10.1021/jp109843a

24. P. M. Morse, "Diatomic Molecules According to the Wave Mechanics II. Vibrational Levels", *Physical Review*, 34, 1929 pp. 57-64. 10.1103/PhysRev.34.57.

25. Donahue, N. M. Reaction Barriers: Origin and Evolution. *Chem. Rev.* 2003, *103,* 4593−4604.

26. Schumacher, N.; Boisen, A.; Dahl, S.; Gokhale, A. A.; Kandoi, S.; Grabow, L. C.; Dumesic, J. A.; Mavrikakis, M.; Chorkendorff, I. Trends in low-temperature water-gas shift reactivity on transition metals. *J. Catal.* 2005, *229*, 265−275.

27. Flytzani-Stephanopoulos, M.; Gates, B. C. Atomically Dispersed Supported Metal Catalysts. *Annu. Rev. Chem. Biomol. Eng.* 2012, *3*, 545−574.

28. Zemski, K. A.; Justes, D. R.; Castleman, A. W., Jr. Studies of Metal Oxide Clusters: Elucidating Reactive Sites Responsible for the Activity of Transition Metal Oxide Catalysts. *J. Phys. Chem. B* 2002, *106*, 6136−6148.

29. Gronert, S. Mass Spectrometric Studies of Organic Ion/Molecule Reaction. *Chem. Rev.* 2001, *101*, 329−360.

30. Roithová, J.; Schröder, D. Selective Activation of Alkanes by Gas-Phase Metal Ions. *Chem. Rev.* 2010, *110,* 1170−1211.

31. Armentrout, P. B. Mass Spectrometry- Not Just a Structural Tool: The Use of Guided Ion Beam Tandem Mass Spectrometry to Determine Thermochemistry. *J. Am. Soc. Mass Spectrom.* 2002, *13*, 419−434.

32. Zhang, X.-G.; Liyanage, R.; Armentrout, P. B. Potential Energy Surface for Activation of Methane by Pt+: A combined Guided Ion Beam and DFT Study. *J. Am. Chem. Soc.* 2001, *123*, 5563−5575.

33. Liu, F.; Zhang, X.-G.; Armentrout, P. B. Activation of CH4 by gas phase Ni+ and the thermochemistry of Ni-ligand complexes. *Phys. Chem. Chem. Phys.* 2005, *7*, 1054−1064.

34. Armentrout, P. B.; Kretzschmar, I. Guided Ion Beam and Theoretical Studies of the Reactions of Pd+ with CS2: Thermochemistry of PdS+ and PdCS+. *Inorg. Chem.* 2009, *48*, 10371−10382.

35. Chen, Y.-M.; Sievers, M. R.; Armentrout, P. B. Activation of CH4, C2H6, C3H8, and c-C3H6 by gas-phase Pd+ and the thermochemistry of Pd-ligand complexes. *Int. J. Mass Spectrom. Ion Processes* 1997, *167/168*, 195−212.

36. Rue, C.; Armentrout, P. B.; Kretzschmar, I.; Schröder, D.; Schwarz, H. Guided Ion Beam Studies of the Reactions of Ni+, Cu+, and Zn+ with CS2 and COS. *J. Phys. Chem. A* 2002, *106*, 9788−9797.

37. Tolbert, M. A.; Mandich, M. L.; Halle, L. F.; Beauchamp, J. L. Activation of Alkanes by Ruthenium, Rhodium, and Palladium Ion in the Gas Phase: Striking Differences in Reactivity of First- and Second- Row Metal Ions. *J. Am. Chem. Soc.* 1986, *108*, 5675−5683.

38. Halle, L. F.; Houriet, R.; Kappes, M. M.; Staley, R. H.; Beauchamp, J. L. Nickel Ions Effect a Highly Specific 1,4-Dehydrogenation of Hydrocarbons in the Gas Phase: Metallacyles Are Not Involved. *J. Am. Chem. Soc.* 1982, 104, 6293−6297.

39. Bozovic, A.; Feil, S.; Koyanagi, G. K.; Viggiano, A. A.; Zhang, X.; Schlangen, M.; Schwarz, H.; Bohme, D. K. Conversion of Methane to Methanol: Nickel, Palladium, and Platinum (d9) Cations as Catalysts for the Oxidation of Methane by Ozone at Room Temperature. *Chem. - Eur. J.* 2010, *16*, 11605−11610.

40. Houriet, R.; Halle, L. F.; Beauchamp, J. L. Activation of C-H and C-C Bonds in Alkanes by First-Row Group 8 Atomic Transition-Metal Ions in the Gas-Phase. Mechanistic Details from a Study of Deuterium and 13C-Labeled Hydrocarbons. *Organometallics* 1983, *2*, 1818−1829.

41. van Koppen, P. A. M.; Brodbelt-Lustig, J.; Bowers, M. T.; Dearden, D. V.; Beauchamp, J. L.; Fisher, E. R.; Armentrout, P. B. Transition Metal Ion Mediated C-H and C-C Bond Activation of Alkanes: Dynamical Coupling between Entrance and Exit Channel Transition States. *J. Am. Chem. Soc.* 1991, *113*, 2359−2369.

42. van Koppen, P. A. M.; Bowers, M. T.; Fisher, E. R.; Armentrout, P. B. Relative Energetics of C-H and C-C Bond Activation of Alkanes: Reactions of Ni+ and Fe+ with Propane on the Lowest Energy (Adiabatic) Potential Energy Surface. *J. Am. Chem. Soc.* 1994, *116*, 3780−3791.

43. Blum, O.; O'Bannon, P.; Schwarz, H.; Schroeder, D. Specific Carbon-Carbon Bond Cleavage in n-Pentylbenzene by Bare nickel(I) in the Gas Phase. *Organometallics* 1993, *12*, 980−981.

44. Schultz, R. H.; Armentrout, P. B. Threshold Collisional Activation of Fe+C3H8: Probing the Potential Energy Surface. *J. Am. Chem. Soc.* 1991, *113*, 729−730.

45. Haynes, C. L.; Armentrout, P. B. Thermochemistry and Structures of CoC3H6 +: Metallacycle and Metal-Alkene Isomers. *Organometallics* 1994, *13*, 3480−3490.

46. Haynes, C. L.; Fisher, E. R.; Armentrout, P. B. Probing the [CoC3H8]+ Potential Energy Surface: A Detailed Guided-Ion Beam Study. *J. Phys. Chem.* 1996, *100*, 18300−18316.

47. Carpenter, C. J.; van Koppen, P. A. M.; Bowers, M. T. Details of Potential Energy Surfaces Involving C-C Bond Activation: Reactions of Fe+, Co+, and Ni+ with Acetone. *J. Am. Chem. Soc.* 1995, *117*, 10976−10985.

48. Villarroel, O. J.; Laboren, I. E.; Bellert, D. J. Co+-Assisted Decomposition of h6-acetone and d6-acetone: Acquisition of Reaction Rate Constants and Dynamics of the Dissociative Mechanism. *J. Phys. Chem. A* 2012, *116*, 3081−3088.

49. Laboren, I. E.; Villarroel, O. J.; Dee, S. J.; Castleberry, V. A.; Bellert, D. J.; Klausmeyer, K. The Reaction Rate Constants and Mechanistic Detail of the Ni+ + Butanone Reaction. *J. Phys. Chem. A* 2011, *115*, 1810−1820.

50. Dee, S. J.; Castleberry, V. A.; Villarroel, O. J.; Laboren, I. E.; Bellert, D. J. Low Energy, Reaction Rate Constants for the Ni+-Assisted Decomposition of Acetaldehyde: Observation of C-H and C-C activation. *J. Phys. Chem. A* 2010, *114*, 1783−1789.

51. Dee, S. J.; Castleberry, V. A.; Villarroel, O. J.; Laboren, I. E.; Frey, S. E.; Ashley, D.; Bellert, D. J. Rate-Limiting Step in the Low-Energy Unimolecular Decomposition Reaction of Ni+•Acetone into Ni+CO + Ethane. *J. Phys. Chem. A* 2009, *113*, 14074−14080.

52. Castleberry, V. A.; Dee, S. J.; Villarroel, O. J.; Laboren, I. E.; Frey, S. E.; Bellert, D. J. The Low Energy Unimolecular Reaction Rate Constants for the Gas Phase, Ni+ Mediated Dissociation of the C-C σ- bond in Acetone. *J. Phys. Chem. A* 2009, *113*, 10417−10424.

53. Wiley, W. C.; McLaren, I. H. Time-of-Flight Mass Spectrometer with Improved Resolution. *Rev. Sci. Instrum.* 1955, *26*, 1150−1157.

54. Morse, M. D. Atomic, Molecular, and Optical Physics: Atoms and Molecules; Experimental Methods in the Physical Sciences; Springer, 1996; Vol 29, p 211 0.1016/S0076-695X(08)60784-X.

55. Auerbach, D. J. Velocity Measurements by Time of Flight Methods. In Atomic and Molecular Beam Methods, Scoles, G.; Bassi, D.; Buk, U.; Laine, D., Eds.; Oxford University Press: New York, 1988; pp 363−369.

56. Haberland, H.; buck, U.; Tolle, M. *Rev. Sci. Instrum.* 1985, *56*, 1712.

57. National Institute of Standards and Technology, Physical Measurements Laboratory: Basic Atomic Spectroscopic Data. Energy Levels of Singly Ionized Nickel; http://physics.nist.gov/PhysRefData/Handbook/Tables/nickeltable6_a.htm.

58. Hohenberg, P.; Kohn, W. Inhomogeneous Electron Gas. *Phys. Rev.* 1964, *136*, 864−871.

59. Kohn, W.; Sham, L. J. Self-Consistent Equations Including Exchange and Correlation Effects. *Phys. Rev.* 1965, *140*, 1133−1138.

60. Perdew, J. P.; Burke, K.; Ernzerhof, M. Generalized Gradient Approximation Made Simple. *Phys. Rev. Lett.* 1996, *77*, 3865−3868.

61. Dunning, T. H. Gaussian Basis Sets for Use in Correlated Molecular Calculations. I. The Atoms Boron Through Neon and Hydrogen. *J. Chem. Phys.* 1989, *90*, 1007−1023.

62. Dunning, T. H.; Woon, D. E. Gaussian Basis Sets for Use in Correlated Molecular Calculations. III. The Atoms Aluminum through Argon. *J. Chem. Phys.* 1993, *98*, 1358−1371.

63. Laury, M. L.; Boesch, S. E.; Haken, I.; Sinha, P.; Wheeler, R. A.; Wilson, A. K. Harmonic Vibrational Frequencies: Scale Factors for Pure, Hybrid, Hybrid Meta, and Double-Hybrid Functionals in Conjunction with Correlation Consistent Basis Sets. *J. Comput. Chem*. 2011, *32*, 2339−2347.

64. Minenkov, Y.; Singstad, A.; Occhipinti, G.; Jensen, V. The Accuracy of DFT-Optimized Geometries of Functional Transition Metal Compounds: A Validation Study or Catalysts for Olefin Metathesis and other Reactions in the Homogeneous Phase. *Dalton Trans.* 2012, *41*, 5526−5541.

65. Bühl, M.; Reimann, C.; Pantazis, D. A.; Bredow, T.; Neese, F. Geometries of Third-Row Transition-Metal Complexes from Density-Functional Theory. *J. Chem. Theory Comput.* 2008, *4*, 1449−1459.

66. Rappoport, D.; Crawford, N. R. M..; Furche, F.; Burke, K. Approximate Density Functionals: Which should I Choose?, Encyclopedia of Inorganic Chemistry, Solomon, E. I.; King, R. B.; Scott, R. A., Eds.; Wiley: Chichester, 2009.

67. Cramer, C. J.; Truhlar, D. G. Density Functional Theory for Transition Metals and Transition Metal Chemistry. *Phys. Chem. Chem. Phys.* 2009, *11*, 10757−10816.

68. Bauernschmitt, R.; Ahlrichs, R. Stability Analysis for Solutions of the Closed Shell Kohn-Sham Equation. *J. Chem. Phys.* 1996, *104*, 9047−9052.

69. Frisch, M. J.; Trucks, G. W.; Schlegel, H. B.; Scuseria, G. E.; Robb, M. A.; Cheeseman, J. R.; Scalmani, G.; Barone, V.; Mennucci, B.; Petersson, et al. Gaussian 09, Revision D.01; Gaussian, Inc.: Wallingford, CT, 2009.

70. Zhu, L.; Hase, W. L.; Quantum Chemistry Program Exchange; Indiana University: Bloomington, IN, 1994; Program No. QCPE 644.

71. Liang, B.; Zhou, M.; Andrews, L. Reactions of Laser-Ablated Ni, Pd, and Pt Atoms with Carbon Monoxide: Matrix Infrared Spectra and Density Functional Calculations on M(CO)n (n = 1−4), M(CO)n− (n = 1−3), and M(CO)n + (n = 1−2), (M = Ni, Pd, Pt). *J. Phys. Chem. A* 2000, *104*, 3905−3914.

72. Distefano, G. Photoionization Study of Fe(CO)5 and Ni(CO)4. *J. Res. Natl. Bur. Stand., Sect. A* 1970, *74A*, 233−238.

73. Khan, F. A.; Steele, D. L.; Armentrout, P. B. Ligand Effects in Organometallic Thermochemistry: The Sequential Bond Energies of Ni(CO)x + and Ni(N2)x + (x = 1−4) and Ni(NO)x + (x = 1−3). *J. Phys. Chem.* 1995, *99*, 7819−7828.

74. Wigner, E. On the Quantum Correction for Thermodynamic Equilibrium. *Phys. Rev.* 1932, *40*, 749−459.

75. Bell, R. P. The Tunnel Effect Correction for Parabolic Potential Barriers. *Trans. Faraday Soc.* 1959, *55*, 1−4.

76. Hoyle, J. In The Chemistry of Acid Derivatives; Patai, S., Ed.; Wiley: Chichester, England, 1992; Chapter 11.

77. Taylor, R. In The Chemistry of Acid Derivatives; Patai, S., Ed.; Wiley: Chichester, England, 1992; Chapter 15.

78. Sabatier, “Catalysis in Organic Chemistry,” translated by E. Emmet Reid, D. Van Nostrand and Co., New York, 1922, par. 831-839

79. Woolley, M.; Khairallah, G. N.; Silva, G.; Donnelly, P. S.; O'Hair, R. A. J. Direct Versus Water-Mediated Protodecarboxylation of Acetic Acid Catalyzed by Group 10 Carboxylates, $[(phen)M(O_2CCH_3)]^+$. *Organometallics* 2014, 33, 5185-5197.

80. Vajo, J. J.; Sun Y. K.; Weinberg, W. H. Catalytic Dehydration of Acetic acid on a Graphitized Platinum Surface. *J. Phys. Chem.* 1987, *91*, 1153-1158

81. O'Hair, R. A. J.; Rijs, N. J. Gas Phase Studies of the Pesci Decarboxylation Reaction: Synthesis, Structure, and Unimolecular and Bimolecular Reactivity of Organometallic Ions. *Acc. Chem. Res.* 2015, 48, 329-340.

82. Asadi, M; Kim, K.; Liu, C.; Addepalli, A. V.; Abbasi, P.; Yasaei, P.; Phillips, P.; Behranginia, A.; Cerrato, J. M.; Haasch, R.; Zapol, P.; Kumar, B.; Klie, R. F.; Abiade, J.; Curtiss, L. A.; Salehi-Khojin, A., "Nanostructured Transition Metal Dichalcogenide Electrocatalysts for CO_2 Reduction in Ionic Liquid", *Science*, 2016, 353, 467-470. DOI: 10.1126/science.aaf4767

83. Rijs, N. J.; O'Hair, A. J. "Dimethylcuprate-Catalyzed Decarboxylative Coupling of Allyl Acetate", *Organometallics.* 2012, 31, 3012-8023

84. Sekine, K.; Yamada, T., "Silver-Catalyzed Carboxylation", *Chem. Soc. Rev.*, 2016, Advance Article, DOI: 10.1039/c5cs00895f

85. Markus, R. A., "Unimolecular Dissociations and Free Radical Recombination Reactions", *J. Chem. Phys.* 1952, 20, 359-364. Doi:10.1063/1.1700424